THE FLORIDA STATE UNIVERSITY

COLLEGE OF ARTS AND SCIENCES

SEARCH FOR RESONANCES IN THE PHOTOPRODUCTION OF PROTON-ANTIPROTON PAIRS

By

BURNHAM E. STOKES

A dissertation submitted to the
Department of Physics
in partial fulfillment of the
requirements for the degree of
Doctor of Philosophy

Degree Awarded:
Fall Semester, 2006

The members of the Committee approve the dissertation of Burnham E. Stokes defended on June 16, 2006.

Paul Eugenio
Professor Directing Dissertation

Gregory Riccardi
Outside Committee Member

Todd Adams
Committee Member

Larry Dennis
Committee Member

Alexander Ostrovidov
Committee Member

Jorge Piekarewicz
Committee Member

Dennis Weygand
Committee Member

Approved:

David Van Winkle, Chair
Department of Physics

The Office of Graduate Studies has verified and approved the above named committee members.

To Cathy…

ACKNOWLEDGEMENTS

First, I am especially grateful to my wife, Cathy, for selflessly supporting me through the years. She has made many great sacrifices so that I could succeed. I am deeply indebted to her for all that she has given. Next, I would like to thank my advisor Dr. Paul Eugenio for his continuous support throughout my graduate career, for helping with my writing skills, for taking the time to review my work, for encouraging me to give talks, and for requiring nothing less than excellence. I would also like to thank him for his friendship and for being concerned about my personal life as well as professional. I would like to thank Dr. Dennis Weygand for taking interest in my work and for the valuable time spent discussing the analysis. His experience and creativity were invaluable assets and he often inspired me at times when I needed it most. I would like to thank Dr. Sasha Ostrovidov for reviewing my analysis and my dissertation. I would also like to thank him for the many times he helped debug my programs. I would like to thank Dr. Lei Guo for his help with my analysis and for his attention to details. His feedback has greatly improved the quality of this analysis.

I would like to thank my friends Blake Sharin, Lukasz Blaszczyk, Dr. Shifeng Chen, and Philip Coltharp for often lending me their ears as well as their hands. I owe them for the many times they helped me with software issues, with detector construction, and especially for carrying large objects up and down stairs. I would like to thank Dr. Simon Capstick who has been a mentor to me throughout my college career. Countless times, Simon has given me help, advice, and inspiration, for which I am truly grateful. I would also like to thank my committee members, Dr. Jorge Piekarewicz, Dr. Todd Adams, Dr. Larry Dennis, and Dr. Greg Riccardi,

for their time and effort reviewing my dissertation. Finally, I would like to thank my family for supporting me over the years and for being extremely patient.

TABLE OF CONTENTS

APPENDIX

LIST OF TABLES

LIST OF FIGURES

ABSTRACT

Results are reported on the reaction $\gamma p \rightarrow p\bar{p}p$ with beam energy in the range 4.8-5.5 GeV. The data were collected at the Thomas Jefferson National Accelerator Facility in CLAS experiment E01-017(G6C). The focus of this study is an understanding of the mechanisms of photoproduction of proton-antiproton pairs, and to search for intermediate resonances, both narrow and broad, which decay to $p\bar{p}$. The total measured cross section in the photon energy range 4.8-5.5 GeV is $\sigma = 33 \pm 2\ nb$. Measurement of the cross section as a function of energy is provided. An upper limit on the production of a narrow resonance state previously observed with a mass of 2.02 GeV/c^2 is placed at 0.35 nb. No intermediate resonance states were observed. Meson exchange production appears to dominate the production of the proton-antiproton pairs.

CHAPTER 1

INTRODUCTION

In the Standard Model of elementary particle interactions, particles interact through three forces; the weak, strong, and electromagnetic interactions (Fig. 1.1)[1]. Gravity is excluded because it is not described by the Standard Model, however it is also a fundamental interaction. The electromagnetic force is mediated by photons, the weak force is mediated through Z and W bosons, and the strong force is mediated through gluons. Each elementary particle has a complementary antiparticle.

The Standard Model describes how elementary particles interact to make up matter. Quantum Chromodynamics (QCD) is the theory which describes the strong interaction. However, at the energies of quark confinement, the perturbation methods of QCD break down for calculating strong force interactions. Just how these processes actually occur remains one of the major questions to date which physicists are trying to understand.

We know that the hydrogen atom is made of a proton orbited by an electron, and that the proton is made up of quarks and gluons. The simplest description of the proton is that it is made of three quarks,(Fig. 1.2), and while this "Quark Model" [2] picture has been very useful in understanding the nature of sub-nuclear matter, the proton is actually much more complicated. The quarks interact through the strong force via force carriers called gluons. Quarks and gluons interact to form various types of sub-nuclear matter called hadrons. Protons and neutrons are a form of hadrons called baryons, and we also know of other baryons and other forms of hadrons called mesons.

Table 1.1. The usual Quark Model hadrons and other hadrons allowed by QCD.

Hadron Configurations	
Usual Quark Model Hadrons	
Bosons	Fermions
$q\bar{q}$	qqq
Unusual Hadrons	
Bosons	Fermions
gg/ggg	$qqqg$
$q\bar{q}g$	$qqqq\bar{q}$
$qq\bar{q}\bar{q}$	
$qqq\bar{q}\bar{q}\bar{q}$	
plus other configurations	

Yet the Standard Model suggests many more new forms of matter which are recently discovered or have yet to be explored [3]. QCD allows the existence of multiquark mesons, such as a particle containing two quarks and two antiquarks ($qq\bar{q}\bar{q}$). Hybrid mesons are predicted as well. These contain gluons as well as quarks, qqg for example. There are also predictions for purely gluonic states (gg or ggg). In hadronic nuclear physics one studies how quarks and gluons form the observable hadrons to better understand the origin of matter and the nature of confinement.

Hadron spectroscopy is the study of the interactions and states of mesons, baryons, and other particles which are composed of quarks and gluons. During the last half century, many new hadrons have been identified expanding our understanding of nature. A main goal of nuclear physics is the discovery and the study of forms of hadronic matter. This includes identifying new mesons and baryons, pure quarkless objects called glueballs, and other forms of exotic matter like gluonic hybrids, pentaquarks, and other multiquark states.

New hadrons can be produced through the use of energetic particle beams that interact with targets or other particle beams[1]. Examples of particle beams are photons, pions, protons, and antiprotons. These beams are used to produce many hadronic interactions, of which the byproducts are observed by particle detectors.

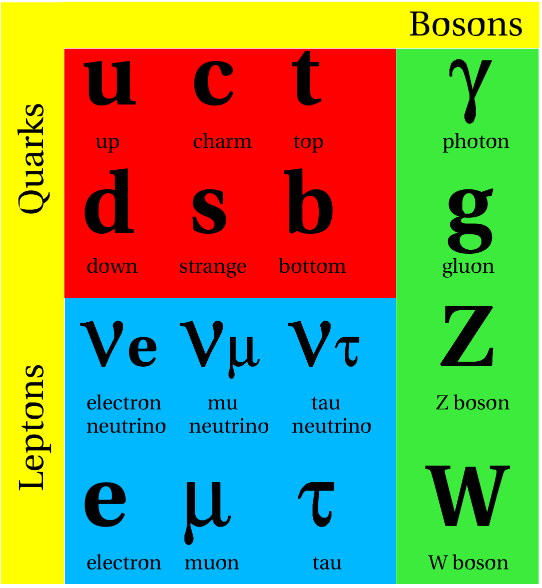

Figure 1.1. The Standard Model table of elementary particles. Nuclear physicists study how the quarks and gluons form hadrons.

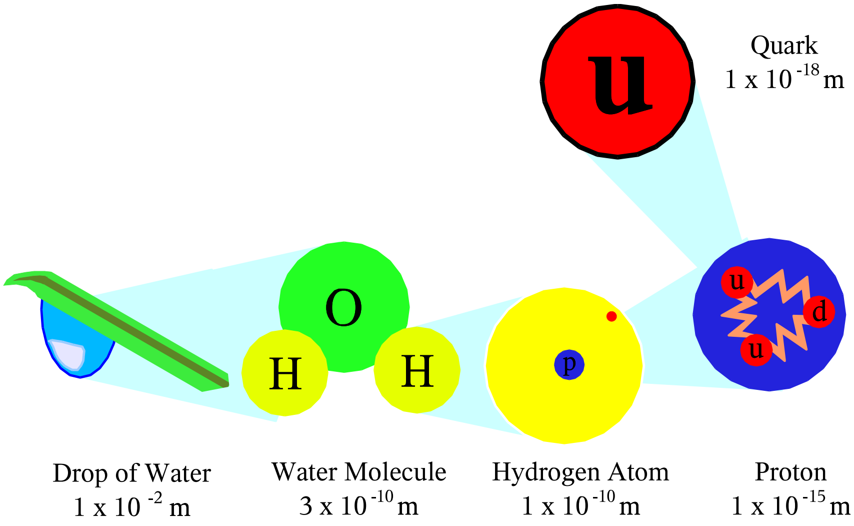

Figure 1.2. The decomposition of matter into smaller substructures and elementary particles.[4]

The focus of this work is the analysis of experimental data collected at Thomas Jefferson National Accelerator Facility (Jefferson Lab). Jefferson Lab is a U.S. Department of Energy facility which is utilized by scientists worldwide. At Jefferson Lab, electrons are accelerated using the Continuous Electron Beam Accelerating Facility (CEBAF), and pass into three experimental halls (Hall A, B, and C). Hall B is the location of the CEBAF Large Acceptance Spectrometer (CLAS) that is used to detect the byproducts of the high energy collision reactions. In this experiment, protons at rest interact with photons of energy up to 5.5 GeV. When the photon interacts with a proton, the products are projected forward into the CLAS detector, and the properties of those products are measured. In this study, events are observed in which the proton and photon interact to produce an additional proton and antiproton ($\gamma p \rightarrow pp\bar{p}$).

Proton-antiproton studies have a rich history spanning more than thirty years. Proton-antiproton pair production has been studied in proton-antiproton scattering, pion-production, and photoproduction experiments. While there has been a history of much excitement over the prospects of the observation of new forms of exotic matter decaying to proton-antiproton, these earlier experiments suffered from limited statistics. Only the J/ψ meson has been clearly observed to decay to $p\bar{p}$ [5].

The experiment E99-005[6] at Jefferson Lab was optimized for acquiring data of the reaction $\gamma p \rightarrow \phi p, \phi \rightarrow K^+K^-$. In E99-005, approximately 2000 events identified as $\gamma p \rightarrow pp\bar{p}$ were observed[8]. This relatively large yield was unexpected because the reaction requires complicated mechanisms to produce the three quarks and three antiquarks. This yield has led to the search for the same decay in Jefferson Laboratory experiment E01-017 data [7]. Experiment E01-017 had a higher beam current and was configured for a larger acceptance of this type of event. E01-017 has provided an order of magnitude larger number of $\gamma p \rightarrow pp\bar{p}$ events, and it is this data set that is the main focus of this work.

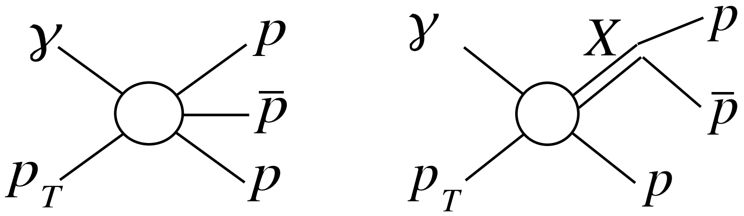

Figure 1.3. Differing $p\bar{p}$ pair production mechanisms. Left: The $p\bar{p}$ pair are produced directly without an intermediate resonance. Right: Production of a resonance which decays to a $p\bar{p}$ pair.

Initially, the $p\bar{p}$ system had much interest due to theories that predicted nucleon-antinucleon states that are loosely bound in a molecule-like structure called baryonium. Bubble chamber experiments that searched for these states used proton-antiproton elastic scattering suffered very little data and complications arising from antiproton annihilations. A problem with bubble chamber experiments is that after the antiproton scatters off a proton, it may annihilate before traveling a detectable distance [9]. Another problem is that events in which the antiproton annihilates in flight may be indistinguishable from those in which it decays at rest[10]. In photoproduction the $p\bar{p}$ pair is produced in the interaction, which suggests that the $p\bar{p}$ pair may be produced in the decay of a produced state. It is also possible though that the $p\bar{p}$ pair could be produced directly without an intermediate resonance. The difference of these interactions is illustrated in Figure 1.3. The intermediate particle could be a baryonium, a hybrid four-quark meson, or even a normal $q\bar{q}$ meson.

One difficulty in studying the reaction $\gamma p \rightarrow pp\bar{p}$ is in properly handling the identical particles. In this final state, there are two protons, one of which may be associated with a $p\bar{p}$ resonance and the other possibly not. In order to characterize the type of production, one would like to be able to distinguish the protons. Under some kinematic conditions this can be done. In diffractive production, the photon essentially “skims” off the proton and produces the proton-antiproton pair (Fig. 1.4).

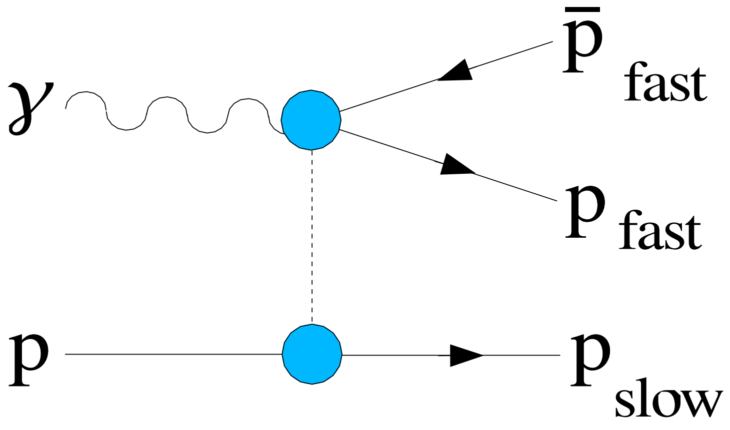

Figure 1.4. The diffraction/meson exchange diagram. In diffractive production, the photon essentially "skims" off the proton and produces the $p\bar{p}$ pair. The recoil proton is expected to receive very little momentum from a meson which decays to a proton-antiproton pair.

In baryon exchange, a photon interacts with an exchange baryon, converting it to a fast forward-going proton, leaving a slow-going resonance (Fig. 1.5). Antibaryon exchange is similar, except that the fast forward-going particle is an antiproton.

This dissertation is outlined as follows. In Chapter 2, a brief history of proton-antiproton resonance searches is covered, followed by theoretical predictions for quasi-nuclear and multiquark baryonia. Chapter 2 ends with definitions of kinematic variables used throughout the dissertation. In Chapter 3, the experimental apparatus and the experimental run conditions are described. The event reconstruction is described in Chapter 4, and Chapter 5 describes the procedures used to select and identify the reaction $\gamma p \to pp\bar{p}$. Chapter 6 describes the general features of the data. Chapter 7 describes the models and methods used for generating Monte Carlo events, and also describes CLAS resolutions studies. In chapter 7, a description of how the Monte Carlo simulations were fit to the data is given. Chapter 7 also explains how the production mechanisms for proton-antiproton pair production were determined. In Chapter 8, upper limits on the production of a previously observed resonance is calculated, and also cross section measurements are shown. In Chapter 9, an

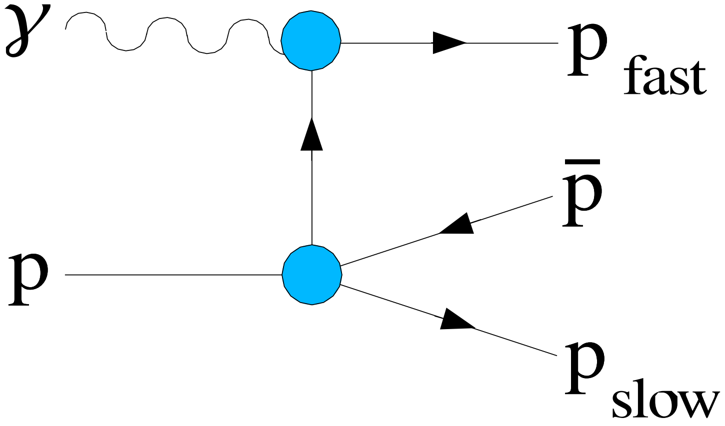

Figure 1.5. The baryon exchange diagram. In baryon exchange, a photon interacts with an exchange baryon, converting it to a fast forward-going proton. The produced proton is expected to have high momentum compared to the other decay products.

angular moments analysis is shown as part of the search for resonances decaying to proton-antiproton pairs. The results of the analysis are summarized in Chapter 10.

CHAPTER 2

BACKGROUND HISTORY AND THEORETICAL PREDICTIONS

2.1 History of Proton-Antiproton Studies

The proton-antiproton system has had a rich history spanning more than thirty years. In the late 1960s, there were claims of a meson resonance with a mass of 1.93 GeV/c^2 seen using a missing mass spectrometer at the European Center for Nuclear Research (CERN)[11]. In 1968, it was hypothesized that this narrow resonance was a baryonium particle when it was observed in a $p\bar{p}$ elastic scattering bubble chamber experiment at Brookhaven National Laboratory(BNL)[9]. This implies that it should be possible to produce the state in $p\bar{p}$ interactions and also observe it in $p\bar{p}$ decays. There were then claims that other experiments found the resonance in proton-antiproton scattering experiments [12][13][10]. Beginning in the late 1970s there were additional claims of higher mass resonances at 2.02 and 2.20 GeV/c^2 in the proton-antiproton system[14][15] [16]. However, subsequent experiments refuted these claims [17][18], and until recently the debate had diminished.

The resonances claimed by Benkheiri *et. al.* in 1977 [14] were significant because they were the first claims of a resonance decaying to a proton-antiproton pair. This experiment was performed using CERN's Omega spectrometer. In the reaction $\pi^- p \rightarrow \pi^- p_F p\bar{p}$, where p_F is a high momentum proton compared to the other particles, it was assumed that a resonance was produced through baryon exchange. They claimed observation of two narrow peaks (Fig.2.1), one at 2.020 and the other at 2.200 GeV/c^2. The 2.020 GeV/c^2 resonance had a significance of more than 6 standard deviations. The 2.020 GeV/c^2 resonance was reported to have a width of 24 ± 12 MeV/c^2. The width of the 2.200 GeV/c^2 resonance was 16^{+20}_{-16} MeV/c^2. The cross section of the 2.02 GeV/c^2 resonance was measured to be $30 \pm 12nb$.

Other experiments with lower statistics supported the 2.020 GeV/c^2 resonance[15] [16], but an experiment at BNL [18] refuted these claims. The BNL experiment observed approximately 7000 events of the type $\pi^- p \rightarrow \pi^- p_F p\bar{p}$. They did not observe resonances, and an upper limit of 3nb was placed on the resonance cross section.

The first experiment to produce proton-antiproton pairs via photoproduction used the 7 GeV Electron Synchrotron DESY at Hamburg in 1983 [16]. The experiment recorded 230 events of the type $\gamma p \rightarrow pp\bar{p}$. The experiment claimed to observe a $p\bar{p}$ resonance with a mass of 2.024 GeV/c^2 with a width of 27 MeV/c^2, and a cross section of $14 \pm 5nb$. The total $p\bar{p}$ cross section measured by DESY is shown in Figure 2.2. Note that the DESY experiment analyzed the same reaction as in the E01-017 $\gamma p \rightarrow pp\bar{p}$ analysis. DESY also ran with a photon beam energy from 4.7 to 6.6 GeV, which is comparable to that of E01-017, which ranged from 4.8 to 5.5 GeV. These similarities make the DESY results ideal for comparison to the results of the E01-017 analysis.

CERN performed a followup experiment to the one which observed resonances in 1977[19]. In 1997, CERN published results which refuted their earlier claims of the 1.93 and 2.02 GeV/c^2 resonances. Yet in 1999, a reanalysis of the same data resulted in the confirmation of the existence of the 2.02 and 2.2 GeV/c^2 resonances [20]. The claim of this new analysis was that certain kinematic cuts were necessary to favor the production mechanism of the resonance. Ferrer *et. al.* claimed that the resonance production occurred in a central production mechanism, as shown in Figure 2.3. Various kinematic cuts were used to enhance the signal in central production mechanisms. In the $p\bar{p}$ rest frame of a central production mechanism, an

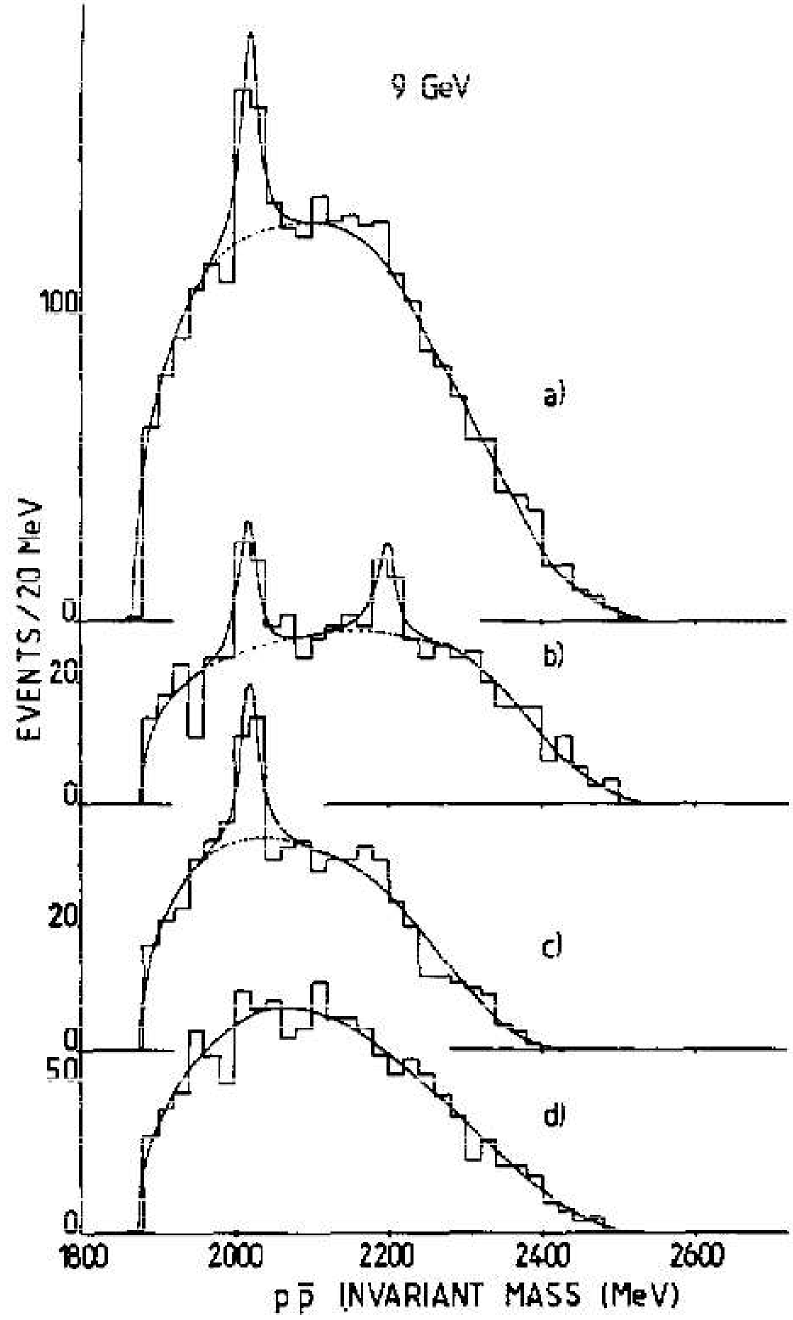

Figure 2.1. The $p\bar{p}$ invariant mass spectrum from $\pi^- p \rightarrow \pi^- p_F p\bar{p}$ events taken at the CERN Omega spectrometer. a) The entire data sample. b) Events in which the $\pi^- p_F$ mass is in the range of the $\Delta(1232)$. c) Events in which the $\pi^- p_F$ mass is in the range of the $N^0(1520)$. d) The events excluded by b) and c).

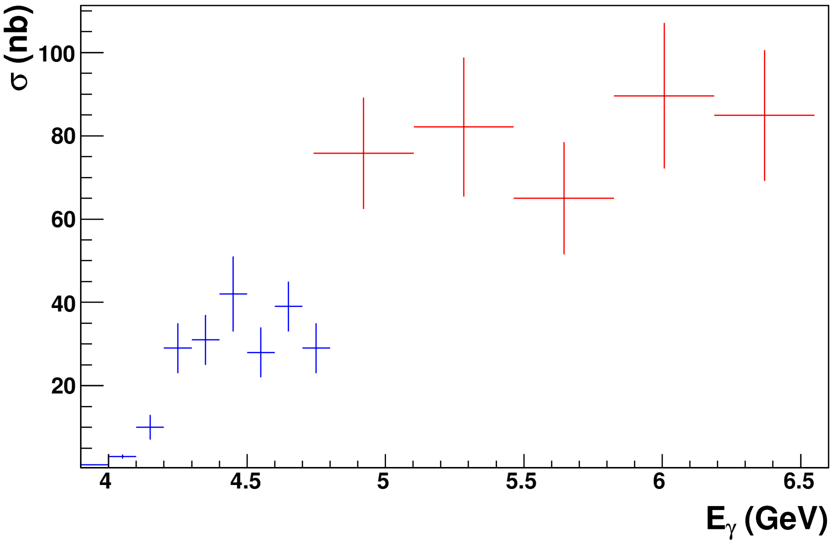

Figure 2.2. Total cross section of $\gamma p \to pp\bar{p}$ as a function of photon energy. The figure shows the results from DESY(red) and NINA(blue). The results of this analysis will be directly compared to those of the DESY experiment.

exchange proton and an exchange antiproton head towards each other. After forming a resonance, the decay has no preferential angular distribution. The other final state particles are either moving in the direction of the beam or in the direction of the target. The kinematic cuts were used to enhance this mechanism, and to reduce mechanisms in which most of the final state particles move in the beam direction. It was shown that the 2.02 GeV/c^2 resonance was enhanced by these cuts.

Presently, the only well-known particle that decays to proton-antiproton is the J/ψ particle, which has a mass of 3.097 GeV/c^2 [5]. Recently, the BES collaboration claimed the observation of a baryonium state seen in radiative J/Ψ decays [21]. The claimed state appears as an enhancement in the $p\bar{p}$ invariant mass spectrum near threshold as shown in Figure 2.4.

Recently, Jefferson Laboratory observed the photoproduction of proton-antiproton pairs. Experiment E99-001, an experiment to search for unusual mesons, observed approximately 2000 events of the reaction $\gamma p \to pp\bar{p}$[8]. A preliminary study of this

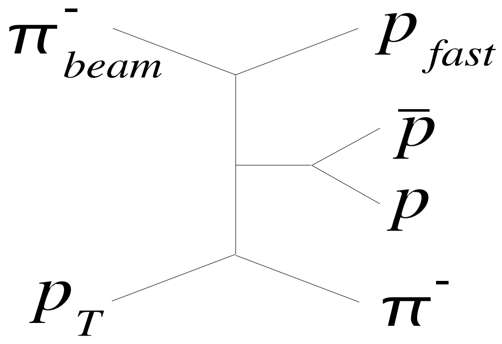

Figure 2.3. Central production of a $p\bar{p}$ state in $\pi^- p$ interactions. This is the production mechanism claimed to produced the narrow 2.02 GeV/c^2 resonance by Ferrer *et. al.*[20]

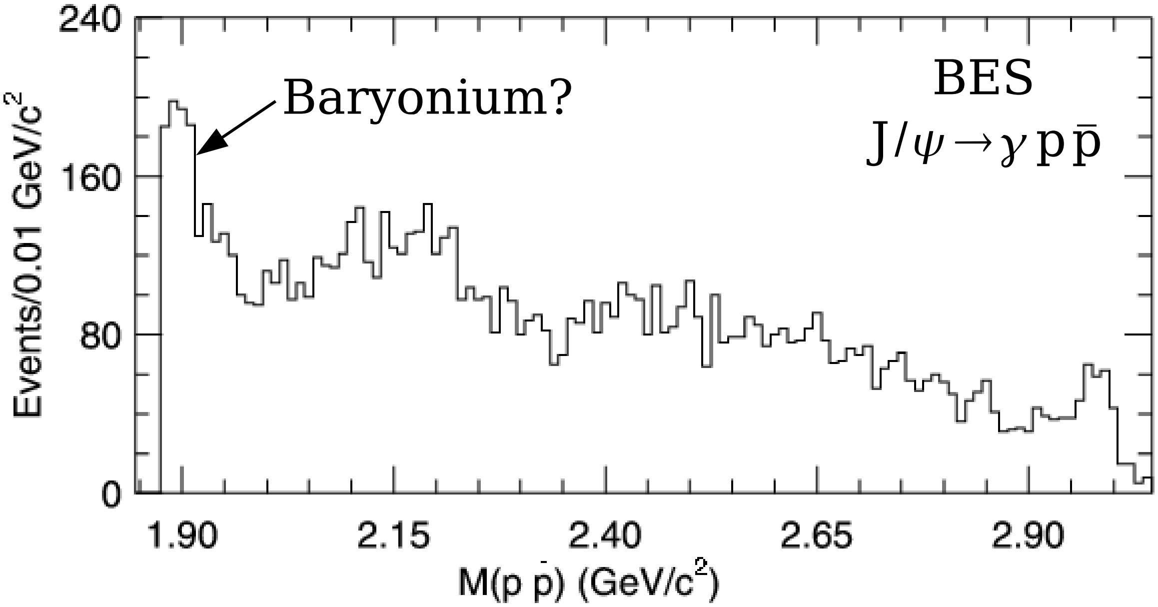

Figure 2.4. The $p\bar{p}$ invariant mass distribution for the $J/\Psi \rightarrow \gamma p\bar{p}$ reaction at BES[21]. The enhancement seen at 1.90 GeV/c^2 is claimed to be a sub-threshold baryonium resonance.

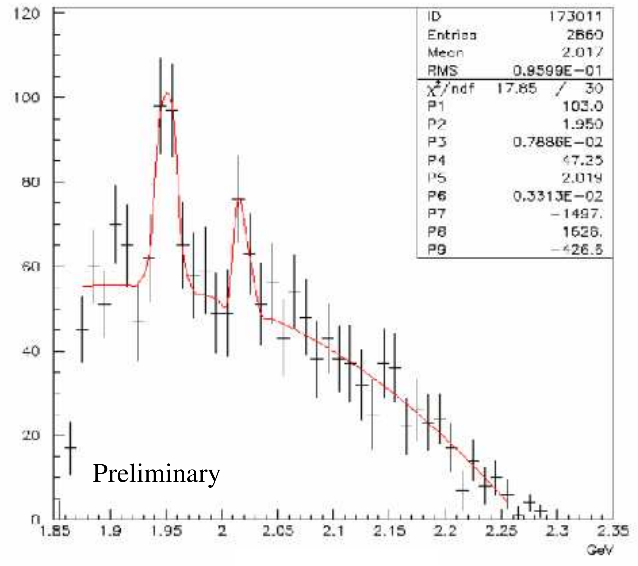

Figure 2.5. The $p_{slow}\bar{p}$ invariant mass spectrum, from CLAS Analysis Note 2001-001 by V. Koubarovsky, M. Battaglieri, and M. Ripani. An enhancement was observed at a $p\bar{p}$ invariant mass of 2.02 GeV/c^2. An enhancement was also observed at 1.95 GeV/c^2.

data suggests a possible resonant structure at 2.02 GeV/c^2, consistent with earlier observations (Fig. 2.5).

In 2001, Jefferson Lab Experiment E01-017 acquired a large sample of photoproduction events at beam energies of 4.8-5.5 GeV. E01-017 acquired more than 18,000 events of the reaction $\gamma p \rightarrow pp\bar{p}$. It is the analysis of this data which this dissertation is based. With such a data set, it may be possible for the first time to search for the existence of both narrow and broad resonances via the use of angular and kinematic dependence of the proton-antiproton system.

Historically, the $p\bar{p}$ system has a rich, but controversial, history of narrow resonance observations. The debate on the existence of these states has greatly lingered on due to a lack of statistics, supporting evidence, and conflicting experimental results. The source of proton-antiproton production in pion and photoproduction experiments is unexplained.

2.2 Quark Model Predictions

Originally, Fermi and Yang attempted to describe the pion as a nucleon-antinucleon state [22]. They found that the state would share many properties as those of the pion from Yukawa theory. In the 1970s, theorists associated $\bar{N}N$ states with new types of particles with masses near the $\bar{N}N$ threshold [23]. These theories were encouraged by many experimental results at the time. These states can generally be categorized into either quasi-nuclear baryonium or multiquark baryonium.

The quantum numbers of a proton-antiproton state are exactly the same as those for a quark-antiquark state since they are both Dirac fermions. Parity is $(-1)^{L+1}$, and charge conjugation is $(-1)^{L+S}$. Both particles have spin $= \frac{1}{2}$, so the total spin quantum number is $S = 0$ or 1. The allowed J^{PC} are 0^{++}, 0^{-+}, 1^{++}, 1^{+-}, 1^{--}, 2^{++}, 2^{-+}, 2^{--}, 3^{--}, and so forth. The set of J^{PC} quantum numbers which are not generated by this prescription ($J^{PC} = 0^{--}$,0^{+-},1^{-+},2^{+-},...) are not allowed. These J^{PC} quantum numbers also correspond to the exotic J^{PC} for mesons. These exotic quantum numbers are forbidden for $q\bar{q}$ mesons as well as for $p\bar{p}$ states.

2.2.1 Quasi-Nuclear Baryonium

A quasi-nuclear baryonium state is thought of as a six quark state in which the nucleon-antinucleon components interact via meson exchange [24]. Shapiro predicted that there would be 10-20 bound and resonant states with widths of 1-100 MeV. In formation experiments, these states would manifest themselves in radiative electromagnetic transitions from $p\bar{p}$-atomic Coulomb states to quasi-nuclear ones.

Dover *et. al.* attempted to interpret some experimental results as being $N\bar{N}$ resonances [25]. Dover used a One Boson Exchange model (OBEP) to explain the $N\bar{N}$ interaction. The OBEP model depended on exchange of mesons with well-defined G-parity. The $N\bar{N}$ potential $V_{N\bar{N}}(r)$, was constructed from the NN potential by inverting the signs of those terms corresponding to exchange of mesons of odd G-parity. In this model, the ω-exchange potential (G=-1) became attractive, whereas it is repulsive in NN systems. From this model, Dover predicted that strong tensor forces would produce $I = 0$ high-spin states $(3^-, 4^+, 5^-)$ relatively near the $\bar{N}N$ threshold [26].

2.2.2 Multiquark States

The Quark Model provides a simple scheme for resonances assumed to be $Q\bar{Q}$ states. The meson resonances lie on Regge trajectories which were developed from the ground state $Q\bar{Q}$ configurations by adding angular momentum [27]. The difficulty for $Q^2\bar{Q}^2$ configurations is the large number of states. Jaffe cataloged these states and used the MIT bag model to estimate Regge slopes and intercepts. Jaffe then used the ${}^3P_0$ model to estimate the couplings of $Q^2\bar{Q}^2$ states to $N\bar{N}$. The ${}^3P_0$ model simply uses vacuum quantum numbers for a $q\bar{q}$ pair produced from the vacuum[28].

The MIT Bag Model describes multiquark hadrons and ordinary mesons ($Q\bar{Q}$) and baryons (Q^3) using the same dynamics. For a $Q\bar{Q}$ system, the bag contains a quark antiquark pair interacting through the color-electric flux. For large angular momentum, the flux carries most of the angular momentum and energy. The slope of the Regge trajectory is determined by the magnitude of the color flux which depends on the color charge at each end. For ordinary mesons and baryons, the SU(3) color representation on either end is always a $\mathbf{3}$ or $\bar{\mathbf{3}}$, hence $Q\bar{Q}$ and Q^3 trajectories have the same slope.

For $Q^2\bar{Q}^2$, two quarks at one end can couple to a $\bar{\mathbf{3}}$ or $\mathbf{6}$ as shown in Figure 2.2.2. A $Q\bar{Q}$ pair at the end can couple to a $\mathbf{1}$ or $\mathbf{8}$. Thus three families of $Q^2\bar{Q}^2$ are possible, with differing Regge slopes.

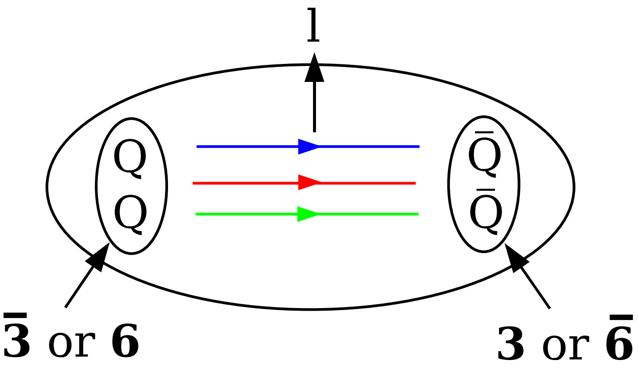

Figure 2.6. The $Q^2\bar{Q}^2$ system with a diquark and antidiquark at each end. The diquark can assume the color representations $\bar{\mathbf{3}}$ or $\mathbf{6}$.The angular momentum barrier suppresses the coupling to mesons.

$$\bar{\mathbf{3}} - \mathbf{3}$$

$$\mathbf{6} - \bar{\mathbf{6}}$$

$$\mathbf{8} - \mathbf{8}$$

From this picture the $\bar{\mathbf{3}} - \mathbf{3}$ and $\mathbf{6} - \bar{\mathbf{6}}$ states are predominantly $N\bar{N}$ resonances. Coupling to mesonic final states is suppressed by an angular momentum barrier.

The $Q^2\bar{Q}^2$ states which couple to $N\bar{N}$ have two quarks at one end and two antiquarks at the other. Two quarks in the same spatial state must be antisymmetric under exchange of color, spin, and flavor. If they are antisymmetric in color ($\bar{\mathbf{3}}$) , then they must be symmetric in both spin and isospin or antisymmetric in both spin and isospin. If they are symmetric in color ($\mathbf{6}$) they may be either symmetric in spin and antisymmetric in isospin or vice versa. States in which a $Q\bar{Q}$ pair sit at each end of the bag do not couple to $N\bar{N}$.

$Q^2\bar{Q}^2$ states in the $\bar{\mathbf{3}} - \mathbf{3}$ configurations lie on trajectories with the same slope as ordinary $Q\bar{Q}$ and Q^3. For $\mathbf{6} - \bar{\mathbf{6}}$ configurations, the trajectory has a smaller slope which results in the masses being more widely spaced. However, for low angular momentum, mixing occurs between the $\bar{\mathbf{3}} - \mathbf{3}$ and $\mathbf{6} - \bar{\mathbf{6}}$ trajectories, which implies curvature in those trajectories. This does not occur in $Q\bar{Q}$ or Q^3. At high angular momentum, the diquark and antidiquark separate and mixing stops.

From the $^3P_0$ model, it is assumed that the annihilating $Q\bar{Q}$ pair have vacuum quantum numbers ($J^P = 0^+$,$I = 0$,color singlet) and the other quarks remain in the same configurations. The result is that the $\mathbf{6} - \bar{\mathbf{6}}$ trajectories decouple from the $N\bar{N}$ system.

Several families of $Q^2\bar{Q}^2$ states are possible, but only the $\bar{\mathbf{3}} - \mathbf{3}$ configurations should couple strongly to $N\bar{N}$. These states have been dubbed the "true" baryonium states. The $\mathbf{6} - \bar{\mathbf{6}}$ configurations, the "mock" baryonium, couple weakly to both $N\bar{N}$ and mesons, but are difficult to form in $N\bar{N}$ scattering. They may couple more strongly to production processes, and may be candidates for narrow states. If the quark-model classification scheme applies to the $Q^2\bar{Q}^2$ sector, then hundreds of $N\bar{N}$ resonances in the region between 1.6 and 3.0 GeV await discovery.

2.3 Momentum Exchange Variables

Possible production mechanisms which describe the photoproduction of a proton-antiproton pair are diffraction/meson exchange, baryon exchange, and antibaryon exchange. In each process, an intermediate resonance may be produced. We can search for these states first as structures in the invariant mass and angular distributions. In peripheral production, the photon interacts with an exchange particle which transfers little momentum to the target proton. The photon interaction produces a resonance which decays to a fast forward-going proton-antiproton pair. In baryon exchange, the photon interacts with an exchange baryon converting it to a fast forward-going proton leaving behind a slow moving resonance at the target vertex. The slow moving resonance then decays to a proton-antiproton pair. For antibaryon exchange, it is assumed that the photon interacts with an exchange antibaryon converting it to a

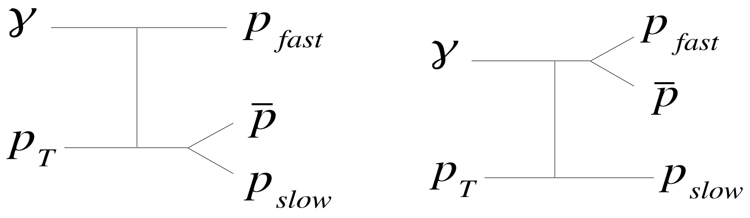

Figure 2.7. The Feynman diagrams for baryon exchange (left) and meson exchange (right). The proton with the most momentum was assumed to be associated with the top vertex for both production mechanisms.

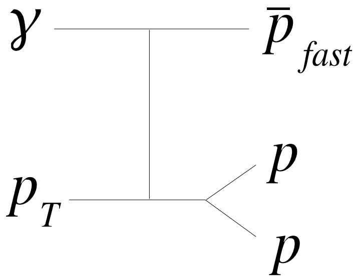

Figure 2.8. The Feynman diagram for antibaryon exchange. It was assumed that the antiproton would have the most momentum of the three particles for this type of production mechanism.

fast forward-going antiproton, leaving behind a resonance at the target vertex which decays to two protons.

A difficulty arises in the distinction of meson exchange and baryon exchange production due to having identical protons in the final state. To be fully correct, one needs to antisymmetrize the production amplitude with respect to exchange of the protons because they are indistinguishable. But using kinematic signatures, one can distinguish the protons to a good degree. For antibaryon exchange, it does not matter since both protons are at the same decay vertex.

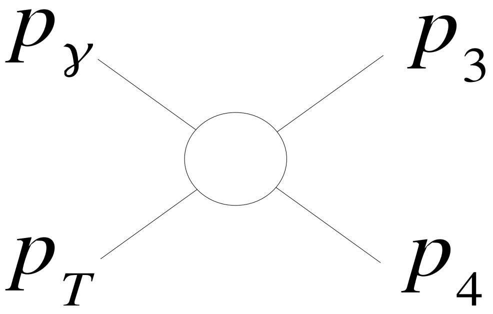

Figure 2.9. The two-body reaction diagram. This diagram illustrates how the Mandelstam variables are defined. P_3 and P_4 are defined differently for meson and baryon exchange.

The protons were labeled according to their momentum. In both meson and baryon exchange processes, the proton produced at the photon vertex (figure 2.3) is expected to have more momentum than the proton at the target vertex. Therefore, the proton with the greatest momentum will be associated with the proton at the photon vertex and labeled p_{fast}. The proton with the least momentum will be associated with the proton appearing at the target vertex and labeled p_{slow}.

The momentum exchange variables used in this analysis are defined by the Mandelstam variables s, t, and u. Mandelstam variables are defined for a two-body final state, whereas this reaction has a three-body final state. The Mandelstam variables can be defined by assuming a $\bar{p}p$ system as shown in Figure 2.3. Using the standard definitions, the variable are defined by

$$s \equiv (p^\mu_\gamma + p^\mu_{p_T})^2.$$

$$t \equiv (p^\mu_\gamma - p^\mu_{P_3})^2.$$

$$u \equiv (p^\mu_\gamma - p^\mu_{P_4})^2$$

For meson exchange, define P_3 and P_4 as

$$P_3^{meson} \equiv p^\mu_{p_{fast}} + p^\mu_{\bar{p}}$$

$$P_4^{meson} \equiv p^\mu_{p_{slow}}$$

Whereas for baryon exchange define P_3 and P_4 as

$$P_3^{baryon} \equiv p^\mu_{p_{fast}}$$

$$P_4^{baryon} \equiv p^\mu_{p_{slow}} + p^\mu_{\bar{p}}$$

Therefore, the magnitude of the four-momentum exchange for meson and baryon exchange are

$$t^{meson} \equiv (p^\mu_\gamma - p^\mu_{p_{fast}} - p^\mu_{\bar{p}})^2.$$

$$t^{baryon} \equiv (p^\mu_\gamma - p^\mu_{p_{fast}})^2.$$

Additionally, the minimum values of t due to kinematic limitations are

$$t^{meson}_{min} \equiv \frac{m^4_{P_3^{meson}}}{4s} - (E^{CM}_\gamma - p^{CM}_{P_3^{meson}})^2$$

$$t^{baryon}_{min} \equiv \frac{(m^2_{P_4^{baryon}} - 2m_p^2)^2}{4s} - (E^{CM}_\gamma - p^{CM}_{P_3^{baryon}})^2$$

CHAPTER 3

THE EXPERIMENT

3.1 Overview

The experiment was performed at Thomas Jefferson National Accelerator Facility in Newport News, VA. Jefferson Lab is the location of CEBAF, the Continuous Electron Beam Accelerator Facility. CEBAF is capable of delivering three separate beams of electrons with energies up to 6 GeV to detector halls A, B, and C [29]. Hall A contains two high resolution magnetic spectrometers for the simultaneous detection of scattered electrons and hadrons. Hall C is equipped with two medium resolution spectrometers which have complementary momentum ranges. The data presented in this dissertation were taken at Hall B, using the CEBAF Large Acceptance Spectrometer (CLAS).

3.2 The Accelerator

Jefferson Lab's Continuous Electron Beam Accelerator Facility (CEBAF) uses a racetrack design in which two anti-parallel LINACs and recirculating magnet arcs are used to accelerate electrons up to an energy of 6 GeV (see Figure 3.1). Electrons are injected into the accelerator with an energy of 45 MeV. The beam can be polarized using the polarizing electron gun [30]. The polarized electrons are produced by illuminating a GaAs photocathode crystal with circularly polarized laser light. Three independent lasers are synchronized and combined to illuminate the photocathode emitting a 1497 MHz pulse train of electrons [31]. Two meters downstream, an RF buncher cavity chops the beam to compensate for space charge effects at higher beam currents. The beam currents span a large dynamic range of 100pA to $100\mu A$. Each of the three beams are delivered to their respective halls at a frequency of 499 MHz, or one pulse per 2.004 ns. The electrons are accelerated by two LINACs which consist of eight cryomodules, each of which contain four pairs of five-cell, 1497 MHz niobium accelerating cavities.

Electrons are first injected into the accelerator by an electron gun, and are then accelerated by a LINAC. The electrons are then redirected by the first of a set of magnet arcs and pass through the second LINAC. Additional sets of magnet arcs allow for this process to be repeated up to four more times by recirculating the electrons through the LINACs. Each beam can obtain a multiple up to five, of the initial lap energy. After the electrons are accelerated, the beams are split into the three halls. Due to the small amount of synchrotron radiation, the spread in the beam energy is only $\frac{\delta E}{E} < 10^{-4}$.

3.3 The CEBAF Large Acceptance Spectrometer

The CLAS detector is mainly designed to measure the momentum, time of flight and path length of charged particles produced when a beam photon or electron interacts with the target (see Figure 3.2). The detector uses a toroidal magnet used to bend the paths of charged particles away from, or towards, the beam line. Drift chambers measure the momenta and path lengths of charged particles while time-of-flight(TOF) scintillator counters measure the time a particle is detected. The Start Counter near the target used in photon beam runs, obtains the event start time. Combining this information, the particle's velocity(β) can be measured and used to calculate the mass of the particle. A Cherenkov detector is employed to differentiate between certain charged particles. The Forward Electromagnetic

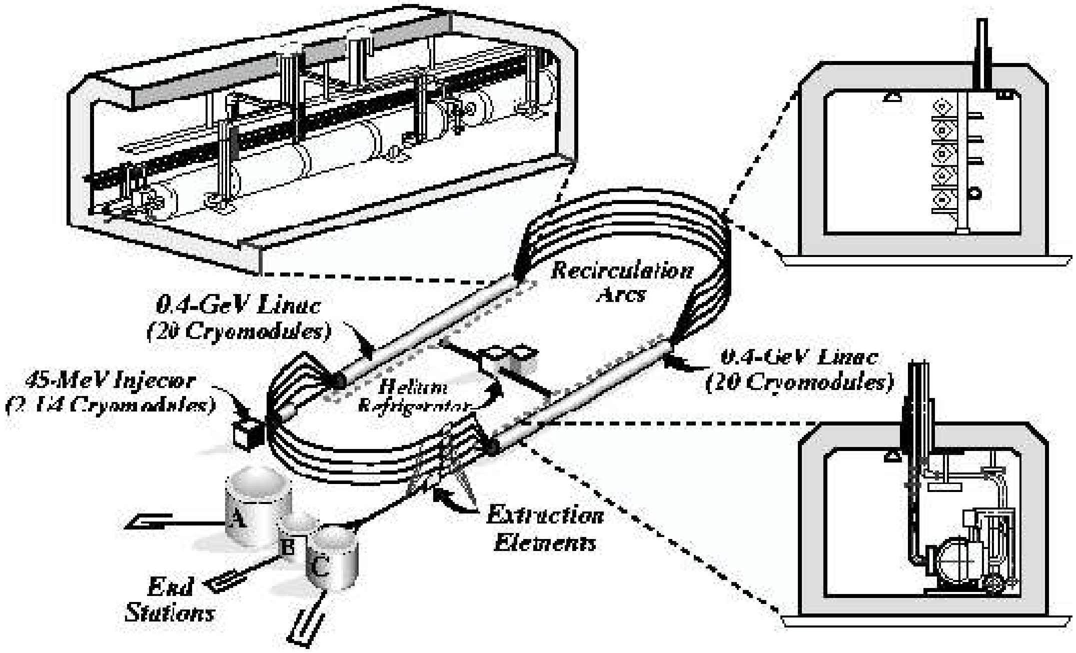

Figure 3.1. CEBAF at Jefferson Laboratory. Electrons start at the injector and pass through the LINAC toward the top left of the image. The electrons are circulated by one of the magnet arcs and pass through the second LINAC. The electrons can be recirculated up to four more times before being inserted into one of the halls.

Calorimeter is used to detect electrons and neutral particles. A detailed description of the CLAS apparatus is given in Reference [29].

3.3.1 Torus Magnet

The torus magnet consists of six superconducting coils. The coils are cooled to 4.5K using supercritical helium. Field lines are generated in the azimuthal direction surrounding the beam line as shown in Figure 3.3. This preserves the azimuthal angle of charged particles traversing the magnetic field. Charged particles bend away or

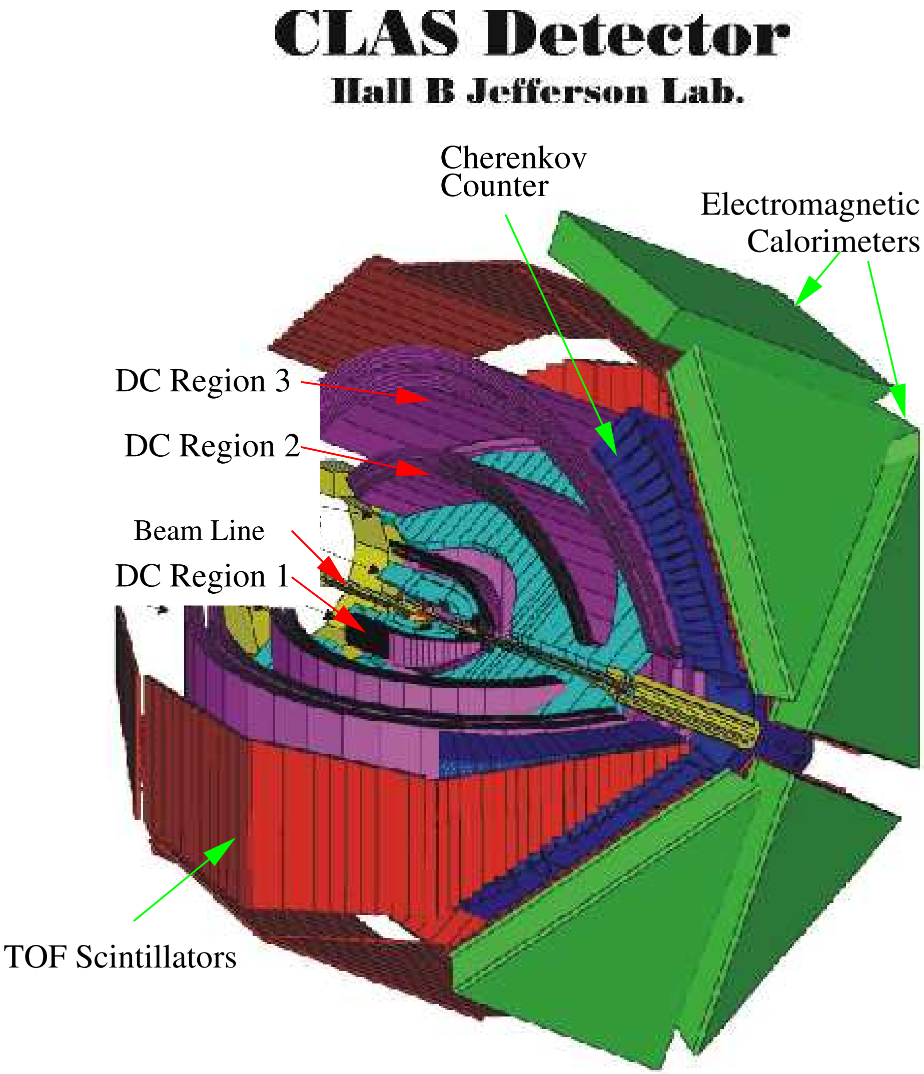

Figure 3.2. A cutaway view of the CLAS detector. Charged particles are bent by the torus magnet (cyan) and tracked by the drift chambers (purple). Their time of flight is then measured by the scintillator counters (red). Cherenkov counters (blue) are used for further particle identification. The electromagnetic calorimeters (green) detect electrons, photons, and neutrons.

towards the beam line, depending on the charge and torus current setting. The magnet is designed so that the magnetic field can be reversed. The magnet contains no iron, which would become magnetized, thus the field can be accurately calculated directly from the torus current.

The kidney-shape geometry results in a high field integral for forward-going particles, and a lower integral for particles emitted at larger angles. At a maximum current of 3860A, the maximum field reaches 3.5 T in the forward direction. The current used for E01-017 was 1938A. The coil geometry also preserves a field-free region near the center of CLAS for the operation of a polarized target.

The six coils of the torus magnet define much of the geometry of the CLAS detectors. The coils create regions in which particles may not be detected. Therefore, the electronics and structural components of many of the CLAS detectors are placed in these regions. This results in the six symmetric sectors of the CLAS detector.

3.3.2 Drift Chambers

Drift chambers are used to track charged particles as they bend in the CLAS magnetic field [32]. The CLAS detector has eighteen drift chambers located at three radial positions in each of the six sectors. The “Region One”(R1) chambers surround the target in a region of low magnetic field. The “Region Two”(R2) chambers are between the torus magnet coils in a region of high magnetic field. The “Region Three”(R3) chambers are located outside the torus magnet coils. A drift chamber has two endplates placed parallel to neighboring torus coils, with thousands of high voltage wires stretched between them.

A row of wires make up a layer. Each successive layer is placed so that the wires are shifted by half the distance of the spacing between individual wires. A pattern of two layers of field wires followed by a layer of sense wires creates a honeycomb structure in which each “cell” consists of six field wires surrounding one sense wire (Figure 3.4). The honeycomb structure improves the track reconstruction

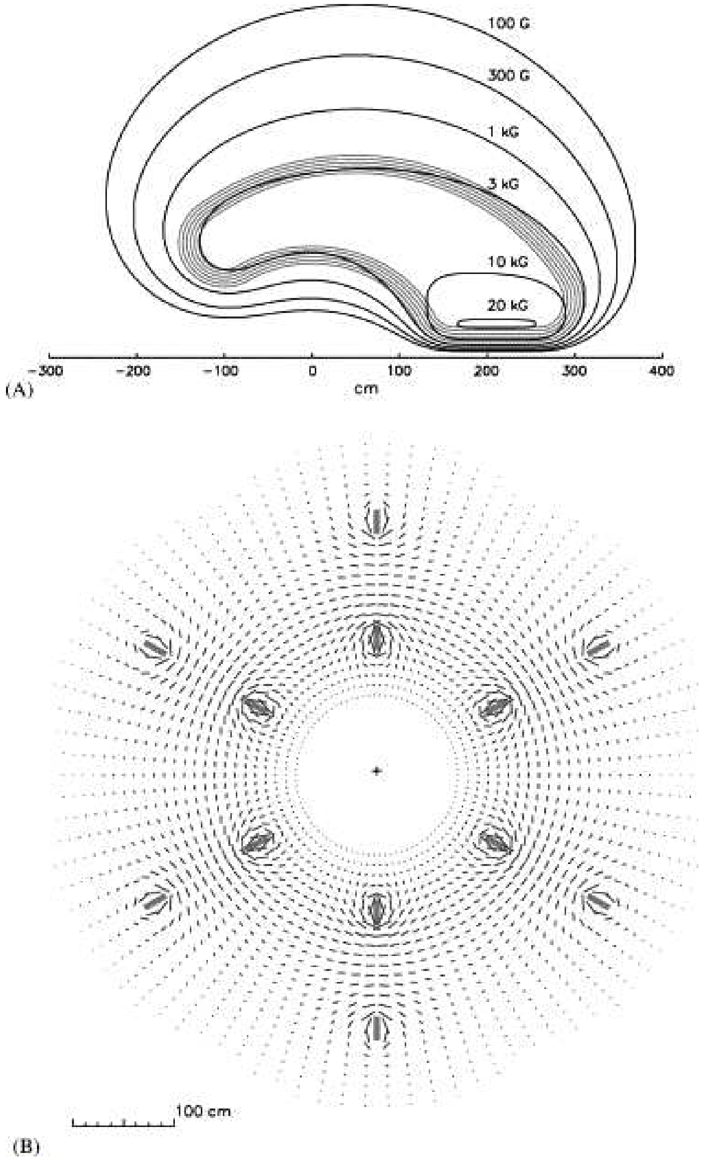

Figure 3.3. A: Contours of constant absolute magnetic field for the CLAS toroid in the midplane between two coils. The field strength is shown for a current much larger than that used in the g6c experiment. The current used for this experiment was 1938A. B: Magnetic field vectors for the CLAS toroid transverse to the beam in a plane at the center of CLAS. The length of each line segment is proportional to the field strength at that point. The six coils are seen in cross-section.

by discriminating which side of the sense wire a particle passed in an individual cell. Each R1 sector has 1296 drift cells, R2 has 2262 cells, and R3 has 2304 cells.

Sense wires are maintained at a positive potential, while field wires are placed at negative potential with the absolute value at half the sense-wire potential. Each drift chamber consists of two superlayers, each of which is made up of several wire layers. The superlayers are tilted at a six degree angle to one another to provide azimuthal information.

The drift chambers are filled with a gas consisting of 88% argon and 12% CO_2. When charged particles traverse a cell, the gas becomes ionized and "drifts" towards the sense wire. Each sense wire is attached to a pre-amplifier which delivers the signal to a post-amplifier and discriminator board (ADB) which produces digital output pulses. The pulses are then input into a time-to-digital converter (TDC) board.

The distance-of-closest approach (DOCA) of a track to the sense wire is a function of the drift velocity and the time it takes for ions to drift to the sense wire. This DOCA value is used to obtain initial tracks. For each cell, there is an ambiguity as to which side of the sense wire the track passed by. To resolve this, the χ^2 values for each of the initial tracks are compared. The set of tracks contains every left-right combination possible. The DOCA value for each cell is reobtained by fitting a track to hits in cells excluding the one being fit and calculating the distance from the track to the sense wire.

3.3.3 Time of Flight Scintillators

The time-of-flight(TOF) scintillators are made using Bicron plastic scintillator which radiates when traversed by ionizing charged particles. The scintillator thickness of 5.08cm was chosen to produce large signals from traversing minimum-ionizing particles. The photon pulses which are emitted by the scintillator are absorbed by photomultiplier tubes (PMTs) to collect the signal.

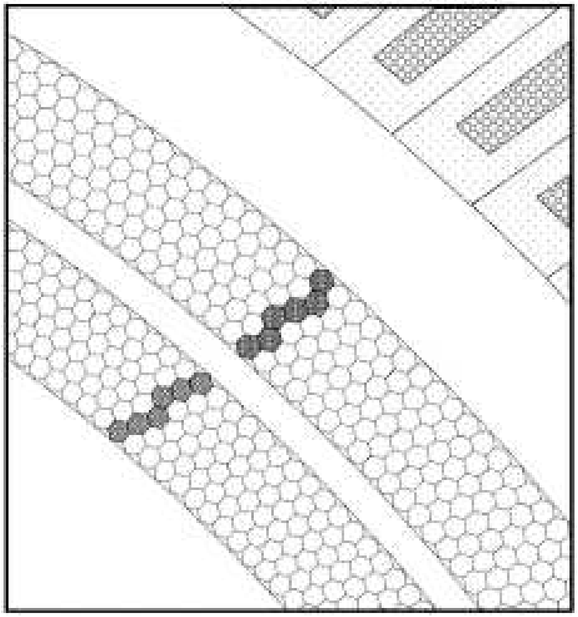

Figure 3.4. Representation of a portion of a drift chamber, showing the layout of its two superlayers. Sense wires with positive potential are at the center of each hexagonal cell and field wires at negative potential are at the vertices. A charged particle traversing the cell ionizes a gas which fills the drift chamber. The ions then drift towards the sense wire. Hits in neighboring cells are used to determine which side of the sense wire a particle passed.

In CLAS, the TOF scintillators are located radially outside the drift chambers and Cherenkov counters, but in front of the calorimeters. The averaged distance from the scintillators to the center of CLAS is 5m. The TOF scintillators for each sector are divided into 58 scintillator paddles which range from 32-445cm long. Each sector is divided into four panels. The forward panel scintillators are 15cm wide, whereas the three large-angle panels have 22cm wide scintillators. Each scintillator paddle has a PMT readout at each end. Using the time difference between signals in the two PMTs allows for the determination of the distance from the PMTs to the hit. The large-angle scintillators are connected to bent light guides which are then connected to the PMTs. In order to reduce cost, the paddles of the largest-angle panel are paired into single PMT readouts.

The TOF counters generate prompt signals for the CLAS trigger electronics as well as signals for pulse-height and timing analysis. The trigger depends on a threshold energy deposited in the TOF counters. The typical time resolution of the TOF is 150-200ps. Figure 3.5 shows the TOF resolution by comparing the TOF vertex time to the vertex time obtained from the Start Counter, which is described in the following subsection. The TOF is calibrated using cosmic-rays and UV lasers.

Cosmic-rays are used by placing two reference scintillator counters above and below the test scintillator [33]. Using coinciding hits in all three scintillators, the timing fluctuations are eliminated. UV lasers are used to simulate the scintillator response to an ionizing particle. The laser light is injected into the center of each scintillator paddle to measure the time resolution. This method eliminates any timing resolution problems which are common to both PMTs.

3.3.4 Start Counters

The start counters are intended to provide a signal of a hadronic event in CLAS and to link this event with a hit in the tagger. The timing resolution must be good enough to determine which 2ns time interval the interacting photon occurred in. The counters consist mainly of three scintillator counters, each of which cover two sectors. The scintillators are oriented around the beamline near the target, with the light collected into PMTs upstream of the target. The downstream end of each scintillator paddle is bent towards the beamline to provide forward angle coverage. The achieved resolution of the start counters is 485ps as shown in Figure 3.5.

3.3.5 Cherenkov Counters

When a particle travels through a material faster than light does in that material, the particle will emit light in a forward-going cone. The CLAS Cherenkov detector is filled with the gas perfluorobutane (C_4F_{10}), which has an index of refraction of 1.00153. Using the momentum of a charged particle determined from the tracking

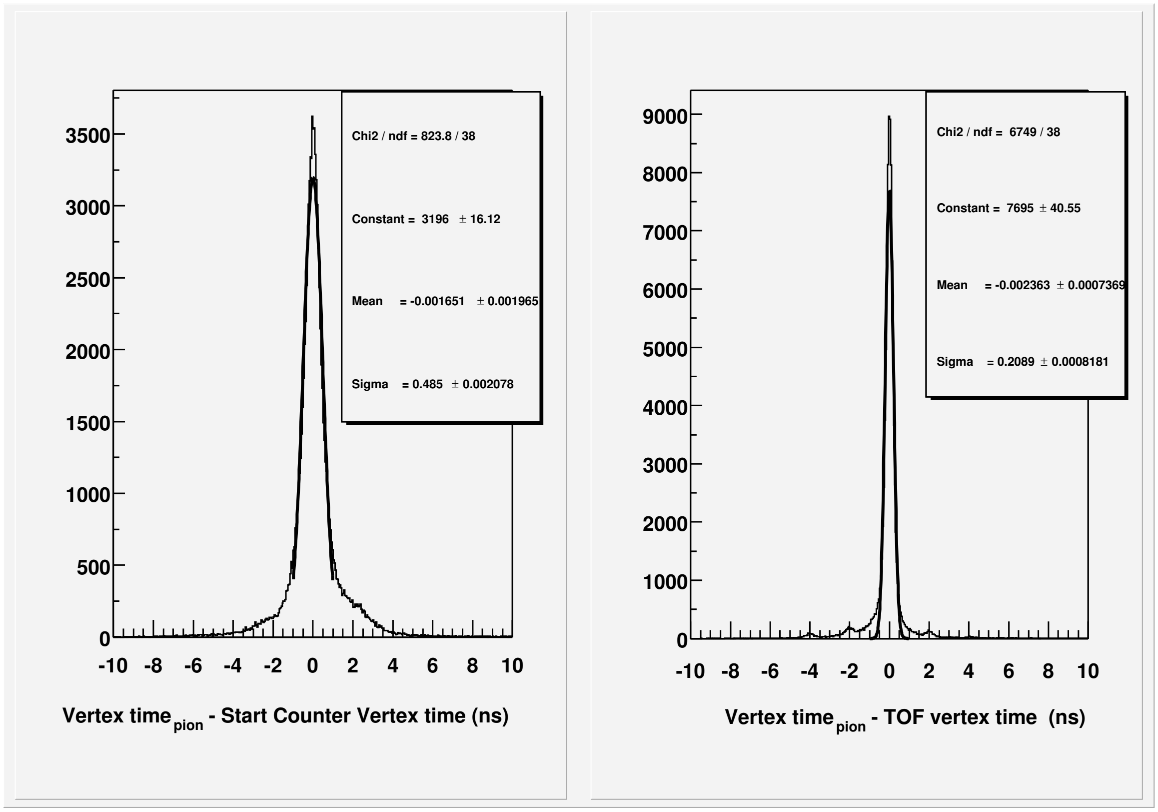

Figure 3.5. Left: The Start Counter (ST) timing resolution is obtained by comparing the ST vertex time to the vertex time determined by the Time-of-Flight(TOF). The ST resolution for this experiment was approximately 485ps. Right: The TOF timing resolution is determined by comparing the TOF vertex time to the tagger vertex time. The TOF resolution for this experiment was approximately 209ps.

system, the particle's identity may be determined by whether or not it emits Cherenkov light. More massive particles require more momentum to emit Cherenkov light. The minimum momentum for a pion to emit Cherenkov light in this detector is 2.5 GeV/c, therefore anything emitting Cherenkov light with less momentum must be an electron or positron.

The Cherenkov counters are used to trigger on electrons and to differentiate between electrons, pions, and kaons. The information from the Cherenkov counters was not used in this analysis because it wasn't necessary for proton identification. This detector mostly benefits experiments which utilize electron beams. The response

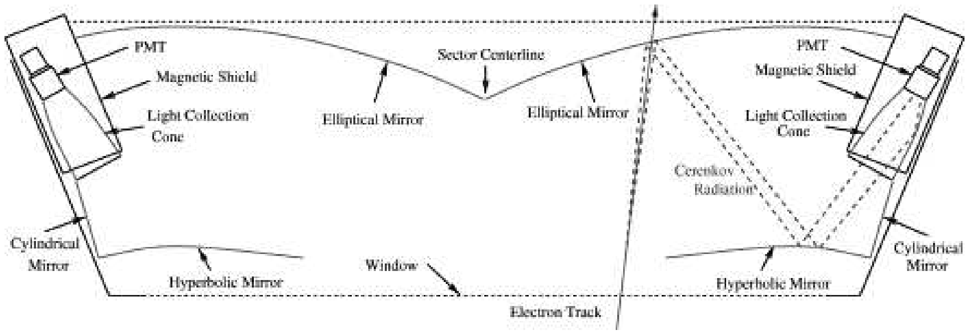

Figure 3.6. Schematic diagram of one Cherenkov segment, symmetric about the sector center. A particle with enough momentum emits Cherenkov light in a forward-going cone. The light first reflects off the elliptical mirror, and then onto the hyperbolic mirror. The light is then reflected into the light collection cone and the signal is measured by a PMT.

of a Cherenkov counter from a single photoelectron is used to calibrate the gain of the PMTs in terms of the number of photoelectrons. The Cherenkov counter in each sector is divided into 18 modules along the θ direction (see Figure 3.6). Each module is divided into two light collection devices along the sector midplane, so that there are a total of 36 light collection devices per sector. The light collection consists of one elliptical and one hyperbolic mirror to provide the primary focusing, a cylindrical mirror, and a light-collection cone connected to a PMT.

3.3.6 Electromagnetic Calorimeter

The Forward Electromagnetic Calorimeter is designed to detect and trigger on electrons at energies above 0.5 GeV, detect photons at energies above 0.2 GeV, and detect neutrons. The calorimeter has six sectors consisting of alternating layers of lead and scintillator (Fig. 3.7). Lead is used because it has a large number of electrons in each atom. The electrons generate a large electromagnetic field in the region near the atom.

When a high-energy electron enters the electromagnetic field of a lead atom, the electron can emit a Bremsstrahlung photon[34]. The photon can then Compton scatter an electron from another atom, or produce an electron-positron pair if it has enough energy. Each additional particle can in turn cause more particle emissions, thus creating a shower of particles. The particle shower passes into the scintillator. The scintillator absorbs the electromagnetic shower and then radiates. The scintillator light is then collected into PMTs to generate a signal. A high energy photon also interacts with the electromagnetic field of the lead atoms, transferring some energy to the atom while creating an electron-positron pair, which then showers into the scintillator.

Each triangular sector contains 39 lead/scintillator layers as shown in Figure 3.7. The sandwich design is employed to sample the particle's energy at intervals to provide better energy resolution. Each triangular layer of scintillator is divided into 36 strips parallel to one of the three edges. One end of each strip is connected to fiber optics for light readout. For each successive scintillator plane, the strip divisions are rotated by 120^0 to form the u,v, and w planes. The three directions of the scintillator paddles give hit position information by locating the intersection of paddles which were hit. The scintillators are connected to fiber optics for light collection into PMTs. To reduce the number of PMTs, the inner 5 layers and the outer 8 layers of a u,v, or w plane, are bundled together.

3.3.7 Target

The target for g6c was positioned 100cm upstream from the center of CLAS. Normally, CLAS experiments position the target at the center of CLAS. The position at -100cm was chosen to optimize the acceptance of charged particles for t-channel meson production. Most of the particles exiting the target move in a forward-going cone. The farther away from the beam line the particles get, the more likely they will be detected by CLAS. By moving the target upstream, the particles will get further away from the beam line, than for a normal target position. Thus the acceptance for forward-going particles is improved.

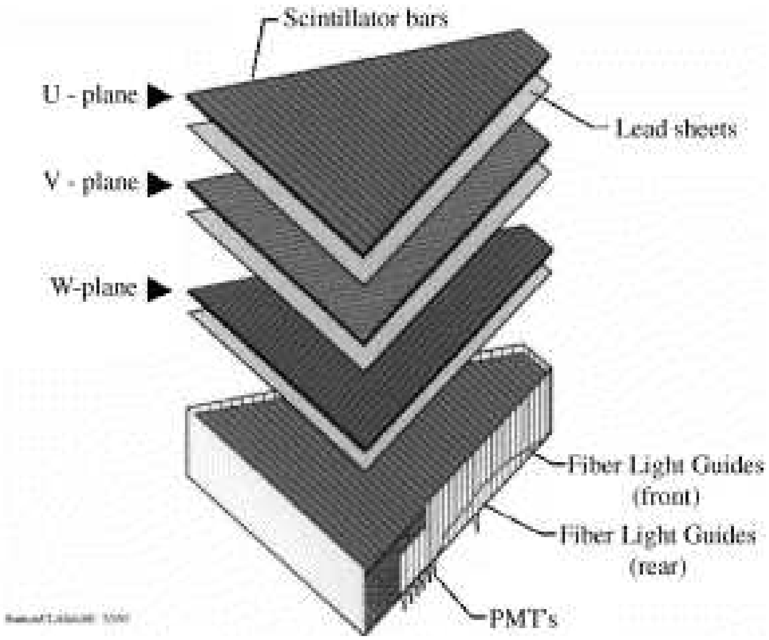

Figure 3.7. Exploded view of one of the six CLAS electromagnetic calorimeter modules.

The target for g6c was liquid hydrogen (LH_2). It was contained in a 18 × 3 cm cylindrical cell (Figure 3.8). The target cell wall is made of Kapton and has a window at each end[35]. A distribution tube at the base of the cell wall allows for LH_2 circulation. Epoxy film is used to seal all contact surfaces.

3.3.8 Photon Tagger

For photon experiments in CLAS, the photon beam is produced by placing a thin foil, called a radiator, in the electron beam which causes electrons to emit bremsstrahlung photons. The photon tagger measures the energy and timing information of the electron in order to determine the energy and time at the vertex for the bremsstrahlung photons[36]. For g6c, the radiator target was 3×10^{-4} radiation lengths thick of gold radiator material[37]. When an electron interacts with the radiator, it emits a bremsstrahlung photon, losing energy in the process. The photon tagger magnet then sweeps all the electrons away from the beam line. Electrons

Figure 3.8. The g6c target. The cell wall is made of Kapton film. A window at each end allows the beam to pass through. The tubes at the base allow for LH_2 to be circulated into the target cell.

which did not radiate go into a secondary beam dump, while those that did radiate are detected by a scintillator hodoscope.

The hodoscope consists of two planar arrays of plastic scintillators and PMTs as shown in Figure 3.9. The first layer of 384 overlapping scintillators provide energy resolution. The photon energy is then determined by the measured electron energy. The second layer of 61 large scintillators provide timing resolution to determine which 2ns RF beam packet the electron came from.

Each timing scintillator (T-counter) has a PMT connected to each end. The tagger is first calibrated by matching the timing values of the two PMTs for each T-counter. The T-counter timing is then identified with the timing from the energy scintillator counters (E-counters). This eliminates any systematic dependency on E-counters. Next, the T-counter timing is compared to timing from the accelerator. The accelerator timing is accurate to within a few picoseconds, and makes an excellent point of reference for timing. The calibration imposes the average electron time to

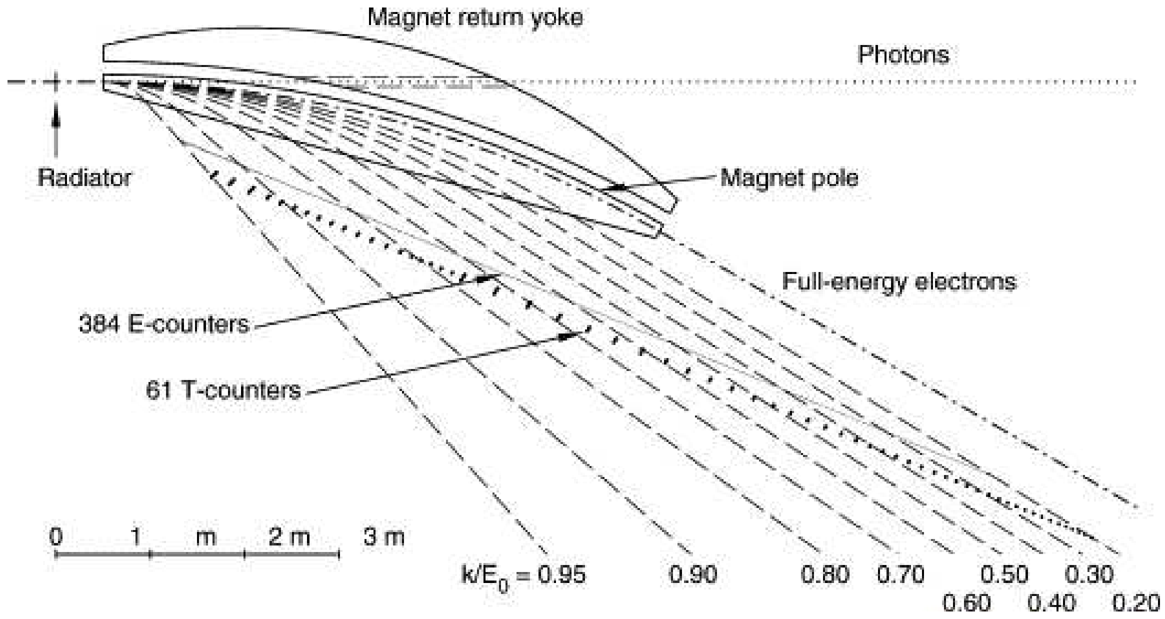

Figure 3.9. Hall B photon-tagging system. The electron is determined by the E-counters, which consist of a layer of 384 small overlapping scintillator counters. The timing is determined by the T-counters, which consist of 61 scintillator counters.

occur in the middle of a 2ns RF beam packet. However, it is possible to obtain the wrong 2ns RF beam packet. This would occur when the average electron time is closer to the wrong RF beam packet time. The error is corrected by comparing the T-counter's corrected time to the start counter timing. The T-counter time is shifted so that events occur at the same time a tagged photon goes through the target.

3.3.9 Radiator Target

The CLAS radiator targets are made at FSU[38]. They are made of a thin gold film with a carbon film for support. A sodium-chloride substrate is placed on a microscope slide and placed in an evaporator. An electron beam is used to create a gold vapor which condenses on the substrate. Using a Quartz crystal disk, the thickness of the gold film is measured. The RF resonant frequency of the Quartz disk is dependent upon how much mass is placed on one of its sides. The resonant frequency is approximately linearly dependent upon the thickness of the gold. The gold film is then placed in water to dissolve the substrate, separating the gold from the microscope slide.

3.4 Trigger and Data Acquisition

To acquire events of interest while minimizing deadtime, the g6c experiment employed a two level trigger. A trigger is a set of conditions which determine whether the data acquisition should record the data from the multiple CLAS detectors as an event. The first level trigger runs constantly, checking for events of interest. Events which pass the first level trigger are then processed by the second level trigger. Deadtime is the fraction of the time in which events which pass the first level trigger are not being queued for processing in the level two trigger. Events which occur during deadtime are lost due to computational limitations.

The g6c first level trigger required the incidence of a high energy tagged photon with hits in any two of the three start counter elements. The Level 1 trigger also required hits in at least two sectors of the time-of-flight elements. The second level trigger for g6c required two reconstructed charged particle tracks. Detector hit and track reconstruction will be described in Chapter 4.

The g6c experiment was interested in events caused by high energy photons[7]. To reduce deadtime, the tagger coincidence was limited to the top twelve tagger T-counters $(80\% - 95\%)E_0$ [37]. These T-counters correspond to photon beam energies in the 4.8-5.5 GeV range. This choice enhanced the collection of events with high end beam photon energies.

The data acquisition system can be viewed as a pipeline of processes that manipulates and transfers data. The process starts with the trigger and digital data conversion at the front-end and concludes with the data storage to RAID disks. A RAID(Redundant Array of Independent Disks) provides fault tolerance and improved performance over standard disk drives. The data from the various

Table 3.1. The MOR rate is the rate at which photons are tagged. The live time represents the amount of time the DAQ is ready to take more data.

Data Acquisition Rates	
Event Rate	1.7 KHz
Data Rate	$7.5MB/S$
MOR Rate	9.5 MHz
Live Time	$75-80\%$

detector components are digitized in FASTBUS and VME crates and collected by Readout Controllers[39]. This data is then sent to the control room where the data is assembled into complete events by the Event Builder. The events are then passed to shared memory which is used to monitor data quality, and to be picked up by Event Reconstruction which writes the events to local RAID disks.

The electron beam current for most of the g6c production runs was set at 40 nA, with few runs at 50 and 60 nA. The data rates in Table. 3.1 were recorded with the beam current of 40 nA. The event rate is the rate at which events pass the trigger and are recorded. The data rate is simply the event rate times the event size. For CLAS, the event size is on the order of 3-6kB. The maximum data rate is 25MB/s. The total tagger rate is called the master "or"(MOR). The MOR rate is the rate at which photons with energy 4.8-5.5 GeV are tagged by the photon tagger. The live time is the percentage of time the data acquisition is not processing events.

3.5 Run Conditions

The data for this analysis came from Jefferson Lab experiment E01-017 which was collected during the g6c running of CLAS (Aug. 17 - Sep. 11 of 2001). The entire experiment was run with the fixed electron beam energy of 5.744 GeV, the highest accessible energy at the time. To produce a photon beam from the electron beam, a thin gold foil radiator with 3×10^{-4} radiation lengths was used [37]. The tagger magnet was set at $I_{tagger} = 2097A$. The acceptance range of the tagger is $(20\%-95\%$

of the incident electron beam energy). This results in an available tagged photon energy in the range of 1.1-5.5 GeV. The trigger requirements of E01-017 required a tagged photon of at least 4.8 GeV. A photon collimator with a 2.8mm diameter was used downstream of the tagger to refine the photon beam. Following the collimator are sweep magnets used to clean up any charged particle background generated in the collimator walls.

The running conditions for this experiment were optimized for meson production recoiling off the neutron, decaying to $\pi^+\pi^+\pi^-$. In order to maximize the detection of the in-bending π^- particles, the experiment took data with the torus field set at half its maximum value $I_{torus} = 1938A$). The target was also moved upstream one meter to optimize forward-going peripherally produced mesons. The g6c running conditions are summarized in Table 3.2.

Table 3.2. Summary of running conditions for g6c. The trigger only included tagger T-counters 1-12, so that events would be recorded only when high energy photons (4.8-5.5 GeV) were tagged. [37]

Experimental Conditions Summary	
Electron Beam Energy	5.744 GeV
Electron Beam Intensity	$40(50)nA = 2.5 \times 10^{11}(3.125 \times 10^{11})e/s$
T-counters used in trigger	T1-T12
Tagger radiator (A)	density: 646 $\mu gm/cm^2$, rad. len.: 3×10^{-4} r.l.
Photon beam Energy	[1.1-5.5] GeV
Photon flux(tagging range:T1-T61)	$1.20 \times 10^8(1.45 \times 10^8)s^{-1}@40(50)nA$
Photon flux(trigger range:T1-T12)	$1.02 \times 10^7(1.28 \times 10^7)s^{-1}@40(50)nA$
Number of tagged photons	3.59×10^{12}
Sensitivity	2.743 events/pb
Tagger magnet current	2097 A
Torus magnet current	1938 A
Target material/size	$18 \times 3cmLH_2 = 7.58 \times 10^{23}atoms/cm^2$
Target position	-100 cm from center of CLAS
Luminosity	$7.58 \times 10^{30}(9.67 \times 10^{30})cm^{-2}s^{-1}@40(50)nA$
Photon collimator	2.8 mm
P.S. converter	0.01 r.l.
Events/Run	10M
Triggered events	1.16×10^9
Data volume	4.4TB
Runs	220
Run files	7313

CHAPTER 4

EVENT RECONSTRUCTION

For photon experiments a radiator foil is placed in the path of the electron beam to produce bremsstrahlung photons, as discussed in section 3.3.8. When the electron emits a photon it loses momentum and energy. As it passes through the tagger magnetic field, its radius of curvature depends on how much momentum it lost. The tagger uses the radius of curvature dependence to determine the electron momentum using a plane of energy and time scintillator counters. The 384 energy counters (E-counters) are arranged to determine the hit position of the electron on the plane, as shown in Figure 3.9. Using the position information and the tagger magnet setting, the E-counters are mapped to specific electron momenta, from which the photon energy is determined. After passing through the E-counters, the electrons hit a plane of 61 time counters (T-counters). For an electron to be tagged, it must hit an E-counter and a neighboring T-counter within 10ns. The accelerator delivers electron bunches every 2ns. Some of the electrons emit a Bremsstrahlung photon when they hit the radiator. For each T-counter, the average time values are calibrated such that they coincide with the nearest electron pulse from the accelerator. The time values are then used to determine the time at which the emitted photon arrived at the event vertex in the target. For a beam photon to be associated with an event detected in CLAS, the photon time at the event vertex must coincide with the CLAS event vertex time.

The resulting tagger information is used to determine at what times photons arrive at the target, and what energies they have. For the analysis of $\gamma p \rightarrow p p \bar{p}$, two protons must be detected by CLAS, and the position of their vertex must be within the target. As the protons pass through the target, they lose energy. The proton energies are corrected by adjusting the final momentum vectors of the protons according to how much material was traversed.

The protons must then pass through the Start Counters, which are scintillator counters placed at the center of CLAS to determine when the event began (see Section 3.3.4). Because the start counter paddles are not linear, the conversion from TDC values to start time values is complicated [40][41]. It is necessary to determine the location of tracks in each of the three paddles. The locations are determined from tracking by propagating the tracks backward to the start counter. For individual hits in the start counter, the best time is determined by the pulse-height weighted average time of the two tubes for one start counter paddle. For multiple particle hits in the start counter which occur within 10-15ns, tracking is used to determine the position of the hit and the nearest single-tube time is used, corrected to the hit position.

After the Start Counters, the protons are bent away from the beam as they traverse the magnetic field from the torus (see section 3.3.1). They must pass through the three Drift Chamber regions, which were described in section 3.3.2. The drift chamber data is a collection of TDC values from hits in individual drift cells. The first step of charged particle tracking is to find clusters of hits in each of the drift chamber (DC) superlayers [40].

A lookup table is used to find groups of hits or segments within a cluster which are consistent with a track traversing the superlayer. Track segments from individual superlayers are then identified with other segments using a look-up table. Once matches are found for at least five superlayers, the segment combination becomes a track candidate [41]. Using the linked track segments, a preliminary angle and momentum are assigned, and a trial track is swum through the CLAS magnetic field. At each layer the track passes through, the DOCA of the track to the hit wire or the position derived from the drift times is calculated. The track parameters are then adjusted to provide the best fit of the track to the measured positions.

The protons must then be detected by the time-of-flight(TOF) scintillator counters, which were described in section 3.3.3. The TOF is used to help determine the particle velocity (β). The particle velocity is determined by dividing the particle path length from the start counter to the TOF counter by the time difference between the TOF and the start counters. The momentum and velocity are used to determine the particle mass using

$$m = \frac{p}{\beta\gamma c}$$

A distribution showing β versus p for charged tracks is shown in figure 4.1. The curved bands correspond to differing particle masses.

$$\beta(p) = \frac{p}{(p^2+(mc)^2)^{\frac{1}{2}}}$$

The three most prominent bands in the figure correspond to pions, kaons, and protons. The small band below the protons are deuterons. The spurious points correspond to inefficiencies due to the TOF [42].

Once the particle velocity is determined, the particle track is propagated backward from the start counter to its vertex to determine the time at which the event began. This value is then matched with the timing of the tagged photons to determine which photon generated the event.

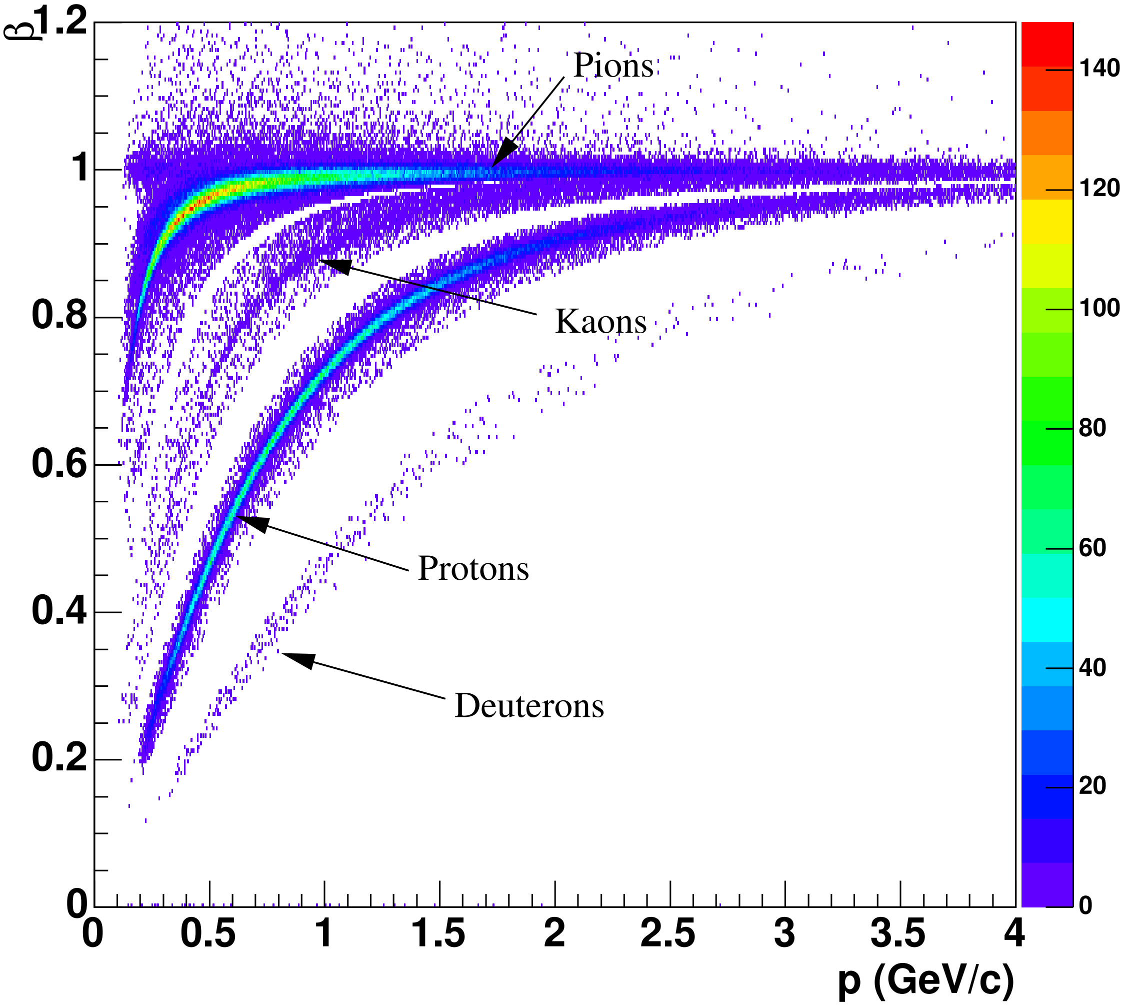

Figure 4.1. The figure shows β versus p for charged tracks. The curved bands correspond to differing particle masses, $\beta(p) = \frac{p}{(p^2+(mc)^2)^{\frac{1}{2}}}$The prominent bands from top-left to bottom right are pions, kaons, protons, and deuterons.

CHAPTER 5

DATA SELECTION

5.1 Introduction

This chapter covers the techniques used to ensure a high quality data set. For this analysis, a high quality data set would be one in which the momentum of the protons and the energy of the photons are well known, there would be no background, and the detector acceptance would be understood perfectly. Additionally, it is important to verify that the charged particles detected in the events are indeed protons, and that the selected photon is the one which caused the event. It is important to identify background sources and improve the signal to background ratio. The techniques covered include particle or mass identification, fiducial cuts, momentum and energy corrections, and kinematic fitting.

5.2 Proton Identification

CLAS identifies charged particles through tracking and timing information. Through tracking, the particle's momentum is determined from the track curvature due to the magnetic field. The path length to the TOF counters is also determined through tracking. With the timing and path length in hand, the particle's velocity can be calculated. The mass of the charged particle is calculated as $m = \frac{p}{\beta\gamma c}$. The β versus p distribution for a set of selected protons is shown in Figure 5.1. From the plot, a band of background events is seen at low momentum. This is caused by choosing the wrong beam photon with out of time information.

5.3 Data Filtering

The reaction analyzed was $\gamma p \rightarrow pp\bar{p}$. Initially, these events were selected from the g6c data set by requiring two protons and one antiproton to be detected, with no other detected particles. To improve data yield, requirements were relaxed so that the antiproton could be missed and its four-momentum obtained through energy/momentum conservation. The final data set, after all cuts, contained 18,419 events. Using this selection, the data yield increases by a factor of three over that with all particles detected. The increased yield is attributed to the fact that the antiproton's acceptance suffers greatly because of the inbending due to the torus field which result in a higher probability that antiprotons end up deflected back into the beam line.

Because of charge and baryon number conservation, events with two protons in the final state at these energies require an antiproton. As a result, the background caused by other reactions is small. The reactions $\gamma p \rightarrow pp\bar{n}\pi^-$ and $\gamma p \rightarrow pp\bar{p}\pi^0$ require a missing mass much larger than the antiproton. These cannot contribute to the background near missing mass of the antiproton. The reaction $\gamma p \rightarrow pp\bar{p}\gamma$ would have a missing mass beginning near the antiproton missing mass. It would be expected that this type of background would cause an enhancement at masses larger than the antiproton. The missing mass squared distribution does not exhibit this feature, thus it is does not significantly contribute to the background. It was found that the performance of the Electromagnetic Calorimeter was poor. Most neutral calorimeter hits were attributed to out of time neutrons which can masquerade as photons. Given a very small background caused by other reactions which may involve neutral particles, and a small signal to background ratio in neutral particle detection, it was safe to assume that neutral particles detected in events could be ignored. Thus events with identified neutral particles, in addition to the two protons, were not excluded from the filtering. Therefore, the filtering required two protons, an optional antiproton, and no other charged tracks. Neutral particles were ignored altogether.

It was also possible to obtain events by allowing one of the protons to be missed. However, this data set contained less than three thousand events, compared to seventeen thousand events using the same cuts for events with two protons. This was expected due to the much higher acceptance rate for positively charged particles versus negatively charged particles. The proton acceptance in this experiment was estimated to be approximately 50%, whereas the acceptance for the antiproton was roughly 28%. The difference in the acceptance of protons and antiprotons is a result of the antiprotons being bent towards the beam due to the magnetic field. The antiprotons have a much larger chance of going undetected due to passing through less of the CLAS detector. Given the large discrepancy in acceptance and the small added yield by missing a proton compared to the missing antiproton yield, the missing proton data was excluded from further analysis.

5.4 Momentum and Energy Corrections

Charged particles lose energy as they traverse the target material. This effect was corrected for the final proton momentum by determining the amount of energy lost due to the various media the particles traverse before entering the drift chambers [44]. These corrections were applied to all protons before energy/momentum calculations. Momentum corrections were applied to the charged particles to reduce systematic errors caused by the limited capability of the tracking algorithms[45]. For protons, the correction was determined by studying the reaction $\gamma p \rightarrow p(\omega)$. The ω particle was observed through missing mass, and the proton momentum was corrected such that the mass of the ω was at its nominal value. These corrections had very little effect on the proton momentum, as the corrections resulted in a less than $0.1 MeV/c$ momentum change. From the g6c data, it was found that the beam energy was not measured correctly. This was corrected by increasing the measured energy of tagged photons by 0.2%.

5.5 Data Selection Cuts

After filtering events by particle identification, initial cuts were applied to the data set. These selections include beam energy, vertex position, and timing requirements. As described previously, the photon energy was determined using a photon tagger. While the trigger required that a photon with an energy in the range of 4.8 to 5.5 GeV be identified in the tagger, additional low energy beam photons were also tagged during the 10ns time window surrounding the triggered photon. This led to an ambiguity in which beam photon is associated with the production of the event measured in CLAS. Timing requirements must be used to take into account this ambiguity, as well as energy conservation cuts. Figure 5.2 shows the beam energy distribution for all events where two protons have been identified. The peak starting at 4.8 GeV occurs because of triggering requirements of a tagged photon with at least 4.8 GeV of energy. The events below 4.8 GeV are those in which more than one photon was tagged in the 10ns time window. For this analysis, each event was required to have a beam energy in the range of 4.8 to 5.5 GeV. Events below this energy were excluded from further analysis.

After making the beam energy cut, there could still be multiple photon beam candidates. Making use of the event timing in CLAS, and the electron beam timing from the accelerator, the correct photon was identified by requiring that the time of the beam at the reaction vertex coincided with the CLAS event time at the vertex.

The intersection of the beam and charged particle tracks was used to determine the position of the event vertex. However some events may have occurred outside of the liquid hydrogen target, such as in the target container's walls as seen in Figure 5.3. The peaks at -110, -92cm are caused by the entrance and exit windows of the target container, and the peak at -87cm was caused by the end-snout of the vacuum

Table 5.1. Initial Cuts on Two Proton Data. Each entry shows the number of events in the sample after the given data selection requirement was made. The total $p\bar{p}$ events were the number of events that passed the event filter.

Data Set Description	Events
Total two proton events	5405333
After beam energy cut	2755674
After timing cut	880226
After vertex cut	459703

beam line. Events were required to have an event vertex inside the target region. Table 5.1 summarizes the effects of the initial data cuts and the effective yields.

Using energy/momentum conservation, the missing four-momentum was calculated using the four momenta of the beam, the target, and the two detected protons. Figure 5.4 shows the missing-mass-squared(the magnitude squared of the missing four-momentum) of events containing two identified protons. The distribution was fit to a Gaussian plus a linear background. The result of the fit finds the prominent peak at $0.8769 \pm 0.0002 (GeV/c^2)^2$, which was consistent with a missing antiproton. The Gaussian width was $0.0177 \pm 0.0002 (GeV/c^2)^2$ which corresponds to a missing mass resolution of $9.45 \pm 0.11 MeV/c^2$. Selecting the events consistent with a missing antiproton ($0.85 (GeV/c^2)^2 \leq MM^2 \leq 0.91 (GeV/c^2)^2$) yields approximately 17,100 $\gamma p \rightarrow pp(\bar{p})$ events. Not all of these events were $\gamma p \rightarrow pp\bar{p}$ events as seen by the nearly linear background of non-antiprotons in the missing-mass squared distribution. A linear background fit results in a background of approximately 9.6% in the selected missing mass squared region. This background will be discussed further in the Kinematic Fit section.

Detecting two protons at these energies likely necessitates the existence of an antiproton in the event. This is simply a result of baryon number and charge conservation. It's also possible that both a π^- and a $\bar{n}$ were missed, or perhaps a $\bar{\Delta}^-$, but if these background sources were significant, these events would be evident in the missing mass spectrum. Therefore, the background events are likely dominated by particle misidentification, by choosing the wrong beam photon, or events containing additional missed final state photons. Particle misidentification occurs when a pion or a kaon was incorrectly determined to be a proton by the particle identification program. Studies show that this effect is near negligible. Due to timing resolution it is possible to select the wrong beam photon. This systematic effect will be estimated in a later section. Unfortunately, attempts to further understand the background due to missing final state photons are inconclusive. This is due to poor performance of the CLAS electromagnetic calorimeter.

5.6 Fiducial Cuts

Events in which particles pass through the edges of detectors should be excluded, because it is often difficult to fully reproduce the detector acceptance in these regions via Monte Carlo simulations. Also, a small error in measuring acceptance becomes greatly magnified in regions of low acceptance. It is not possible to simply remove hits on individual detector elements near detector edges. Tracks are measured using hits on multiple adjacent elements, thus removing elements near edges will simply create new edges with the same inherent problems. The fiducial cuts defined in this section make angular selections by defining an acceptable geometric area for charged particle tracks to pass through.

The main regions excluded were those occupied by the coils of the torus magnet between the six sectors and the beam pipe. In order to define these cuts, Monte Carlo events were used to measure the protons' angular acceptance. Five million events were simulated using a meson exchange production mechanism. Some proton tracks were not reconstructed by the reconstruction program. These events were not accepted, and the ratio of accepted events to the total number of generated events per bin gives the acceptance as shown in figure 5.5. The figure shows the effects of the separation of the six sectors due to the torus coils. Also, the poor acceptance due to protons being lost in the beam line at low θ_{lab} is seen.

The excluded region was where the acceptance drops sharply from around sixty percent to ten percent. To cut these regions, boundaries around the acceptable regions were defined. This was done by defining a function which best describes the boundary shape.

The boundaries around the acceptable regions were roughly parabolic, but the flat regions near $\theta = 0.09$ coupled to the nearly vertical regions at greater θ made it difficult for a parabolic function to fit. It was found that a fourth order polynomial was well suited to fit the boundary region. The fourth power term fits the nearly vertical regions relatively well, while the second order term describes a nearly flat boundary at low θ. Excluding the first and third order terms, the polynomial was kept symmetric. The zeroth order term simply defines the angle θ at which the acceptable region begins. The fiducial boundary function was then $A\theta^4 + B\theta^2 + C$. After matching to the boundary regions, the fiducial boundary function for the first sector at $\phi = 0$ was determined to be

$$\phi = 10\theta^4 + 0.25\theta^2 + 0.09.$$

The boundary functions for the other sectors are found by simply shifting the polynomial by multiples of $\pi/3$ in ϕ. Figure 5.6 shows the fiducial cut for one sector, and figure 5.7 shows the fiducial cuts for all sectors. Figure 5.8 shows the data prior to the fiducial cut and figure 5.9 shows the result of the fiducial cuts on the data.

5.7 Kinematic Fit

Kinematic fitting is a mathematical process that uses physical constraints to make corrections to measurements. Energy and momentum conservation are used to constrain the measured particle four-vectors. A least squares fit is performed using Lagrange multipliers to handle the constraints and a covariance matrix to be used for corrections [50]. Performing the fit yields a confidence level distribution which is used to measure the goodness-of-fit of the data to the hypothesized reaction. The fit also yields pull distributions which measure how much individual variables had to be varied over the entire data sample. The pull of a variable being fit is defined as $z \equiv \frac{\epsilon}{\sigma(\epsilon)}$, where ϵ is the error of the variable with a standard deviation $\sigma\epsilon$. The pulls are used to measure the quality of the error estimations.

The kinematic fit was performed using the CLASevent package developed by M. Williams and C. A. Meyer [50]. The events being fit passed the data selection cuts and the fiducial cuts. The missing mass squared cut was loosened to the range $(0.7 - 1.1(GeV/c)^2)$. Before fitting, the events were corrected using energy loss and the charge particle momentum corrections. From the kinematic fit, each event is given a confidence level, which measures the statistical significance of the event fitting the hypothesized reaction. With no background, the confidence level follows a flat distribution from 0 to 1. Events which do not fit the hypothesized reaction produce a sharp rise in the confidence level near zero.

Figure 5.10 shows the confidence level distribution for the fit. The distribution has a large peak at low confidence and then quickly becomes constant at higher confidence. Typically, this distribution can be used to cut out background events by removing the events with less than one percent confidence level. In the range of up to five percent confidence level there are still a large number of events above the constant confidence level. The majority of these events do not meet the hypothesized reaction and thus are also thrown out. In the inset diagram at the top-right of figure 5.10, the red area indicates where the events with low confidence level lie in the missing-mass-squared distribution. Note that it drops to zero around the mass of the antiproton. This is expected, as it is still possible for some background events to meet the constraints defined by the hypothesized reaction. The inset at the bottom-right shows the missing-mass-squared distribution after the five percent confidence level cut.

To estimate the background and the events lost due to the confidence level cut, the missing mass squared distribution was fit to a Gaussian plus a linear background. This is shown in Figure 5.11. For a missing mass squared cut of 0.85 to 0.91 $(GeV/c^2)^2$, the background is estimated to be 9.6%. The events which did not pass the 5% confidence level cut are shown against all the events in Figure 5.12. The black curve is the linear background fit. In the sideband regions, some good events were cut. To estimate the number of good events lost in the side bands, the number of events above the linear background were counted. The number of good events which were cut by the confidence level represent 6.4% of the total number of good events. In the central region, bad events pass the cut because they are so close to the antiproton mass. The accepted background events represent approximately 6.6% of the yield.

An analysis was done to check that the ionization energy loss and momentum corrections improved data quality. To evaluate the quality of the error estimation used by the kinematic fit, one studies the pull distributions. A pull for an event is the amount a kinematic variable was shifted in order to fit the event to the hypothesis. The pull distribution is expected to have a mean value of zero and a standard deviation of one. The data was first fit without either correction, then with just the energy loss correction, next with only the momentum corrections, and then with both corrections. For each kinematic fit, the pull distributions were studied to evaluate the effects of the energy and momentum corrections.

Table 5.2 shows the mean of each of the pull distributions for the four cases. The variable E is the beam photon energy. P_i is the total momentum of proton i. ϕ_i is a drift chamber angle similar to polar angle *theta* in the lab, where the z-axis is along the beam. λ_i is a drift chamber angle similar to the azimuthal angle in the lab. For full detail, see reference [50]. From the table it appears that the effects from the energy loss corrections are small for this data set, because they do not greatly affect

Table 5.2. The mean values of each of the pull distributions for the four cases run through the kinematic fitter. The last column shows the standard deviation for the case in which both corrections were made. Comparing the pulls for no corrections to those of the momentum corrections, it is seen that momentum corrections generally reduce the pulls. The energy loss corrections however, do not appear to significantly affect the pulls. After the corrections are made, the pulls are consistent with a good error estimation by the kinematic fit.

Mean Pull Values					
Pulls	None	Energy Loss	Momentum	Both	$\sigma(both)$
E	0.5640	0.4959	0.3017	0.2257	1.147
P_1	-0.3269	-0.3615	-0.1755	-0.2404	1.045
λ_1	-0.1798	-0.1422	-0.0902	-0.0933	1.098
ϕ_1	-0.2982	-0.2710	-0.1840	-0.1417	1.101
P_2	-0.1587	-0.2638	-0.0300	-0.2404	1.061
λ_2	-0.2972	-0.0674	0.0000	-0.0416	1.112
ϕ_2	-0.0356	-0.0715	0.0153	-0.0237	1.080

the pulls. The momentum corrections are more effective in moving the pulls closer to zero.

If the kinematic fit has good error estimations, the pulls should have means of zero and standard deviations of one. Each of the pulls are fit to Gaussian distributions after making a one percent confidence level cut. The confidence level cut is done so that the error estimation is not affected by events which do not fit the reaction hypothesis. For the case of using both the energy and momentum corrections, the Gaussian fits are shown in figure 5.13. The last column of table 5.2 shows the standard deviation values. The standard deviations are consistent with good error estimation by the kinematic fit.

After performing the kinematic fit, the measurements of the protons' momenta were improved. Figures 5.14 and 5.15 show the change in momentum for the protons and the antiproton. The protons have negligible momentum shifts, and the antiproton has a relatively small energy shift on the order of a tenth of a percent. The angular distributions of a particle in a two-body rest frame rely heavily on the boosts used to get to that rest frame. Small changes in the particle four-momentum vectors can drastically change these distributions because boosts have the ability to magnify these slight corrections. In figure 5.16 the angular distributions of the antiproton momentum in the $p_{slow}\bar{p}$ rest frames, which will be defined in Chapter 6, are shown. The blue lines indicate the distributions before the kinematic fit and the red lines show the distribution after the fit. The distributions do not show any significant changes due to the kinematic fit.

For the final data set, a five percent confidence level cut was used. The red line histogram in figure 5.17 shows the $p_{fast}\bar{p}$ invariant mass distribution. The blue line shows the distribution before the fit using a missing-mass-squared cut instead. Considering the kinematic fit distribution has more events, the two distributions are statistically equivalent otherwise . Figure 5.18 shows the same for the $p_{slow}\bar{p}$ system. The overall shape does not change significantly due to the kinematic fitting.

5.8 Remarks on the Data Selection

The data selection resulted in a total yield of 18,419 events. To date, this event sample represents the largest set of events in which a proton-antiproton pair was produced. The kinematic fit slightly improved the protons' four-momentum vectors and justified the use of the momentum and energy corrections. Additionally, the kinematic fit allowed more good events to be accepted without increasing the background percentage. The background was estimated to be 6.6% of the data sample.

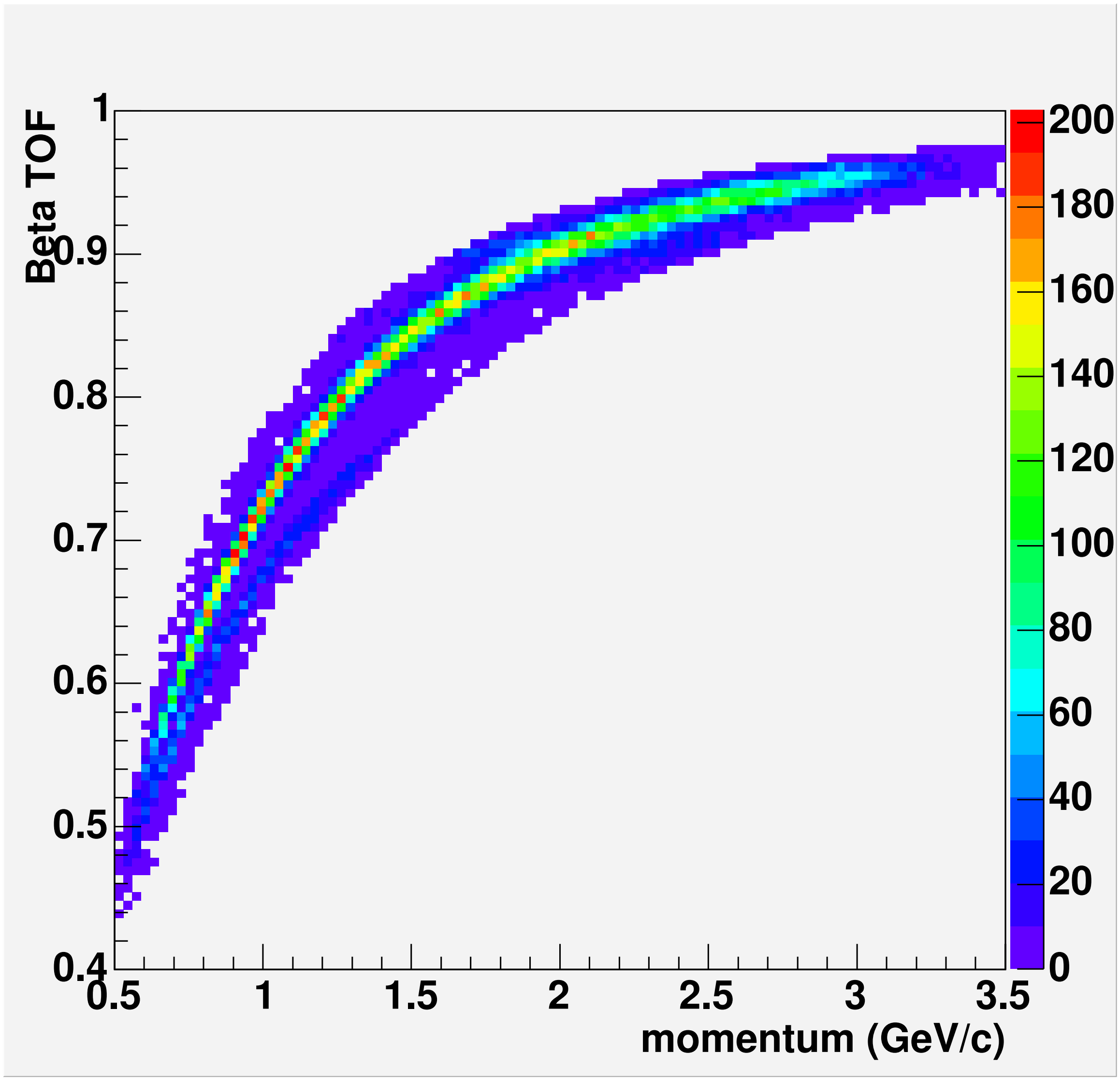

Figure 5.1. The velocity of particles identified as protons compared to their momentum. A background band is seen at low beta. This is caused by choosing the wrong beam photon with out of time information.

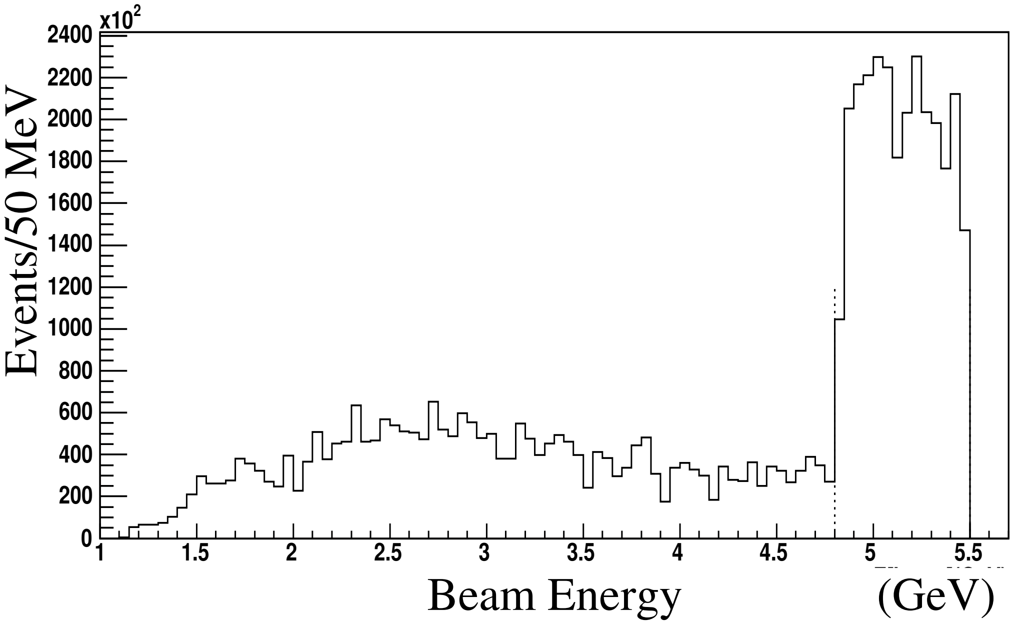

Figure 5.2. Beam Energy Distribution for $\gamma p \rightarrow pp(X)$ events. The yield at high energy coincides with the experimental trigger requirements. The low energy photons are acquired because multiple photons may be tagged. This allows for low energy photons with proper timing requirements to be chosen over the high energy tagged photon.

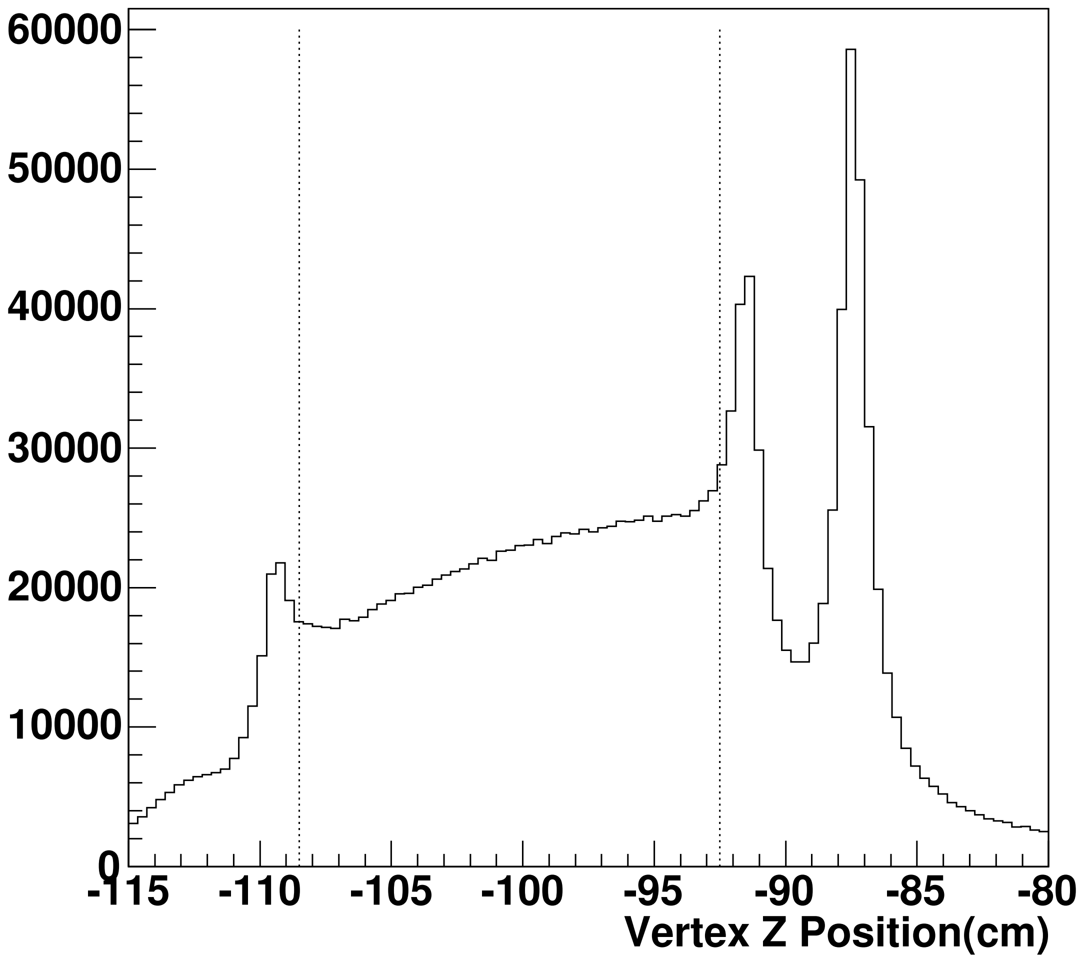

Figure 5.3. The vertex z-position for events after energy and timing cuts. The peaks correspond to the position of parts of the target container. The vertical dotted lines indicate where the cuts were made. These cuts were made at -108.5 and -92.5 cm. to remove the majority of events which occurred outside the target.

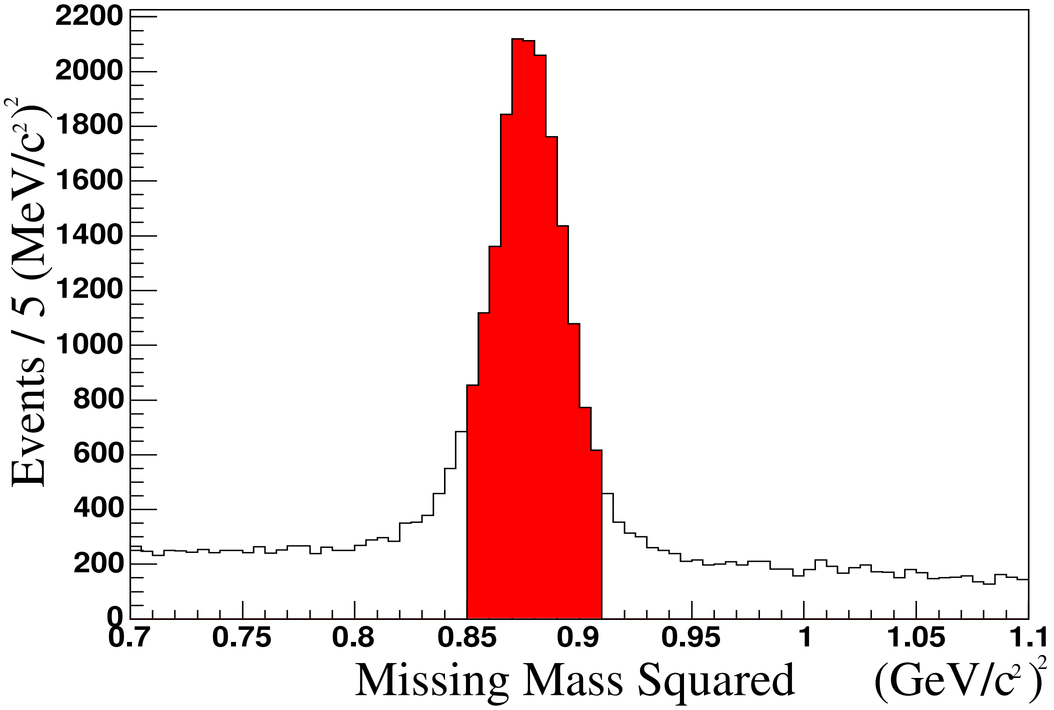

Figure 5.4. Missing Mass Squared for $\gamma p \rightarrow pp(X)$. The mean of the peak is fit to $0.877(GeV/c^2)^2$. The width corresponds to a missing mass resolution of $9.4MeV/c^2$. The background after the missing mass cut is approximately 9.6%.

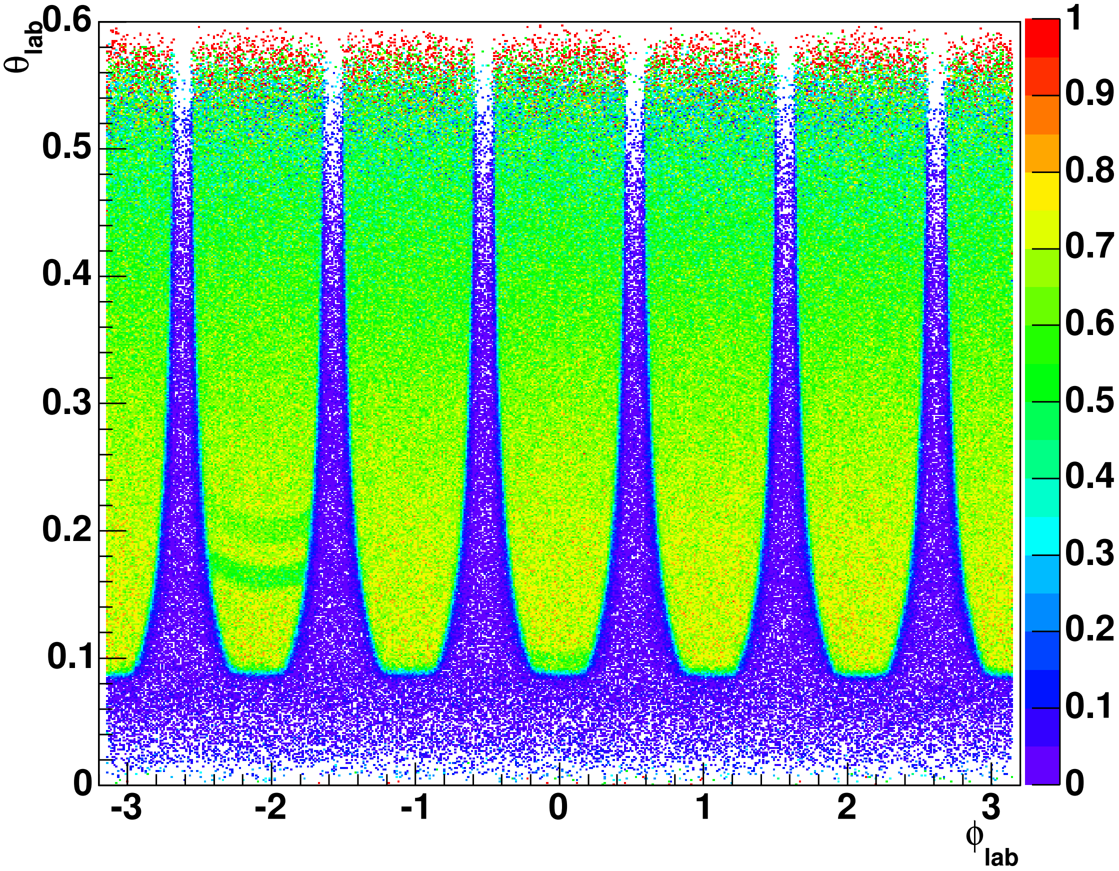

Figure 5.5. Five million Monte Carlo events were generated to measure the angular acceptance. The multiple green areas represent the six DC sectors. The separation between sectors are the spaces occupied by the torus. The tips of the six sectors at low θ_{lab} are the extreme forward regions of CLAS. At larger angles the number of events decreases as seen at higher θ_{lab} values. The low acceptance area at low θ is where the beam passes through the detector. The two bands seen in the sector near $\phi = \frac{-2\pi}{3}$ are caused by inefficient or poorly calibrated TOF paddles.

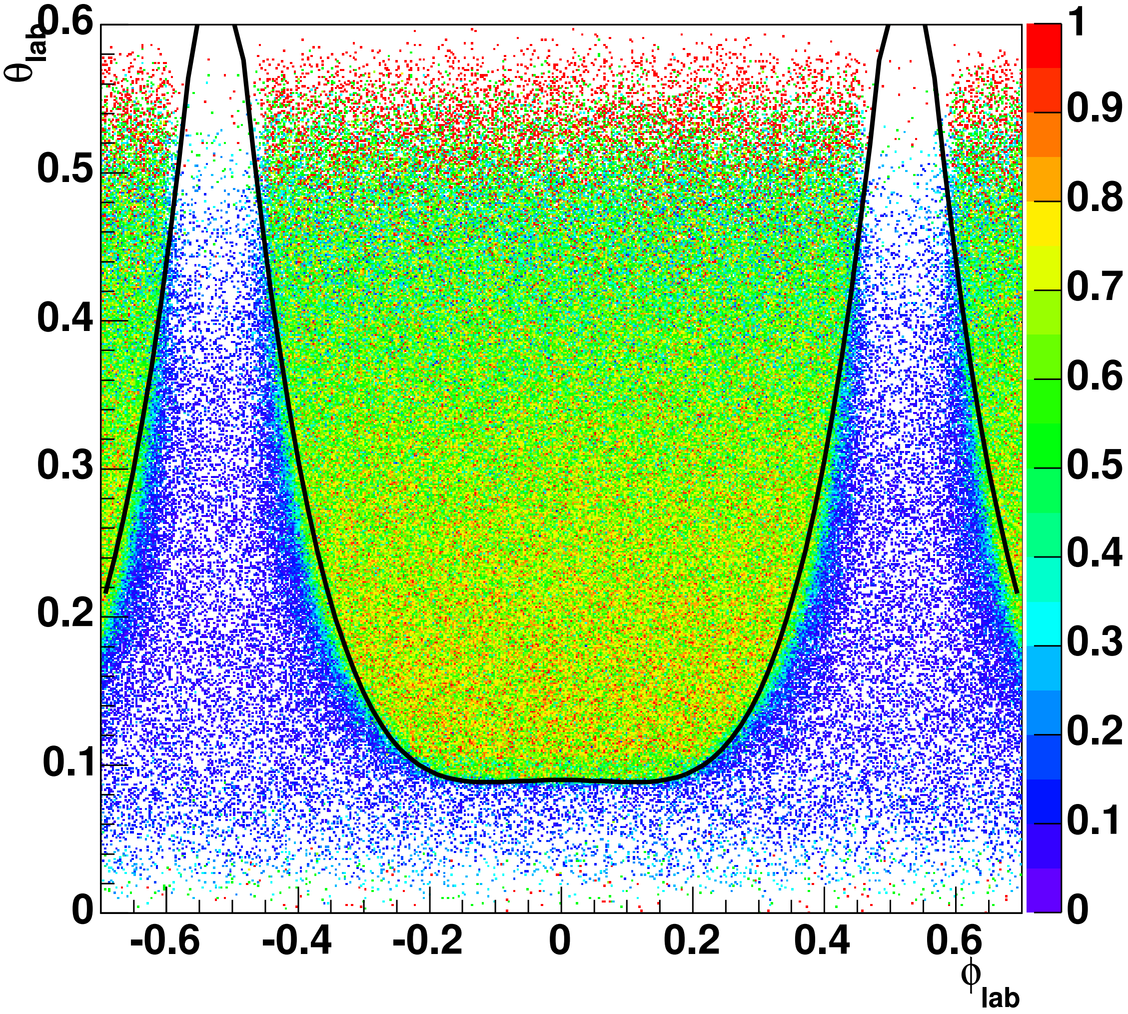

Figure 5.6. A closeup of one sector's angular acceptance. The curve represents the fiducial cut used. The drop in acceptance around the boundary is generally caused by hits in elements of the detector that occur near its edges. Often hits are reconstructed using signals in multiple detector elements. By hitting near an edge, fewer detector elements may be used for reconstruction.

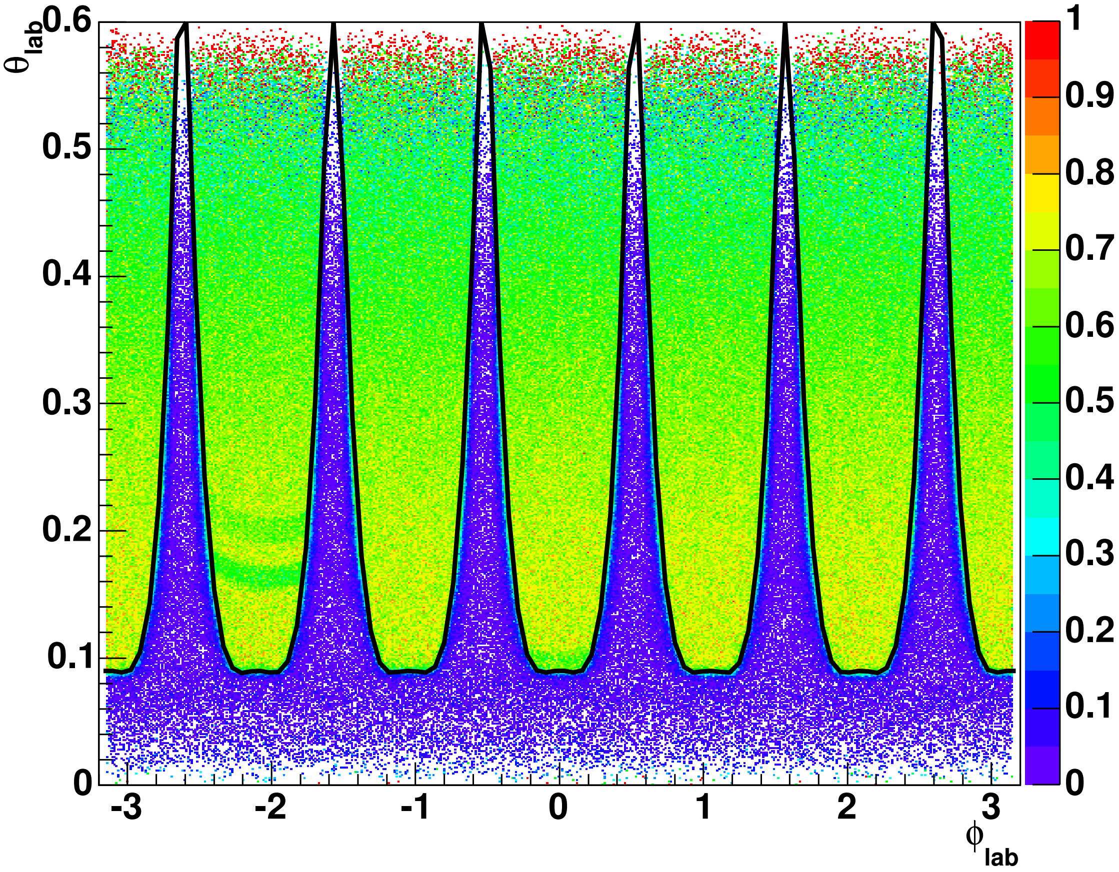

Figure 5.7. The fiducial cut for all sectors is shown as the black curves on top of the angular acceptance. The curves are fourth order polynomials fit to the boundary regions. Each is defined using the same shape, but shifted in ϕ by $\pi/3$.

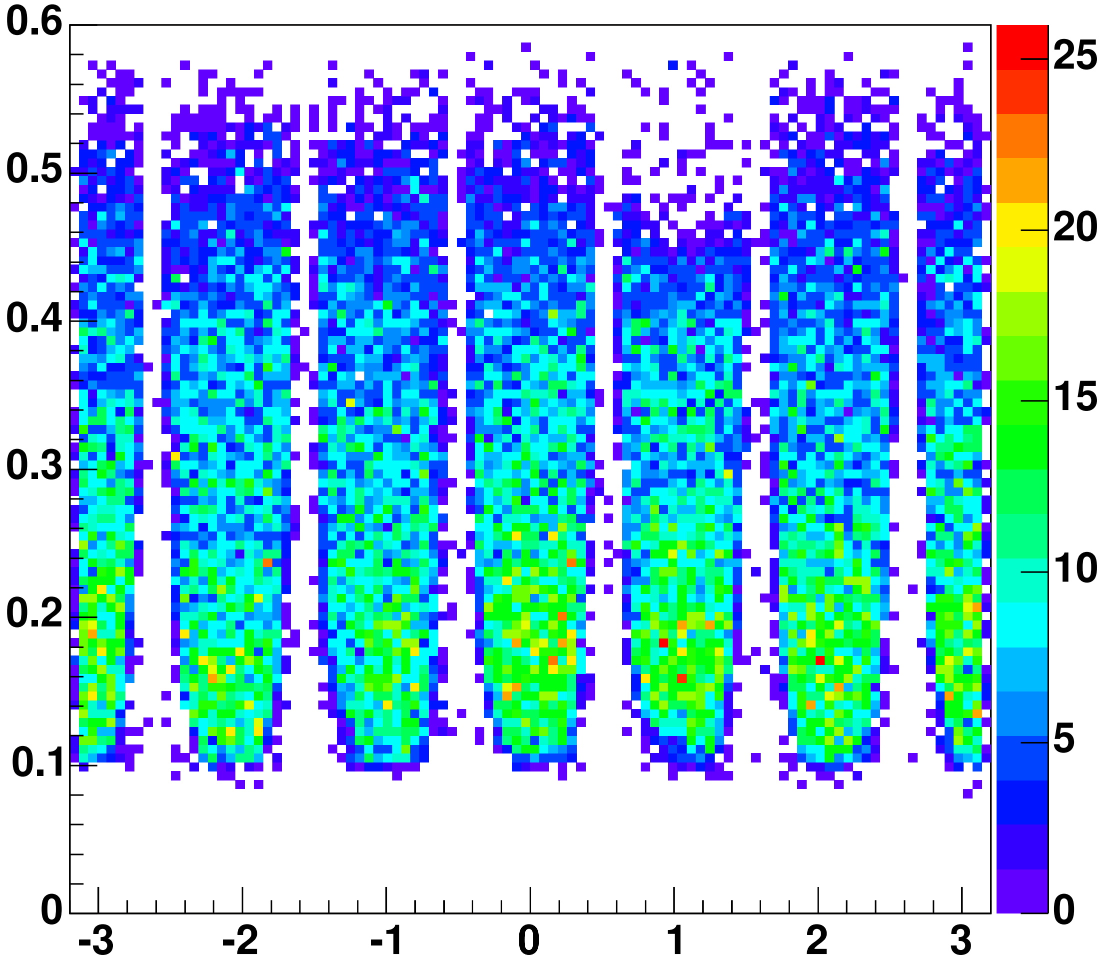

Figure 5.8. The initial proton momentum angular distribution. Note the events that are accepted despite being outside the normal acceptable regions of CLAS. These events will be cut as shown in the following figure.

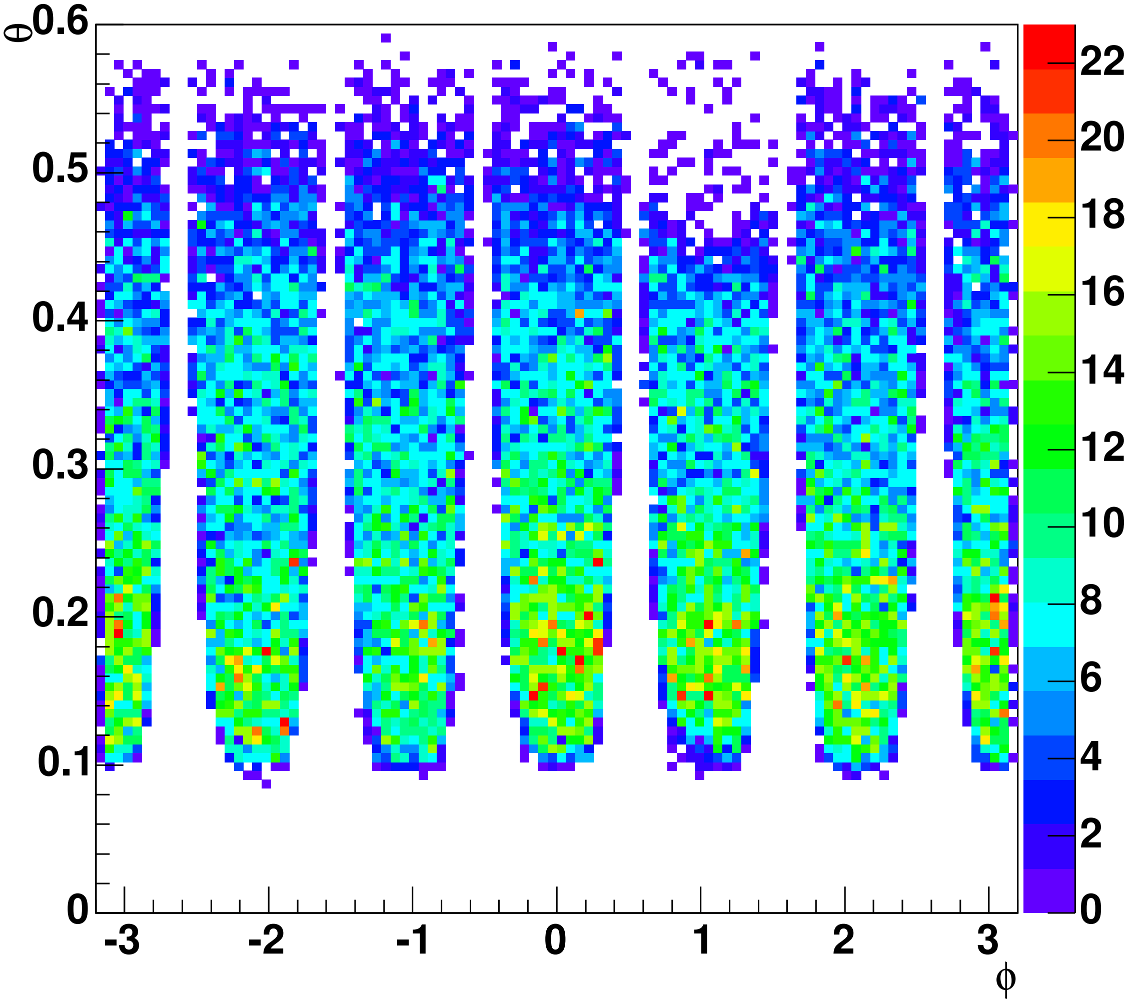

Figure 5.9. The resulting momentum angular distribution after the fiducial cuts are made. The fiducial cut is made before any corrections are applied to the data. This is done because corrections may change a proton's momentum so that it points in an unacceptable region, even though the event is valid.

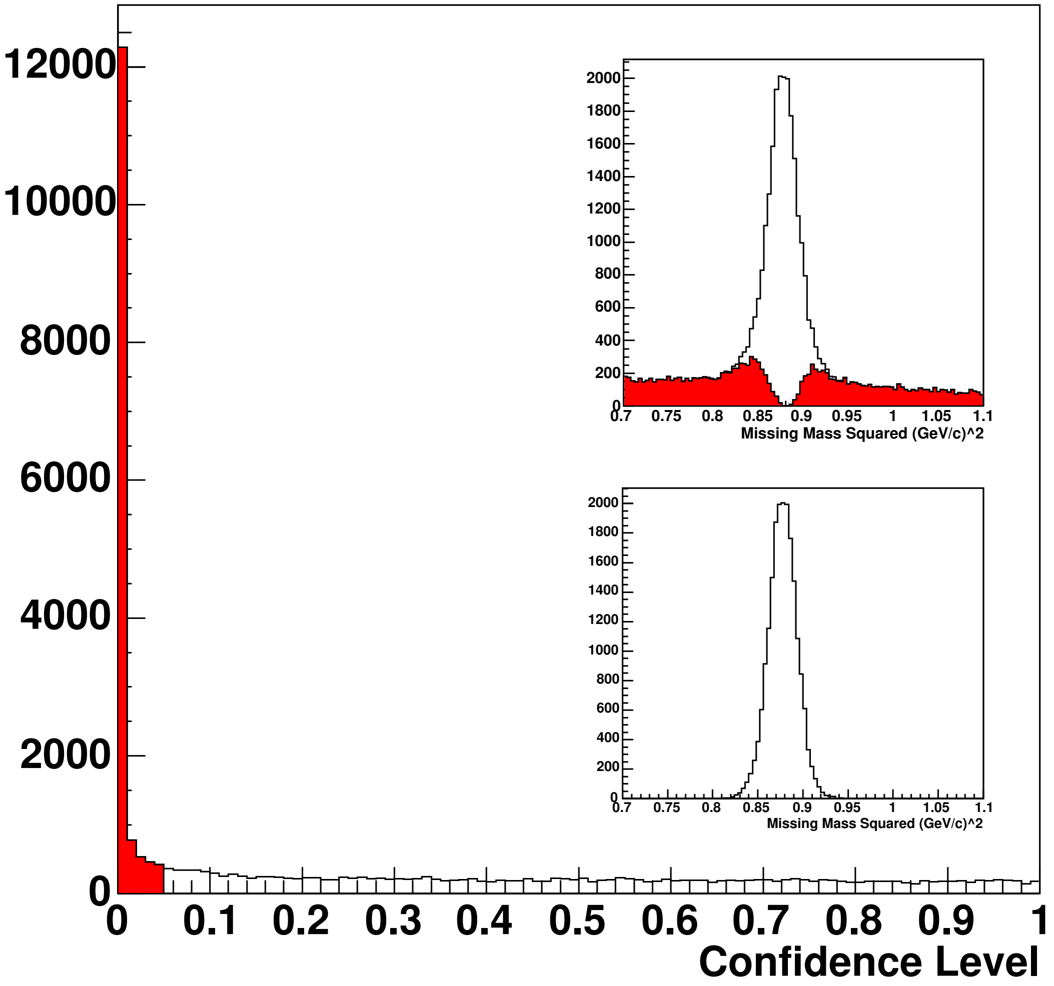

Figure 5.10. The confidence level distribution. The red areas indicate the events that are cut from future analysis. The top-right inset shows the missing-mass-squared distribution with the low confidence level events shown in red. The bottom-right inset shows the missing-mass-squared distribution after a confidence level cut is applied.

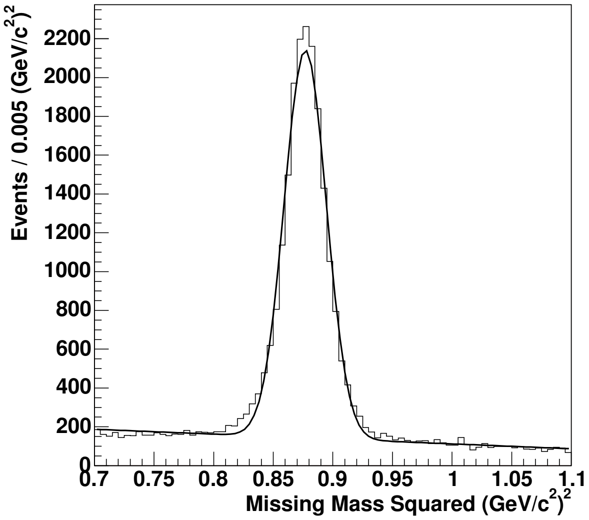

Figure 5.11. The missing mass squared fit to a Gaussian plus a linear background. The background estimate after a missing mass squared cut from 0.85 to 0.91 $(GeV/c^2)^2$ is 9.6%.

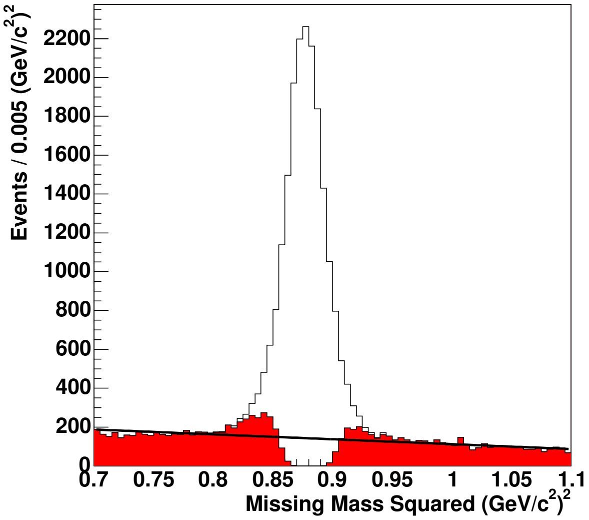

Figure 5.12. The missing mass squared distribution for events which did not pass the confidence level cut is shown in red. The black line represents the linear background fit. The sideband regions include good events which did not pass the cut, whereas the central region shows bad events which did pass the cut. The background is estimated to be 6.6% and the number of missed events represent 6.4% of the total.

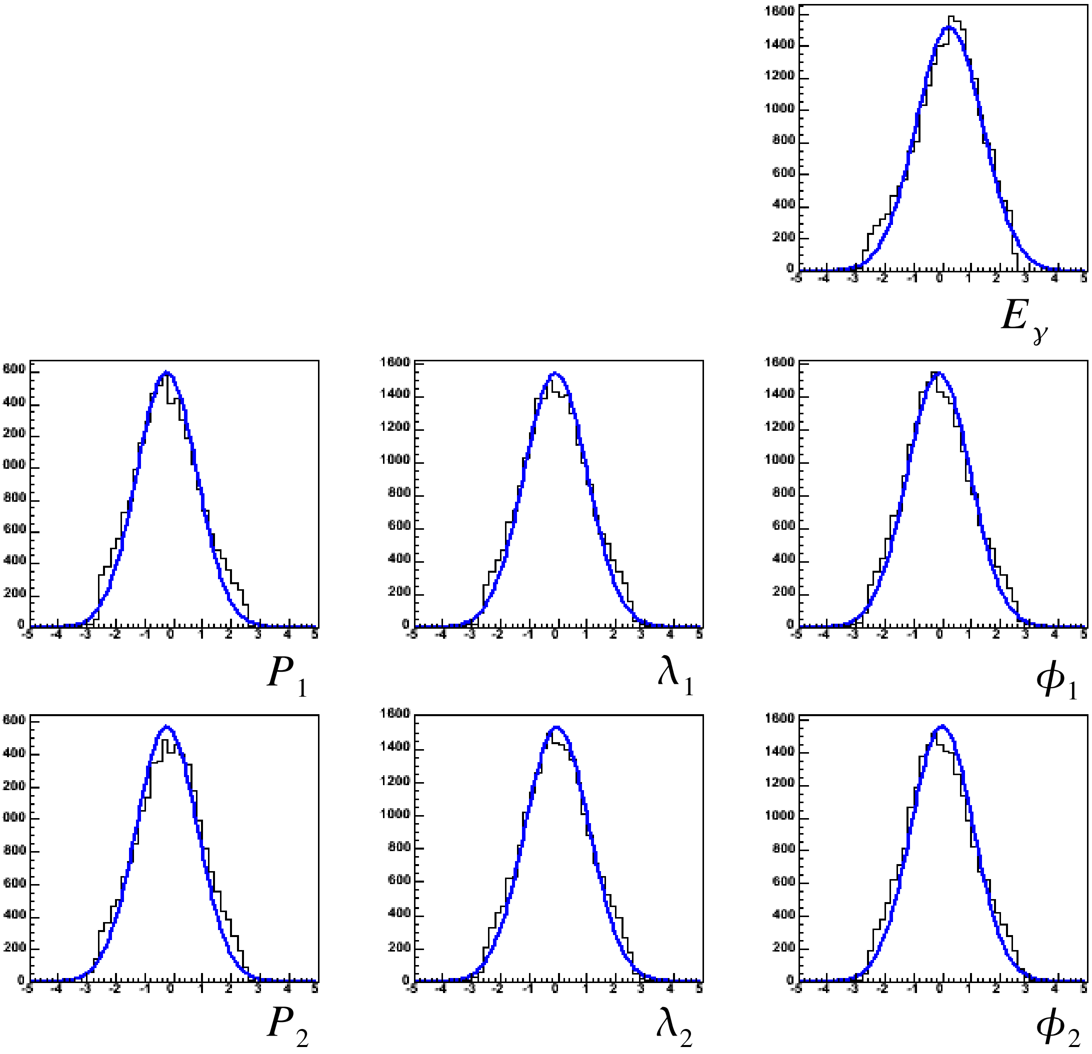

Figure 5.13. The pulls distributions with energy loss and momentum corrections, and a one percent confidence level cut. If the kinematic fit has good error estimations, the pulls should have means of zero and standard deviations of one.

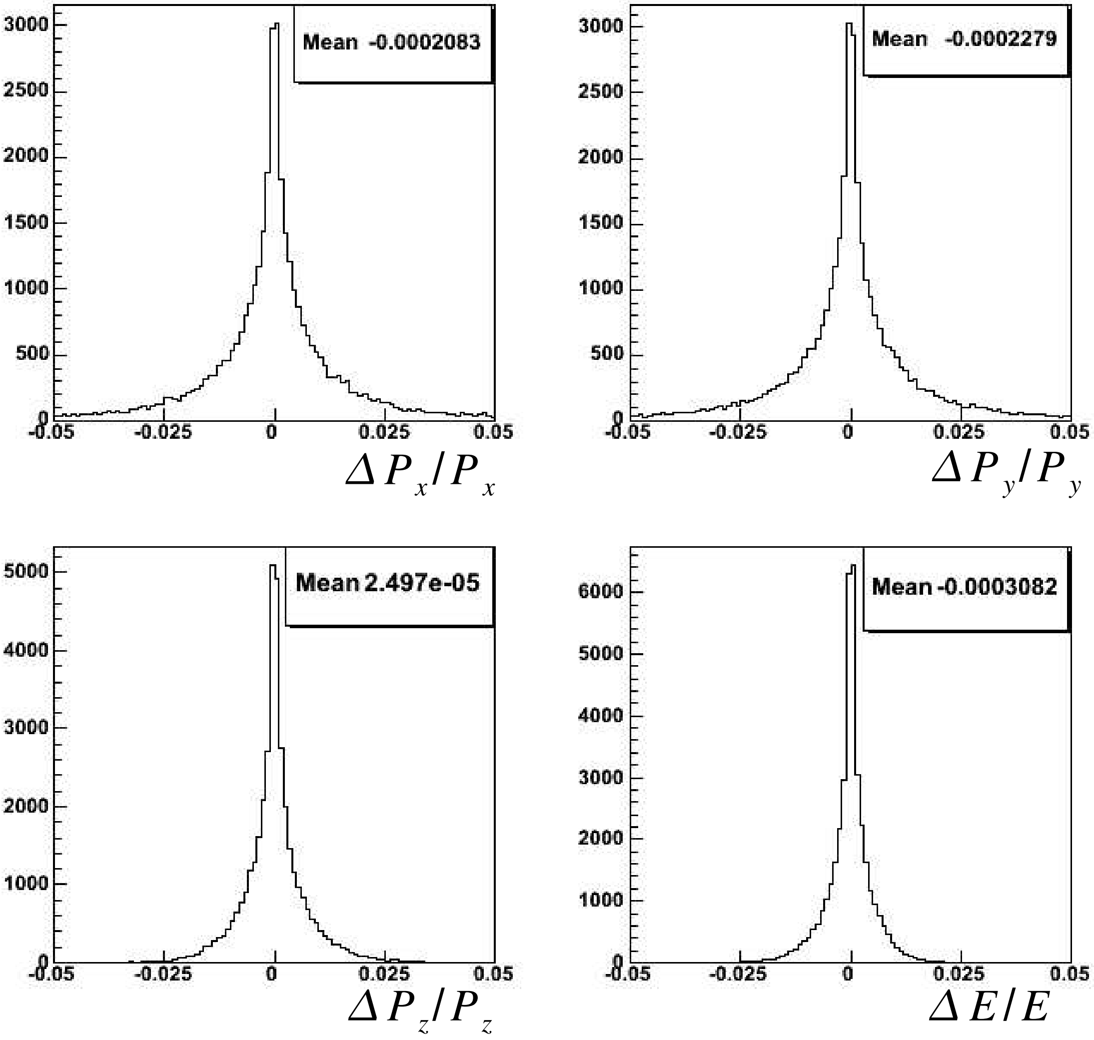

Figure 5.14. The change in momentum and energy for the protons due to the kinematic fit. No significant shifts are seen which would be evidence of systematic errors introduced by the fit.

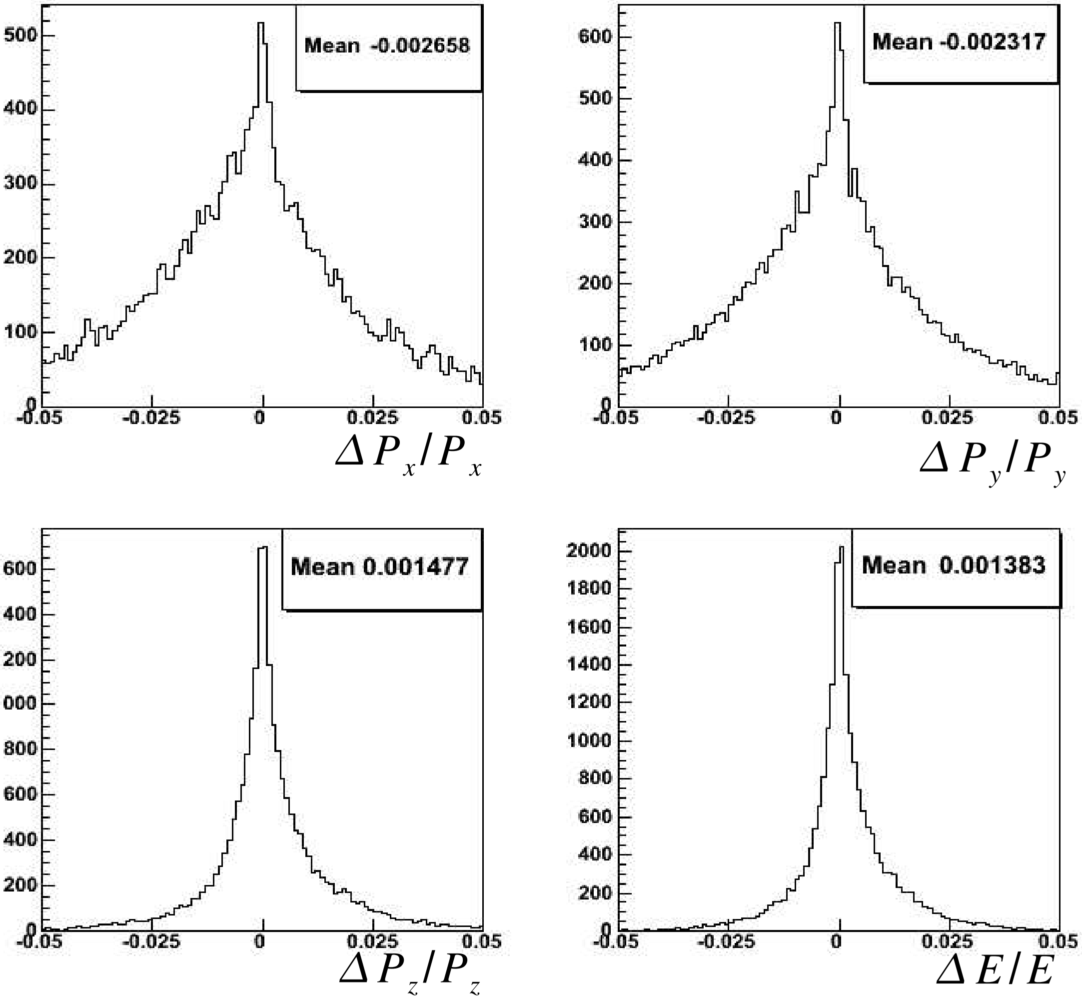

Figure 5.15. The change in momentum and energy for the antiprotons due to the kinematic fit. No significant shifts are seen which would be evidence of systematic errors introduced by the fit.

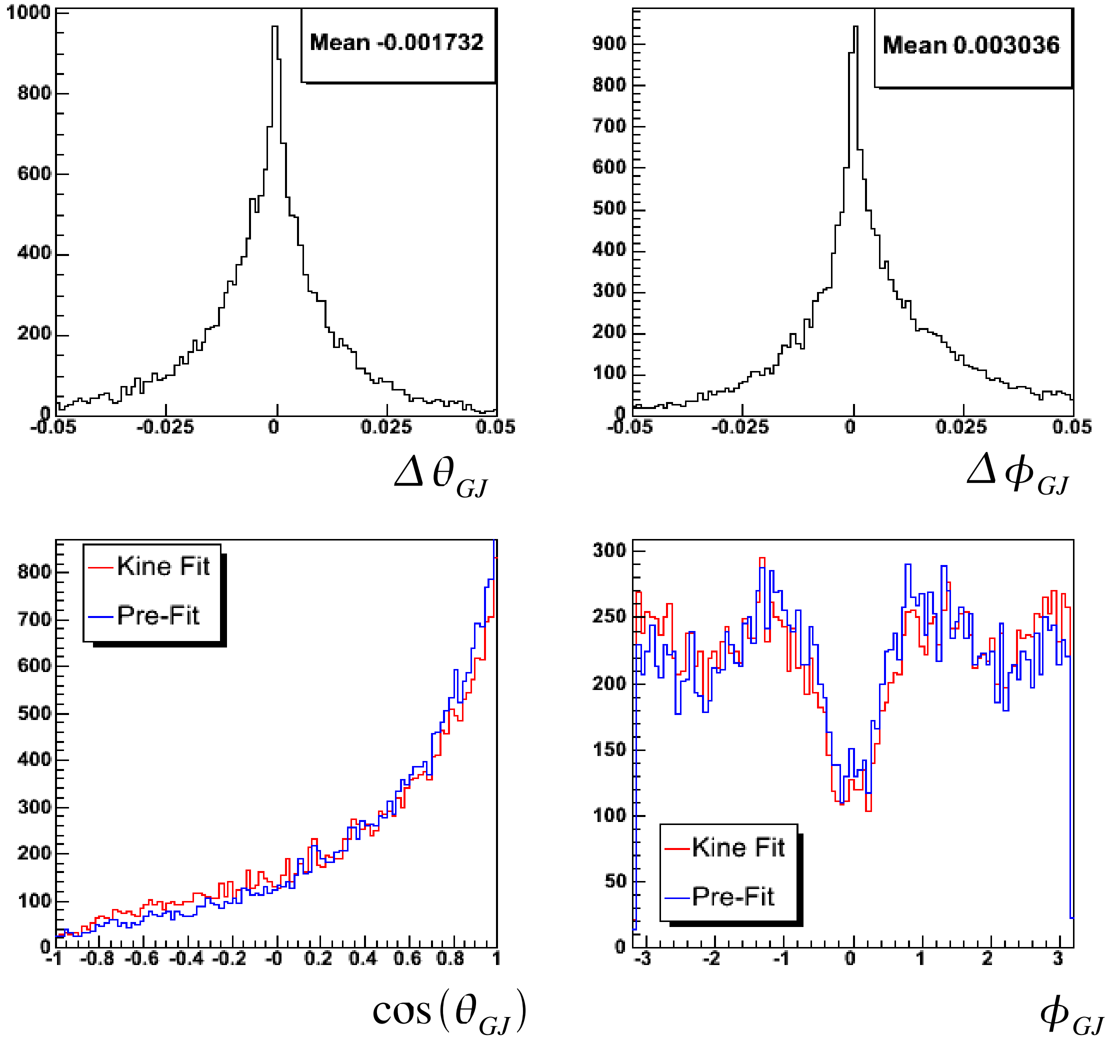

Figure 5.16. The change in the angular distributions for the antiproton in the $p_{slow}\bar{p}$ Gottfried-Jackson frame due to the kinematic fit. Small corrections in the lab frame angular distributions could have significant effects in this frame due to the boosts.

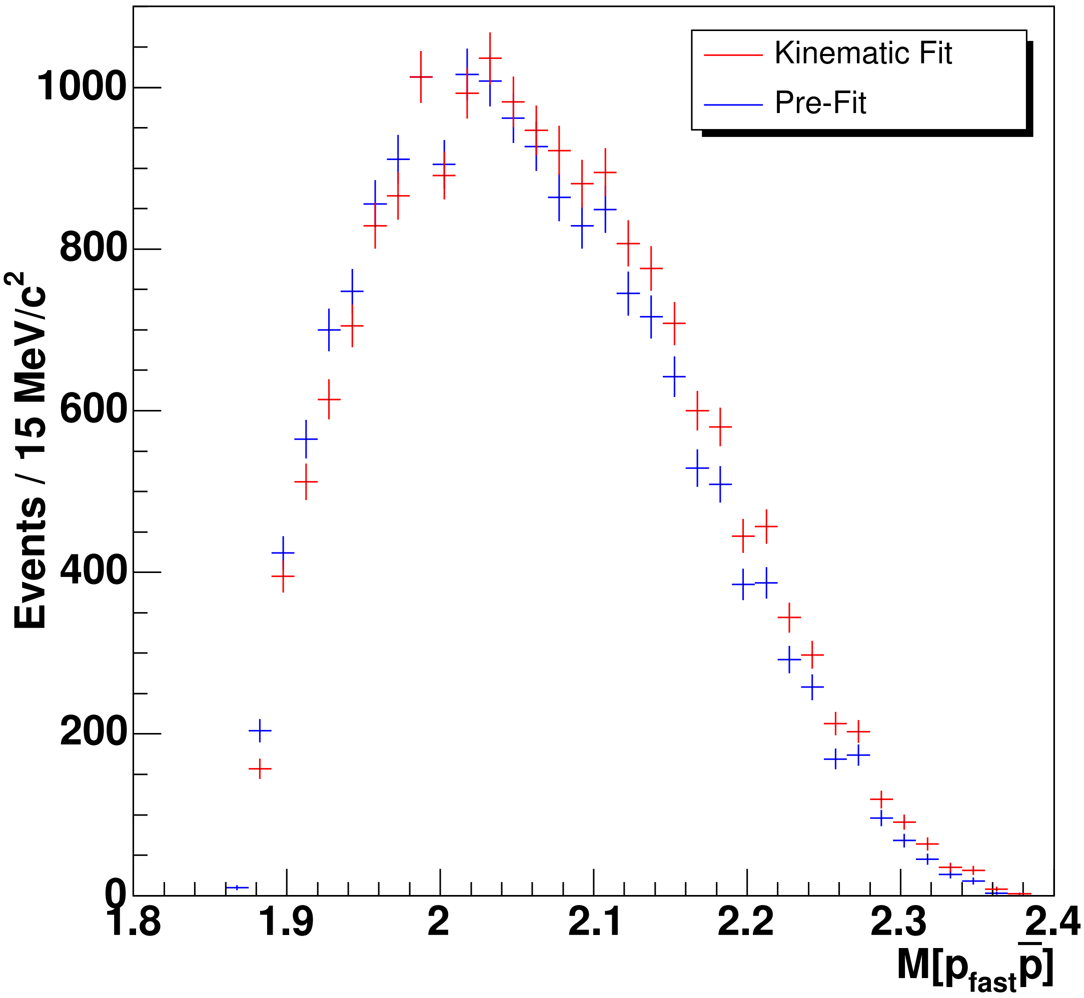

Figure 5.17. The $p_{fast}\bar{p}$ invariant mass distribution for the kinematic fit data with a 5.0 percent confidence level cut (red) and for the pre-fit data with a missing-mass-squared cut of 0.85-0.91 $(GeV/c)^2$ (blue). The kinematic fit does not introduce any significant change in the structure of the invariant mass distribution.

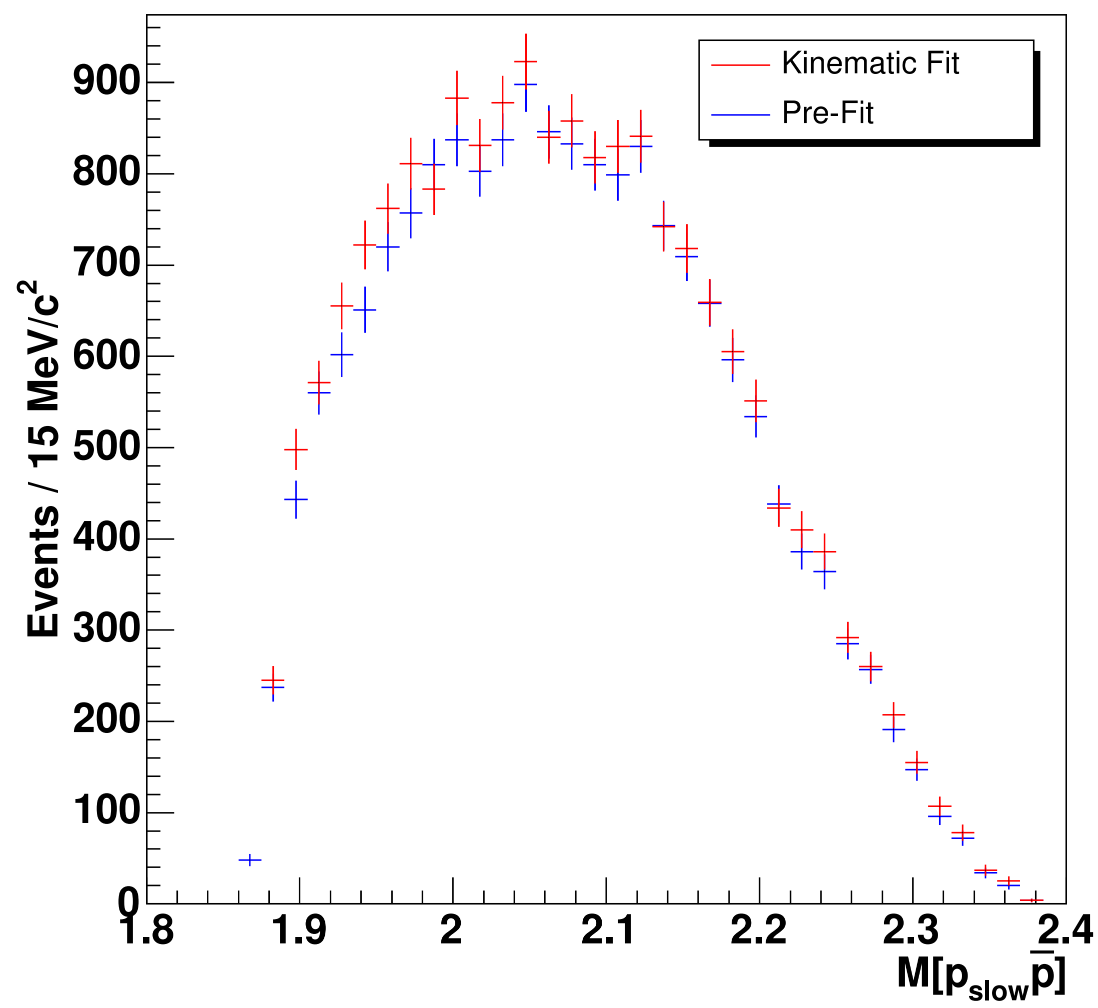

Figure 5.18. The $p_{slow}\bar{p}$ invariant mass distribution for the kinematic fit data with a 5.0 percent confidence level cut (red) and for the pre-fit data with a missing-mass-squared cut of 0.85-0.91 $(GeV/c)^2$ (blue). The kinematic fit does not introduce any significant change in the structure of the invariant mass distribution.

CHAPTER 6

GENERAL FEATURES OF THE DATA

The goal of this chapter is to describe the general features of the data. This chapter will mainly cover invariant mass distributions, angular distributions, and momentum exchange distributions. Some of the essential assumptions of the analysis will also be covered in detail.

6.1 Photon Energy

The beam energy distribution of the accepted $\gamma p \to pp\bar{p}$ events is shown in Figure 6.1. The histogram is binned so that each bin represents a single energy counter in the photon tagger. The structures were due to varying efficiencies of individual tagger elements. The photon energy range for this experiment lies well above the threshold for producing proton-antiproton pairs. The threshold photon energy for producing a $p\bar{p}$ pair is given by calculating the Mandelstam variable s, which is a Lorentz-invariant quantity. Conservation of energy and momentum requires

$$(p_1^\mu + p_2^\mu)^2 = s = (p_3^\mu + p_4^\mu + p_5^\mu)^2$$

where p_1^μ and p_2^μ are the initial state particle four-momentum vectors, and p_3^μ,p_4^μ,p_5^μ are those of the final state particles. Calculating s in the lab frame,

$$s = (p_\gamma^\mu + p_T^\mu)^2 = 2E_\gamma m_p + m_p^2$$

and then calculating s in the CM frame for three particles with mass m_p at rest,

$$s = (p_{p1}^\mu + p_{p2}^\mu + p_{p3}^\mu)^2 = 9m_p^2.$$

Therefore, at threshold

$$E_\gamma = \frac{9m_p^2 - m_p^2}{2m_p} = 4m_p = 3.753\ GeV.$$

6.2 Invariant Mass Distributions

The invariant mass distributions which follow were not corrected for acceptance. The two proton invariant mass is shown in Fig. 6.2. The distribution rises linearly from 1.9 GeV/c^2, peaking at 2.2 GeV/c^2. It then turns over and decreases linearly to 2.4 GeV/c^2. No obvious narrow peaks or features are observed. While a diproton resonance cannot be excluded, it is not expected. A particle decaying to two protons would require a state with at least six quarks. The antibaryon exchange process was excluded from most of this analysis.

The mass distribution of the proton-antiproton combination is shown in Figure 6.3. Since there are two protons in each event, there are two histogram entries per event. The distribution increases rapidly from 1.87 GeV/c^2 to around 2.0 GeV/c^2. From 2.10 GeV/c^2 it decreases almost linearly until 2.35 GeV/c^2. The intermediate mass region between 2.00 and 2.150 GeV is suggestive of structure, but one cannot clearly identify peaks or features of any intermediate states.

Figure 6.4 shows the overall proton momentum distribution. The two protons of each event can be labeled as a high momentum proton(fast) or a low momentum proton(slow). That is, in each event, the faster of the two protons is identified as p_{fast} and by default, the remaining proton is called p_{slow}. Using this differentiation in the protons, the $p_{fast}\bar{p}$ and $p_{slow}\bar{p}$ invariant mass distributions are shown in Figure 6.5 and Figure 6.6 respectively.

The $p_{fast}\bar{p}$ distribution increases rapidly from 1.87 GeV/c^2 to 1.92 GeV/c^2. It then rises more gradually until a maximum near 2.0 GeV/c^2. Just after 2 GeV/c^2 the distribution turns over and decreases steadily to 2.35 GeV/c^2. The $p_{slow}\bar{p}$ distribution increases rapidly from 1.87 GeV/c^2 until 1.95 GeV/c^2. The distribution reaches a

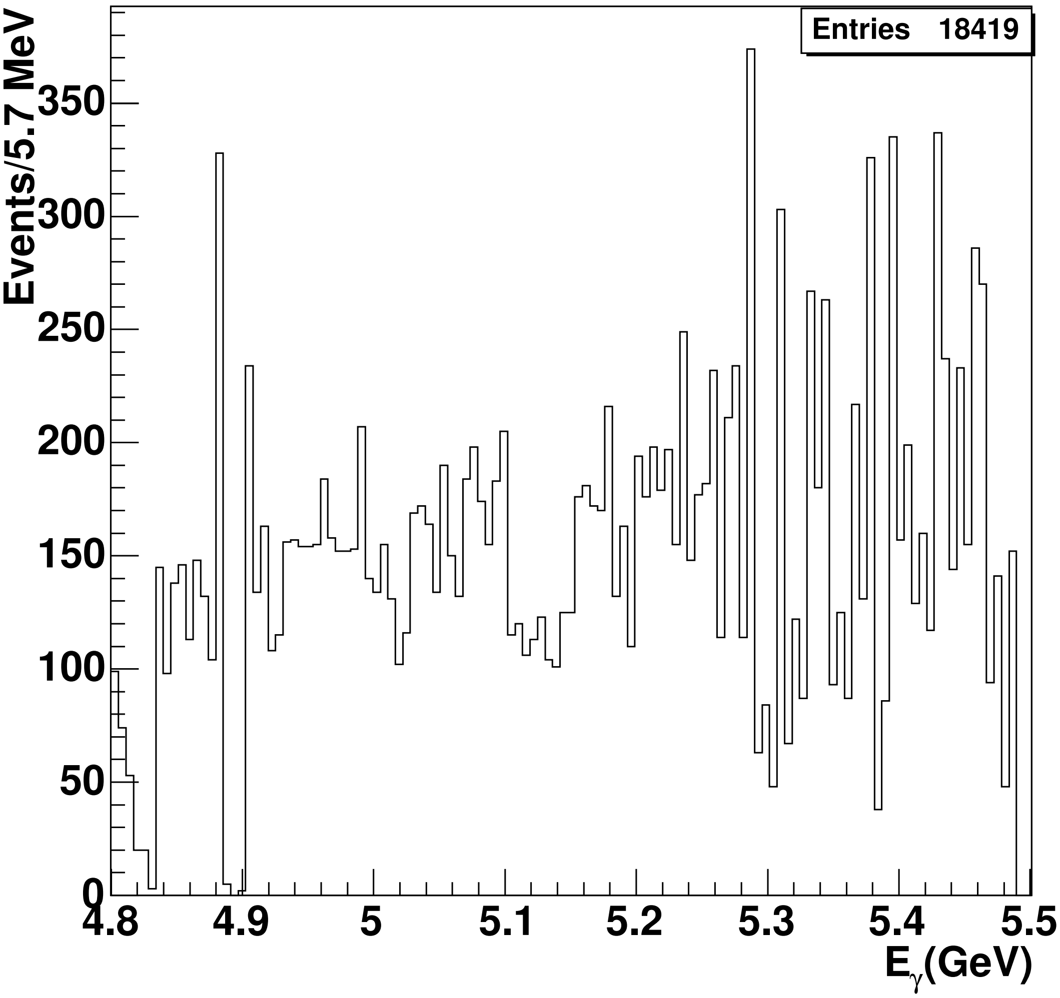

Figure 6.1. The beam energy distribution for the accepted $\gamma p \rightarrow pp\bar{p}$ events. The histogram is binned such that each bin corresponds to a single energy counter in the tagger. The energy resolution is $0.001E_0$ where $E_0 = 5.75$ GeV is the electron beam energy. The large bin-to-bin deviations are caused by inefficiencies of individual tagger elements.

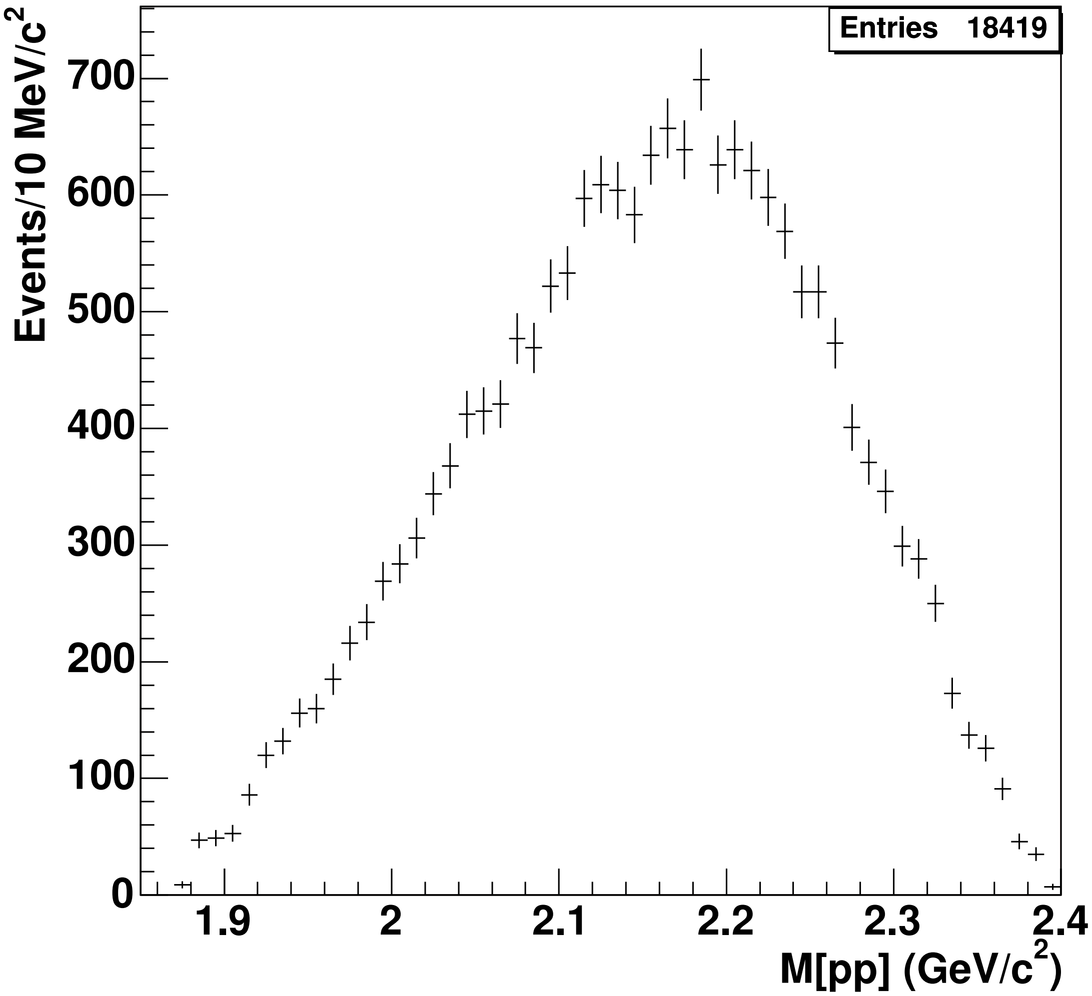

Figure 6.2. The two proton invariant mass distribution. The distribution rises linearly from 1.9 GeV/c^2, peaking at 2.2 GeV/c^2. It then turns over and decreases linearly to 2.4 GeV/c^2. No obvious resonant-like structures are observed.

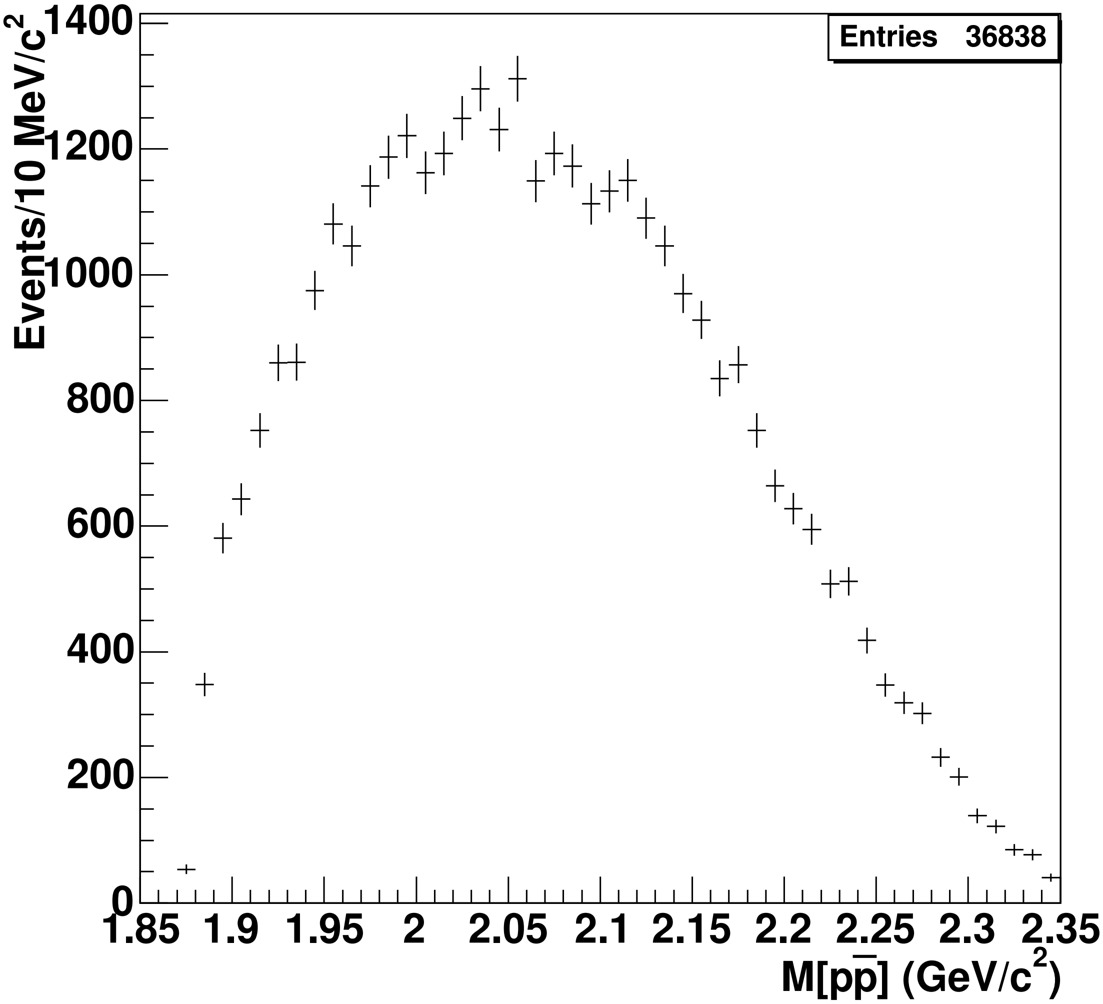

Figure 6.3. The invariant mass distribution for all proton-antiproton combinations. While some structure is seen in the intermediate mass region, these variations are consistent with statistical fluctuations. No obvious narrow resonances are observed.

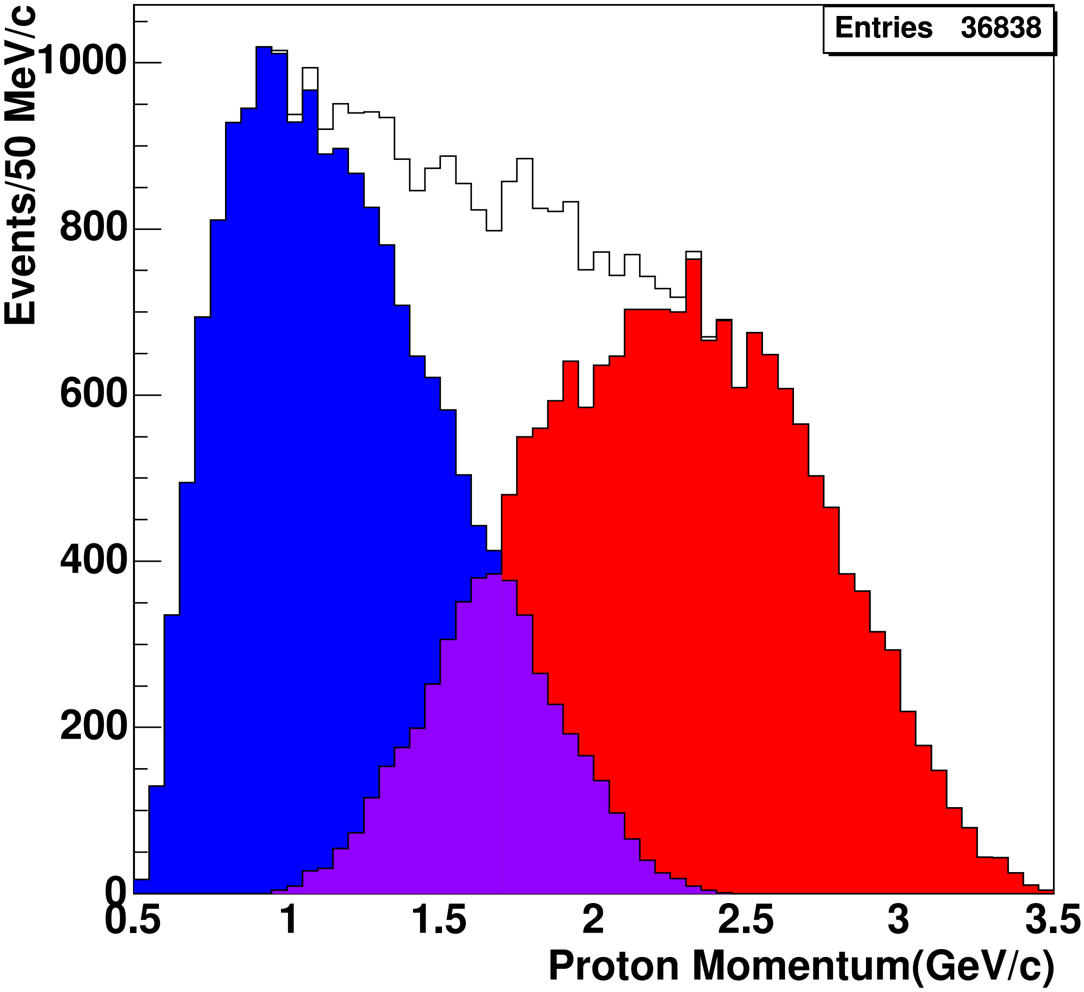

Figure 6.4. The proton momentum in the lab frame. The white distribution represents the overall proton momentum distribution. The red distribution represents the momentum distribution for the slower protons, and the blue represents the faster protons. The purple area simply represents the overlapping between the blue and the red.

maximum near 2.0 GeV/c^2 and decreases almost linearly to 2.35 GeV/c^2. The mass region between 1.95 GeV/c^2 and 2.15 GeV/c^2 contains several fluctuations.

Neither of the distributions exhibit narrow peaks or obvious resonant structure. Recall that a $p\bar{p}$ resonance was previously observed at 2.02 GeV/c^2 [14][15][16]. Because this data does not show obvious resonant-like structures, an upper limit on the production cross section of a 2.02 GeV/c^2 $p\bar{p}$ resonance will be calculated later in Chapter 8. Additionally, the threshold baryonium state seen by BES is also not observed [21]. A threshold $p\bar{p}$ resonance would have very small breakup momentum. The $p\bar{p}$ pair from a threshold resonance would be boosted together in the forward direction and would be less likely detected in CLAS. A threshold $p\bar{p}$ pair with small breakup momentum is likely forward-going and would have poor detector acceptance. Additionally, the CLAS detector is limited in reconstructing close particle tracks [51]. For a proton-antiproton pair with small breakup momentum, the tracks may share similar hits in the Region 1 drift chambers. The tracks would then separate as they pass through the magnetic field into Region 2. The track reconstruction does not allow for the sharing of hits, and thus at least one of these tracks would be lost. While observing both protons and the antiproton improves the mass resolution, measuring the two final state protons and identifying the antiproton via four-momentum conservation greatly enhances the detector acceptance for $\gamma p \to pp\bar{p}$, in particular for events with $p\bar{p}$ near threshold.

Figure 6.7 shows a Dalitz plot which plots the $p_{fast}\bar{p}$ mass squared versus the $p_{slow}\bar{p}$ mass squared. In a Dalitz plot, a narrow two-body resonance would appear as an enhanced vertical, horizontal, or diagonal band. No resonant features are observed in the Dalitz plot.

6.3 Angular Distributions

Angular distributions are useful for studying the dynamics of the system. In order to interpret angular distributions, one must take into account the limitations

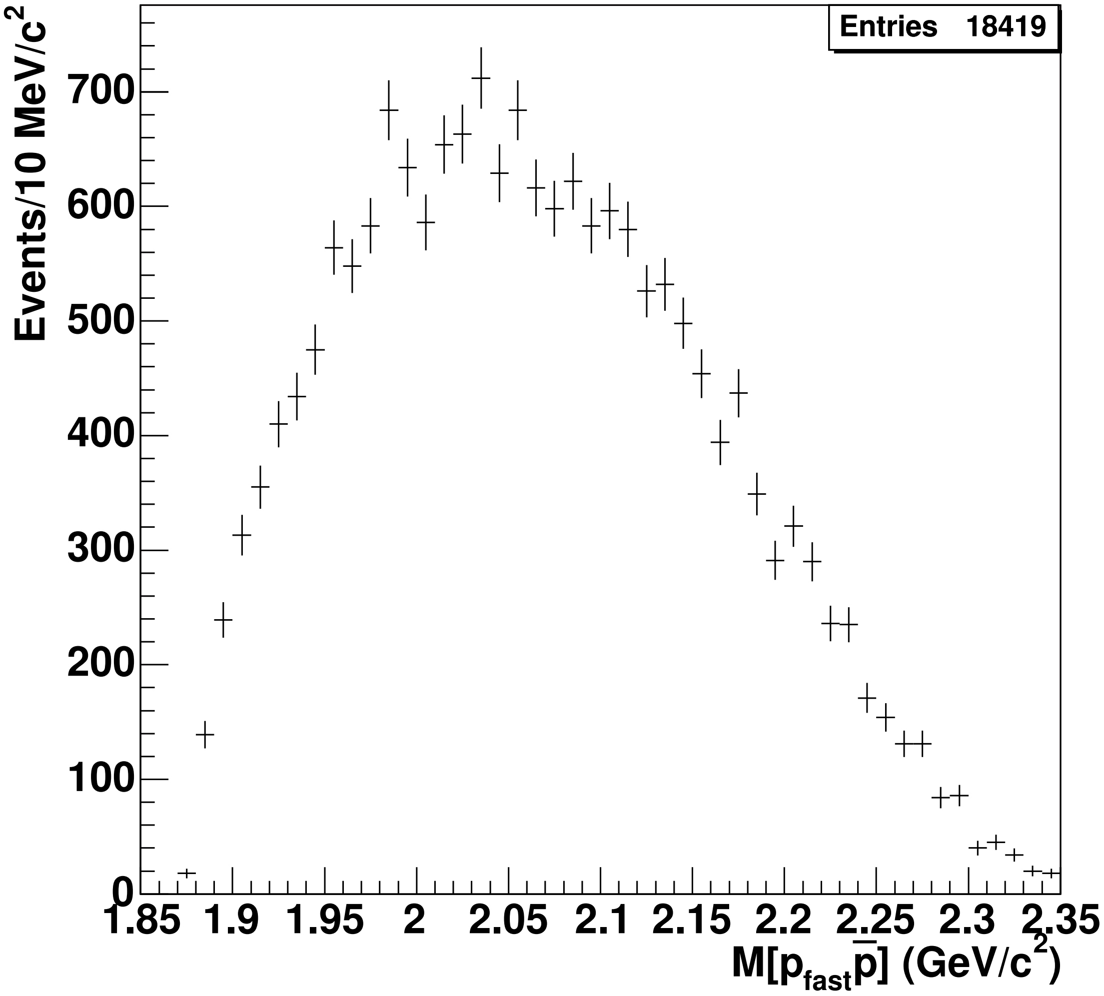

Figure 6.5. The $p_{fast}\bar{p}$ invariant mass distribution. The distribution increases rapidly from 1.87 GeV/c^2 to 1.92 GeV/c^2. It then rises more gradually until a maximum near 2.0 GeV/c^2. Just after 2 GeV/c^2 the distribution turns over and decreases steadily to 2.35 GeV/c^2. No obvious narrow resonant structures are seen.

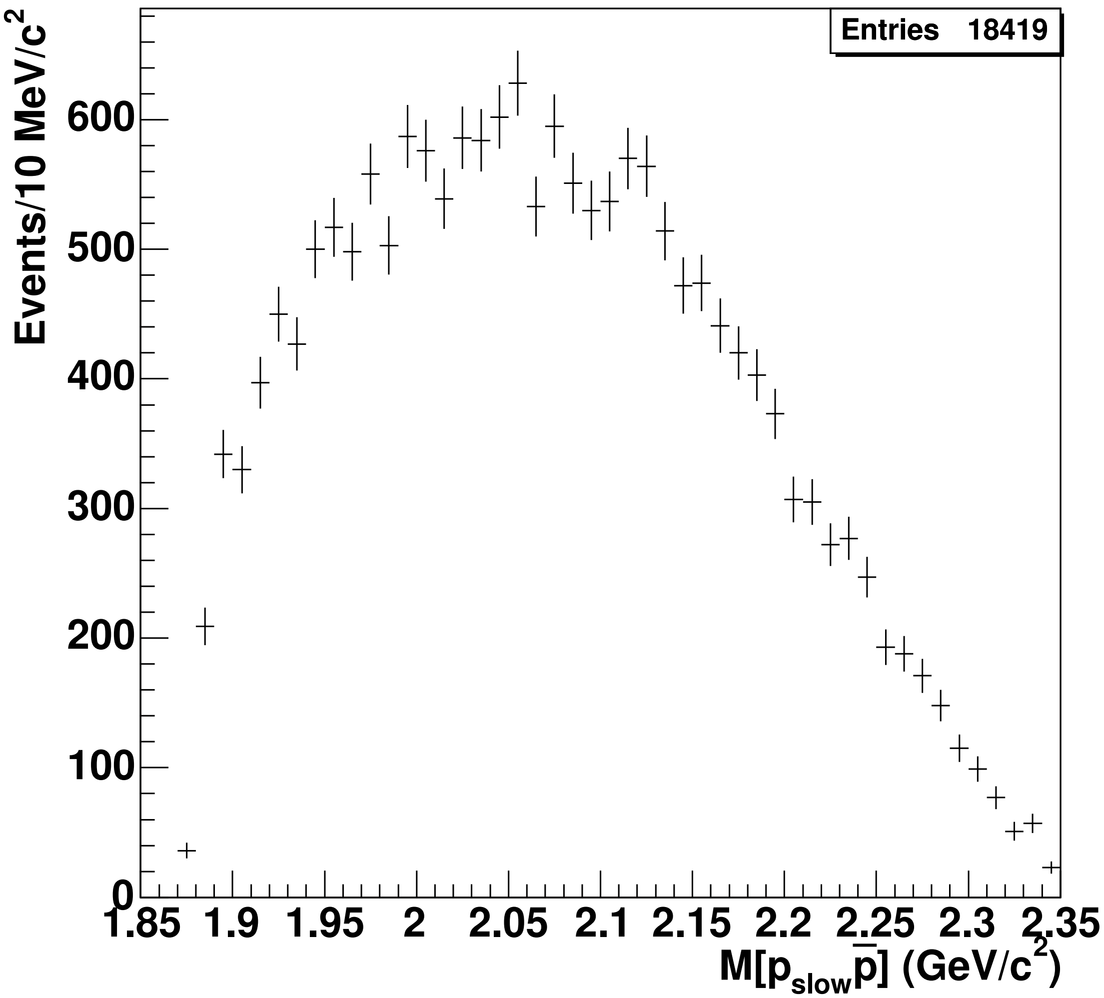

Figure 6.6. The $p_{slow}\bar{p}$ invariant mass distribution. The distribution increases rapidly from 1.87 GeV/c^2 until 1.95 GeV/c^2. The distribution reaches a maximum near 2.0 GeV/c^2 and decreases almost linearly to 2.35 GeV/c^2. The mass region between 1.95 GeV/c^2 and 2.15 GeV/c^2 contains several fluctuations. No narrow resonance is observed at the mass of 2.02 GeV/c^2 where a resonance was claimed previously. No other narrow resonant-like features are observed. The structures are consistent with statistical fluctuations.

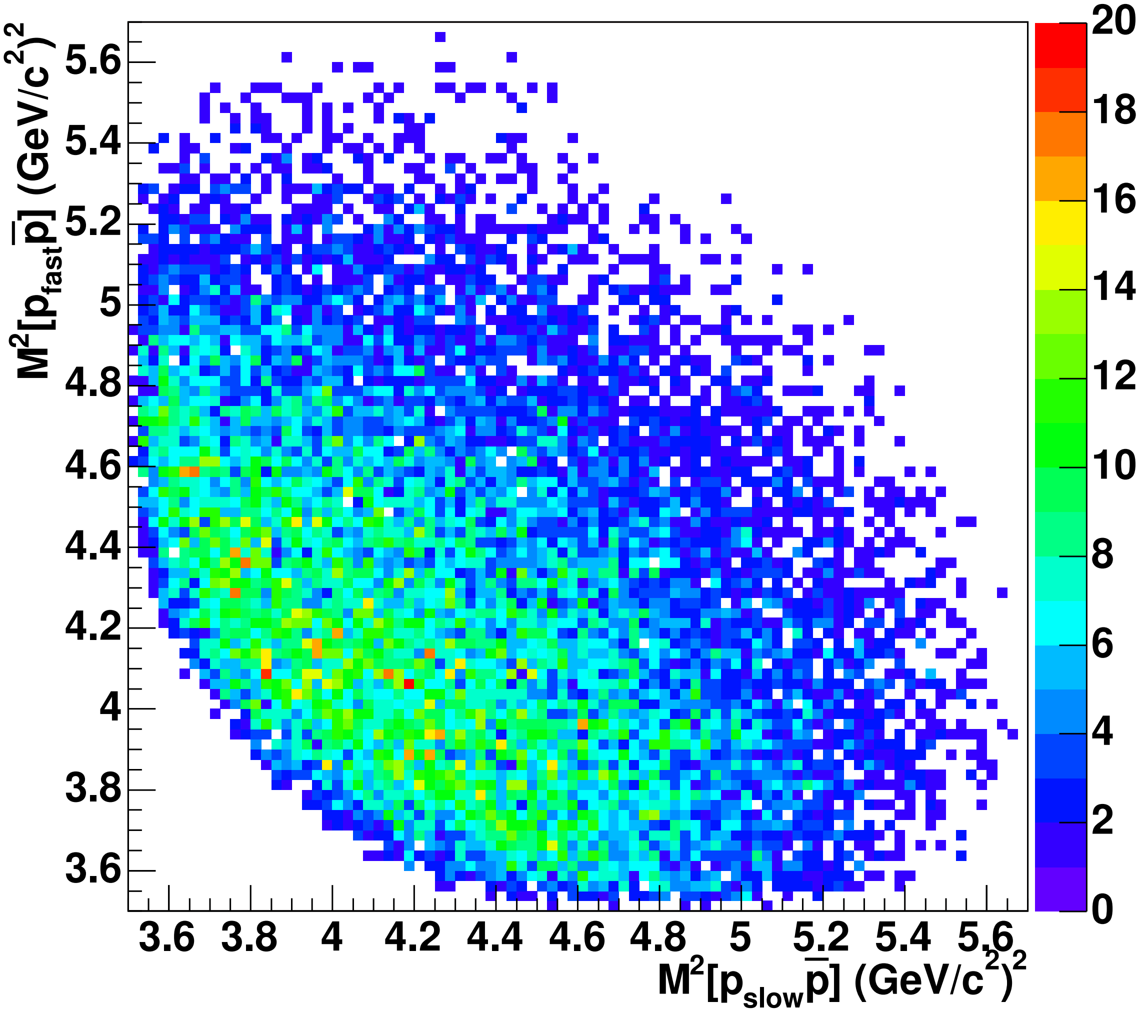

Figure 6.7. The Dalitz plot of $p_{fast}\bar{p}$ mass squared versus the $p_{slow}\bar{p}$ mass squared. Note that this distribution is not corrected for acceptance. A two-body resonance would appear as an enhanced vertical, horizontal, or diagonal band. Note that the distribution is not corrected for acceptance. No resonant features are observed.

Table 6.1. The table summarizes the definitions of the angles used in this section. The CM frame was obtained by boosting from the lab frame. The $\bar{p}p$ rest frames were obtained by boosting from the CM frame.

Reference Frame Definitions				
Angles	Frame	Vector	$\hat{z}$	$\hat{y}$
θ_{fast}^{CM}	CM	$(\bar{p}p_{fast}) - direction$	$\hat{\gamma}$	$(\bar{p}p_{fast}) - direction \times \hat{\gamma}$
θ_{slow}^{CM}	CM	$(\bar{p}p_{slow}) - direction$	$\hat{p_T}$	$(\bar{p}p_{slow}) - direction \times \hat{p_T}$
θ_{fast}^{rest},ϕ_{fast}^{rest}	$\bar{p}p_{fast}$ rest	$\hat{\bar{p}}$	$\hat{\gamma}$	$(\bar{p}p_{fast}) - direction \times \hat{\gamma}$
θ_{slow}^{CM},ϕ_{fast}^{rest}	$\bar{p}p_{slow}$ rest	$\hat{\bar{p}}$	$\hat{p_T}$	$(\bar{p}p_{slow}) - direction \times \hat{p_T}$

of the detection system. General features of the angular distributions can aid in the understanding of possible production mechanisms, whereas detailed studies of angular decays can identify resonance spin-parity properties.

In order to measure the decay angles, the scattering plane must first be defined. First, the lab frame must be boosted to the center-of-momentum(CM) frame along the direction of the photon. The CM frame is pictured in Figure 6.8. In the overall CM frame, $\hat{z}_{CM}$ is defined by the initial beam direction, and the normal to the reaction plane defines $\hat{y}_{CM}$. $\hat{x}_{CM}$ is defined as usual by the right hand rule, $\hat{x}_{CM} = \hat{y}_{CM} \times \hat{z}_{CM}$. Refer to Table 6.1 for a summary of the definitions of angles and axes.

Figure 6.9 shows the distributions the angle the $p_{fast}\bar{p}$ and the $p_{slow}\bar{p}$ systems make with the beam in the CM frame. The $cos(\theta_{fast}^{CM})$ distribution is forward-peaked with a sudden decrease in events in the extreme forward region, due to a loss of protons in the beam line. The $cos(\theta_{slow}^{CM})$ distribution is strongly affected at the backward angles. Low momentum protons have low acceptance due to not exiting the target or from bending too much in the magnetic field so that they aren't detected by CLAS.

With the scattering planes defined in the CM frame, the particles are then boosted to the $\bar{p}p$ rest frames. The rest frame for the $\bar{p}p_{fast}$ system is oriented so that the z-axis is along the boosted beam direction, and the y-axis is retained from the scattering

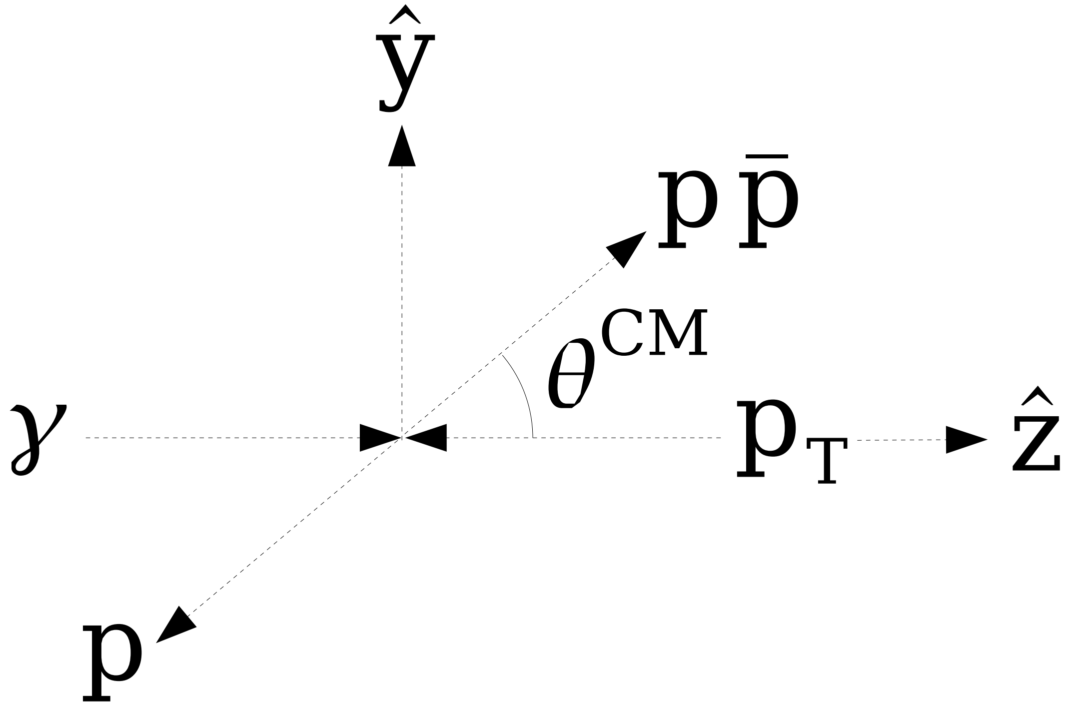

Figure 6.8. The center-of-momentum frame. For the $p_{fast}\bar{p}$ system, $\hat{z}_{CM}$ is defined by the initial beam direction. For the $p_{slow}\bar{p}$ system, $\hat{z}_{CM}$is defined by the initial target(p_T) direction(opposite the direction shown in the diagram). The normal to the reaction plane defines $\hat{y}_{CM}$. $\hat{x}_{CM}$ is defined as usual by the right hand rule, $\hat{x}_{CM} = \hat{y}_{CM} \times \hat{z}_{CM}$. θ^{CM} is defined by the angle that the $p\bar{p}$ system makes with the z-axis, which is along the direction of the beam.

plane, which is invariant to the boost. The rest frame for the $\bar{p}p_{slow}$ system is similar, except that the z-axis is along the boosted target proton direction.

In the $p\bar{p}$ rest frame, the angle θ is defined as the angle the antiproton direction makes with the z-axis, and the angle ϕ is the angle the antiproton direction makes with respect to the x-axis in the x-y-plane. Figure 6.10 shows the $cos(\theta^{rest}_{fast})$ and $cos(\theta^{rest}_{slow})$ distributions. The $cos(\theta^{rest}_{slow})$ distribution appears that it may be described by an exponential function, and its relationship to the production mechanisms will be discussed in Chapter 7. The $cos(\theta^{rest}_{fast})$ distribution peaks backwards with a severe dropoff at backward angles. Figure 6.11 shows the azimuthal angular distributions,

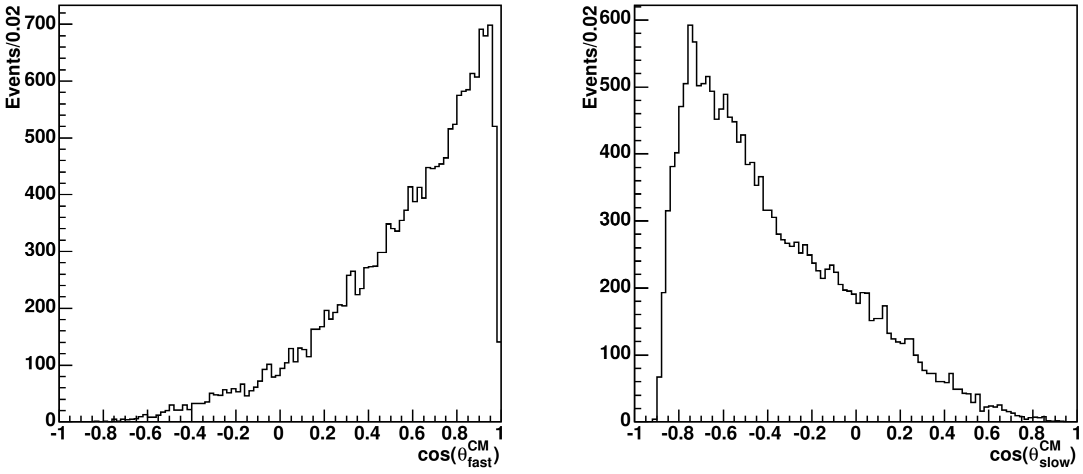

Figure 6.9. Angular distributions in the CM frame. The left-hand distribution is forward peaking because the high momentum protons are generally forward-going. The right-hand distribution is backward peaking because the low momentum protons are generally backward-going. The $cos(\theta^{CM}_{slow})$ distribution is strongly affected at the backward angles. Low momentum protons have low acceptance due to not exiting the target or from bending too much in the magnetic field so that they aren't detected by CLAS.

and figure 6.12 shows the $cos(\theta)$ versus ϕ distributions. These distributions are described by kinematic dependencies and detector acceptance (to be discussed in Chapter 7).

6.4 Momentum Exchange

The variables which will be discussed here were defined in section 2.3. Figure 6.13 shows the t^{meson} and t^{baryon} distributions. The four-momentum exchange distributions provide insight on the production via exchange particles. The limited amount of phase space places boundaries on the values of t^{meson} and t^{baryon}. See for example Figure 6.14 which shows t^{baryon} versus the $p_{slow}\bar{p}$ invariant mass. The solid line represents the kinematic limits. The limits on the four-momentum exchange depend on the photon energy and the $p\bar{p}$ invariant mass. With a large threshold $p\bar{p}$

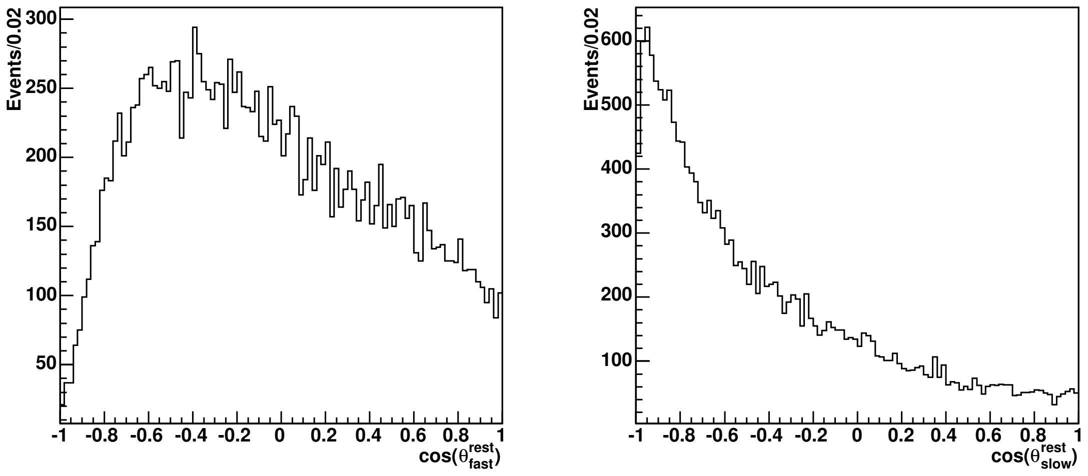

Figure 6.10. The $cos(\theta^{rest}_{fast})$ and $cos(\theta^{rest}_{slow})$ distributions in the $\bar{p}p$ rest frames. The backward-peaking of the $cos(\theta^{rest}_{slow})$ distribution indicates that the antiproton is generally forward-going (along the beam) in the $p_{slow}\bar{p}$ rest frame.

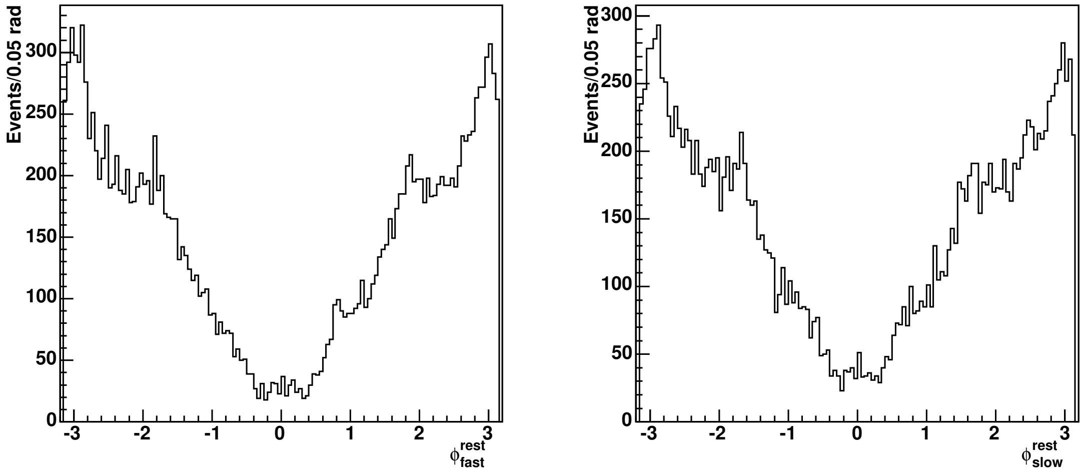

Figure 6.11. The ϕ^{rest}_{fast} and ϕ^{rest}_{slow} distributions in the $\bar{p}p$ rest frames. The angle is measured with respect to the antiproton. The z-axis is in the direction of the beam for ϕ^{rest}_{fast} and in the direction of the target for ϕ^{rest}_{slow}.

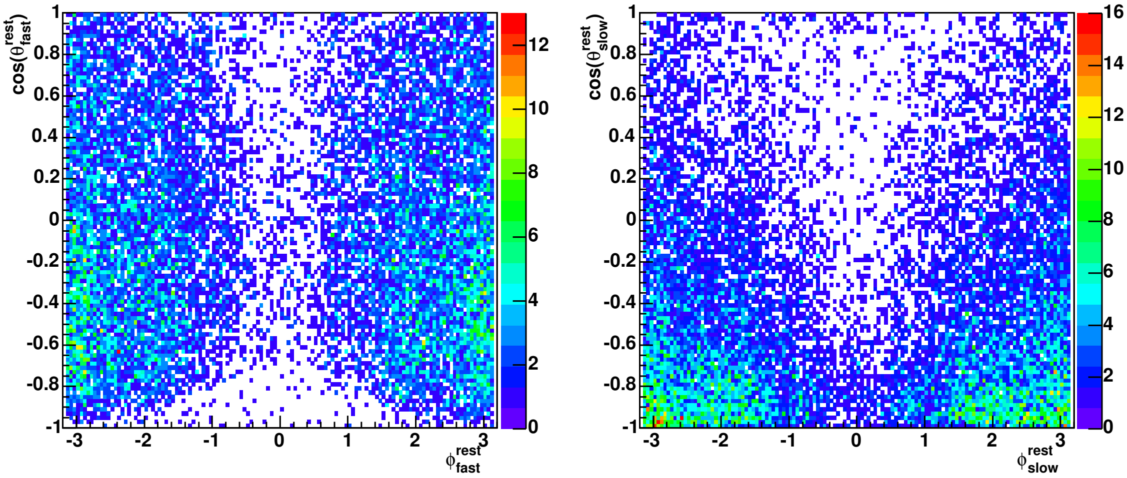

Figure 6.12. The $cos(\theta^{rest})$ versus ϕ^{rest} distributions in the $\bar{p}p$ rest frames. The rest frame for the $\bar{p}p_{fast}$ system is oriented so that the z-axis is along the boosted beam direction, and the y-axis is retained from the scattering plane, which is invariant to the boost. For the $\bar{p}p_{slow}$ system, the z-axis is along the boosted target direction. The angles are measured with respect to the antiproton direction in both rest frames.

invariant mass, the momentum exchange distributions are strongly affected by these limitations. To analyze the momentum exchange without these effects, t^{meson} and t^{baryon} were normalized by their minimum values(t_{min}). This effectively removes the photon energy and mass dependence from the momentum exchange distributions. The t_{min} functions were determined by the beam energy and the mass of the $\bar{p}p$ system.

$$t^{'}_{m} = t^{meson} - t^{meson}_{min}$$

$$t^{'}_{b} = t^{baryon} - t^{baryon}_{min}$$

The $t^{'}_{m}$ and $t^{'}_{b}$ distributions are shown in Figure 6.15. $t^{'}_{m}$ peaks much closer to zero and takes on a somewhat simpler shape. This feature will be exploited when attempting to fit the data using Monte Carlo simulations as will be shown in Chapter 7.

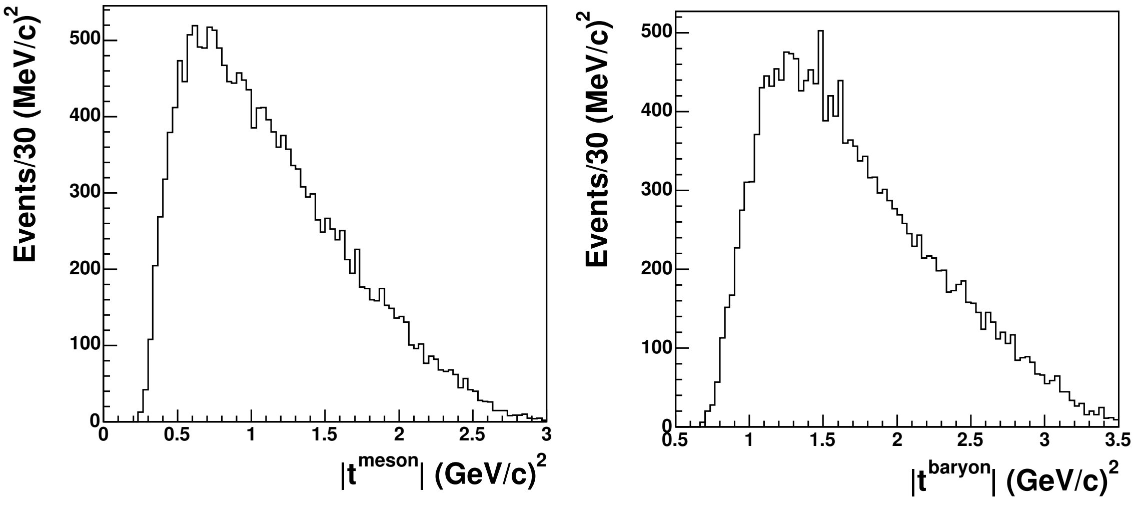

Figure 6.13. The t^{meson} (meson exchange) and t^{baryon} (baryon exchange) distributions. The momentum exchange can provide insight on the production via exchange particles. This will be discussed in a following chapter as Monte Carlo events are fit to these distributions.

6.5 Missing Proton Data

The data used throughout this analysis allows an antiproton to be missed by the CLAS detector. However it is also possible to analyze data in which a proton and antiproton were detected, whereas a proton was missed. These events were analyzed to search for resonant structure in the invariant mass distributions. There are significantly fewer events with a missing proton. The antiproton acceptance is much lower than the proton acceptance because they were often lost in the beam line. Therefore these events require the unlikely detection of an antiproton coupled to the loss of a proton.

Figure 6.16 shows the $p_{fast}\bar{p}$ and the $p_{slow}\bar{p}$ invariant mass distributions. The $p_{fast}\bar{p}$ distribution increases gradually from 1.88 GeV/c^2 to 2.10 GeV/c^2. It then levels out until around 2.22 GeV/c^2 where it turns over. It then decreases rapidly to 2.35 GeV/c^2. This distribution differs from that of the missing antiproton data by increasing less rapidly near threshold. This is expected due to the decreased

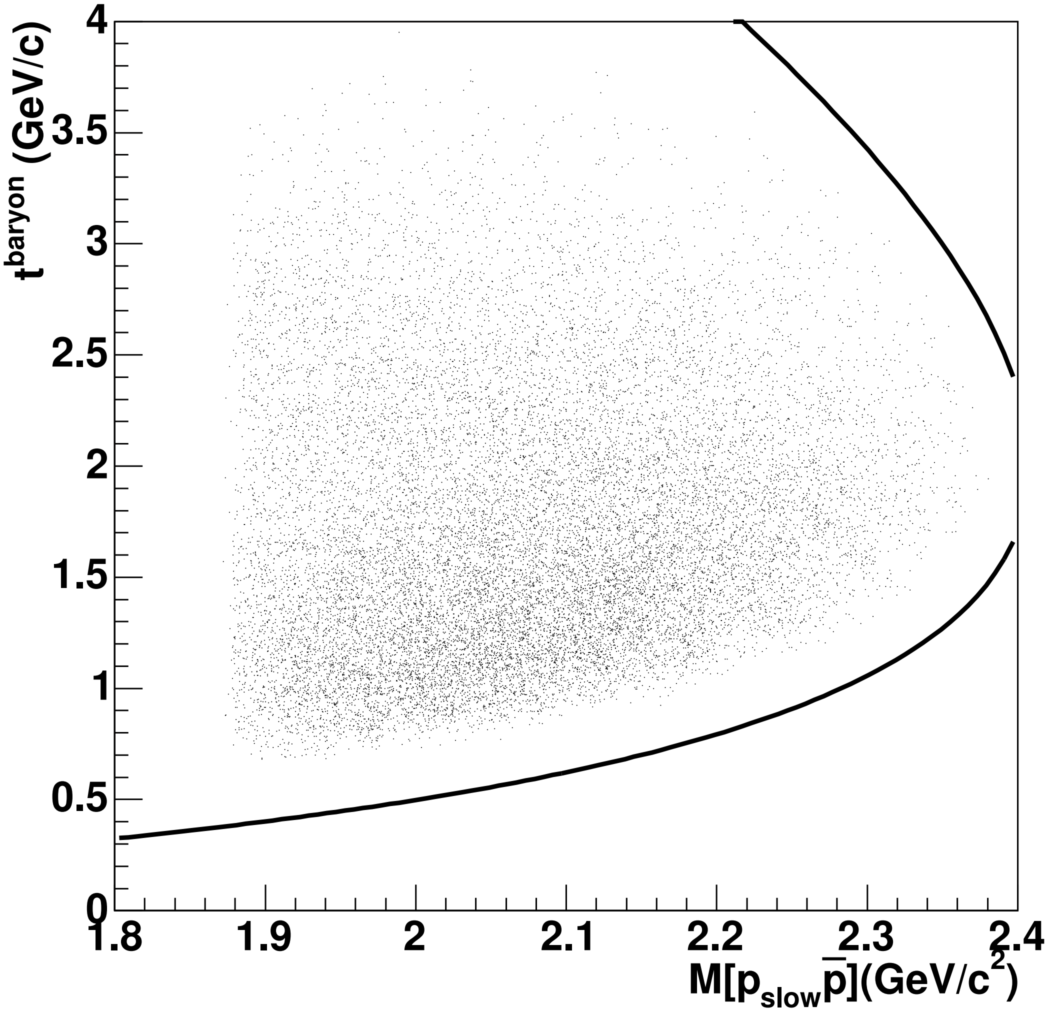

Figure 6.14. t^{baryon} versus the $p_{slow}\bar{p}$ invariant mass. The curve represents the boundary due to the available phase space for the maximum photon beam energy of 5.5 GeV. Decreasing the beam energy shrinks the envelope for the possible t^{baryon} and $p\bar{p}$ invariant mass values. The gap between events and the boundary is due to the the loss of particles in the beam line regions.

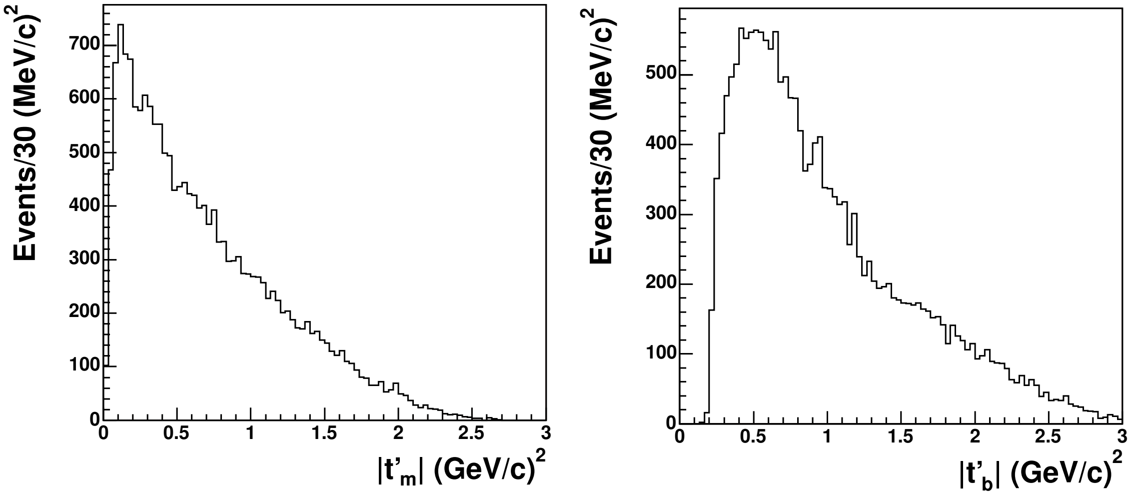

Figure 6.15. The $t_m^{'}$ and $t_b^{'}$ distributions. $t_m^{'}$ and $t_b^{'}$ are defined as $t_m^{'} = t^{meson} - t_{min}^{meson}$ and $t_b^{'} = t^{baryon} - t_{min}^{baryon}$ respectively. t_{min}^{meson} and t_{min}^{baryon} are the minimum values of t^{meson} and t^{baryon}, which are dependent on phase space.

sensitivity to threshold $p\bar{p}$ mass for events requiring a detected antiproton. The $p_{slow}\bar{p}$ invariant mass distribution increases gradually from 1.87 GeV/c^2 to 2.08 GeV/c^2. It then turns over and decreases gradually to 2.35 GeV/c^2. The $p_{slow}\bar{p}$ distribution also differs from that of the missing antiproton data. No obvious narrow resonant structures are seen in either of the mass distributions.

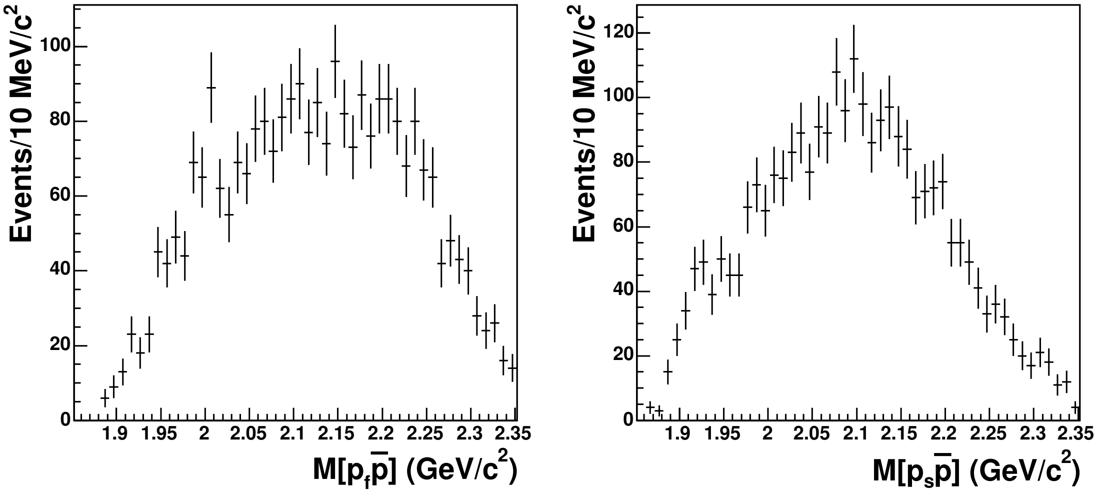

Figure 6.16. The $p_{fast}\bar{p}$(left) and the $p_{slow}\bar{p}$(right) invariant mass distributions are shown for events with an antiproton detected and a proton missed. The $p_{fast}\bar{p}$ distribution increases gradually from 1.88 GeV/c^2 to 2.10 GeV/c^2. It then levels out until around 2.22 GeV/c^2 where it turns over. It then decreases rapidly to 2.35 GeV/c^2. The $p_{slow}\bar{p}$ invariant mass distribution increases gradually from 1.87 GeV/c^2 to 2.08 GeV/c^2. It then turns over and decreases gradually to 2.35 GeV/c^2. No obvious narrow resonant structures are observed.

CHAPTER 7

MONTE CARLO SIMULATIONS

7.1 Introduction

Monte Carlo events are computer simulations of the physics involved in an analysis. These simulations are based upon our knowledge of the physical processes of the particles traversing the medium, the kinematic variables associated with the reaction, and our understanding of the CLAS detector. The goal of these simulations is to describe, as accurately as possible, the physics involved with the analysis. This includes, but is not limited too, the understanding and description of the beam, the target, the CLAS detector, the data collection, and the kinematics involved with the reaction under analysis.

Monte Carlo events are used to measure the acceptance of $\gamma p \to pp[\bar{p}]$ events within the CLAS detector. They are also used to estimate invariant mass resolution and to define cuts associated with the inefficiencies of the CLAS detector. Monte Carlo events for this analysis simulate a $pp\bar{p}$ system leaving the target and traveling through CLAS according to our understanding of the kinematic variables and physical model of the reaction. The target interaction vertex was simulated by spreading the vertex position of the interaction throughout a volume identical to the target. The photon beam was simulated by weighting events according to the expected energy spectrum produced by a bremsstrahlung beam. Hits are generated in detector elements and the events are then reconstructed. The events are generated according to a weighting scheme, which will be described in a later section.

The CLAS program GSIM [46] uses the GEANT [52] routines from the CERN libraries as a framework for a Monte Carlo simulation of the CLAS detector. The GEANT program describes the passage of elementary particles through matter. It tracks particles through the experimental setup and simulates detector response. Using generated events, the protons are traced through CLAS using GSIM.

By default, the detector hits in simulated events have perfect timing and resolution. Because detector elements change over time due aging, malfunctions, repairs, etc., a database is used to keep track of the functionality of these elements over time. The CLAS program GEANT Post Processor(GPP) uses this database to make the simulated detector hits more physical. GPP removes hits with dead drift chamber(DC) wires, bad tagger counters, and dead Time-of-Flight(TOF) paddles. It also smears the DC, TOF, and tagger values according to their measured resolution. GPP also has the capability of applying the trigger logic to the events to check whether they would be accepted using the experiment's trigger requirements.

After applying GPP to the simulated events, the CLAS program a1c [47] is used to perform event reconstruction. A1c is used to reconstruct events for both the Monte Carlo simulations and the experimental data. The overall event reconstruction was described in Chapter 4. The tagger information is used to generate a list of tagged photons for each event, each of which will have an appropriate vertex time and energy. The a1c program takes hits in the DC to obtain the track segments and uses these segments and a lookup table to obtain the particle tracks. A1c also evaluates the TOF information to obtain the particle velocities. The event reconstruction then performs particle identification and generates a list of particles detected for each event with their measured four-momentum.

7.2 Proton Momentum Resolution

A Monte Carlo study was performed to estimate the experimental resolution of a proton's initial momentum vector when using GSIM. This study utilized GSIM and was done to understand how much variation in a particle's track occurs. This was done by creating a two proton event, in which both protons have the lab angle $\theta = 0.3$, but have opposite angle ϕ. They were chosen to have a total momentum of $1.57 GeV/c$ which was in the intermediate momentum range for all protons from events accepted in this analysis. These angles and momentum were chosen so that each proton would pass through the central regions of two CLAS sectors, so that there would be a high acceptance rate. The angular acceptance varies greatly when a particle passes through the edges and inefficient regions of detectors. The event was then run through GSIM 10,000 times. The accepted proton momentum distributions were then fit to Gaussian distributions. The lab angle θ had a mean of 0.300 radians with a width of $\sigma_\theta = 2.19 \times 10^{-3}$ radians. ϕ had a shifted mean of 2.2×10^{-4} radians with a width of $\sigma_\phi = 9.5 \times 10^{-3}$ radians. The total momentum had a resolution of $\frac{\sigma_p}{p} = 5.1 \times 10^{-3}$.

7.3 Invariant Mass Resolution

A study was performed to determine the resolution of the invariant mass of the fast proton-antiproton system. This was done to understand the CLAS mass resolution germane to the search for narrow resonant states. This was especially important when comparing results to the previous claims of a narrow resonant state at 2.02 GeV/c^2 with a width of 20-40 MeV/c^2.

Events were generated with a $1 MeV/c^2$ wide bin in mass at four intervals. The events were simulated, and the invariant mass was measured to obtain the width and any shift in the mass. The results shown in Table 7.1 indicate that the mass may shift by about $1 MeV/c^2$, and the width is on the order of $2 - 3 MeV/c^2$. This result indicates that the CLAS resolution is sufficient enough to clearly observe resonant states with widths of the order as that of the $2.02 \pm 0.024 GeV/c^2$ claimed previously [14][15] [16].

Table 7.1. Invariant mass resolution of the fast proton-antiproton system in CLAS as measured by GSIM. The mass resolution is estimated from GSIM to be 2-3 MeV/c^2.

Invariant Mass Resolution				
Mass input	Mass output	Mass error	Sigma	Sigma error
1.900-1.901	1.9009	1.8×10^{-5}	2.04×10^{-3}	1.5×10^{-5}
2.000-2.001	2.0017	2.7×10^{-5}	3.59×10^{-3}	2.4×10^{-5}
2.100-2.101	2.1020	2.4×10^{-5}	3.39×10^{-3}	2.2×10^{-5}
2.200-2.201	2.2024	2.1×10^{-5}	2.74×10^{-3}	1.9×10^{-5}

7.4 Proton Misidentification

The reaction $\gamma p \rightarrow pp\bar{p}$ has two protons in the final state. Section 6.2 described the method of labeling these protons as p_{fast} and p_{slow}. The protons are labeled according to the magnitude of their momentum in the lab frame. It was assumed that p_{fast} is produced at the photon vertex (see Figure 2.3), and the p_{slow} is produced at the target vertex. One would like to understand how often this assumption fails. In other words, one must determine how often the proton at the photon vertex has less momentum than the proton at the target vertex.

From comparing Monte Carlo simulations to experimental data it appears that the data was dominated by peripheral $p\bar{p}$ production, or meson exchange production. Because of this, the proton misidentification problem was studied using two-body meson exchange Monte Carlo events. These events were weighted using an exponential distribution in t'_m. The misidentification was measured as a function of the exponential slope b.

For two-body meson exchange Monte Carlo events, a $p\bar{p}$ system is produced at the photon vertex. Therefore, the proton of this system should have more momentum than the recoil proton. The system is given an isotropic decay angular distribution, which means that the proton is emitted in a random direction in the $p\bar{p}$ rest frame. Sometimes the proton is emitted in the direction opposite the beam. In this case, after boosting the proton back to the lab frame, it will have less momentum than if it had been emitted in the same direction as the beam. Sometimes it will have less momentum in the lab frame than the other proton. It is in these cases that the protons are misidentified.

Because t' is a measure of the amount of four-momentum transferred to the recoil proton, the t' distribution affects the chance that the protons are misidentified. For instance, a low value of t' means that a small amount of four-momentum was transferred to the target. Thus the $\bar{p}p$ system likely has more momentum, and therefore the proton is more likely to have a greater momentum than the recoil proton. The meson exchange Monte Carlo events were weighted by an exponential function in t',

$$weight = e^{-bt'}$$

This weighting increases the probability that events have small t'. The exponential slope parameter b was varied for several Monte Carlo sets. Figure 7.1 shows the percentage of Monte Carlo events in which the protons were misidentified versus the slope b. In the case where $b = 0(GeV/c)^{-2}$, the protons were misidentified fifty percent of the time. For $b = 2.0(GeV/c)^{-2}$, the protons were only mislabeled ten percent of the time. It was found that the misidentification decreases at roughly an exponential rate. By describing the data using only meson exchange, the t' distribution most closely resembles an exponential function with a slope of 1.5 $(GeV/c)^{-2}$. This would indicate an error of roughly 15% in identifying the protons. However further studies show that the data consists of both baryon and meson exchange processes. The meson exchange has a measured exponential slope of 3.0 $(GeV/c)^{-2}$, which indicates that the proton misidentification for these events is less than 5%.

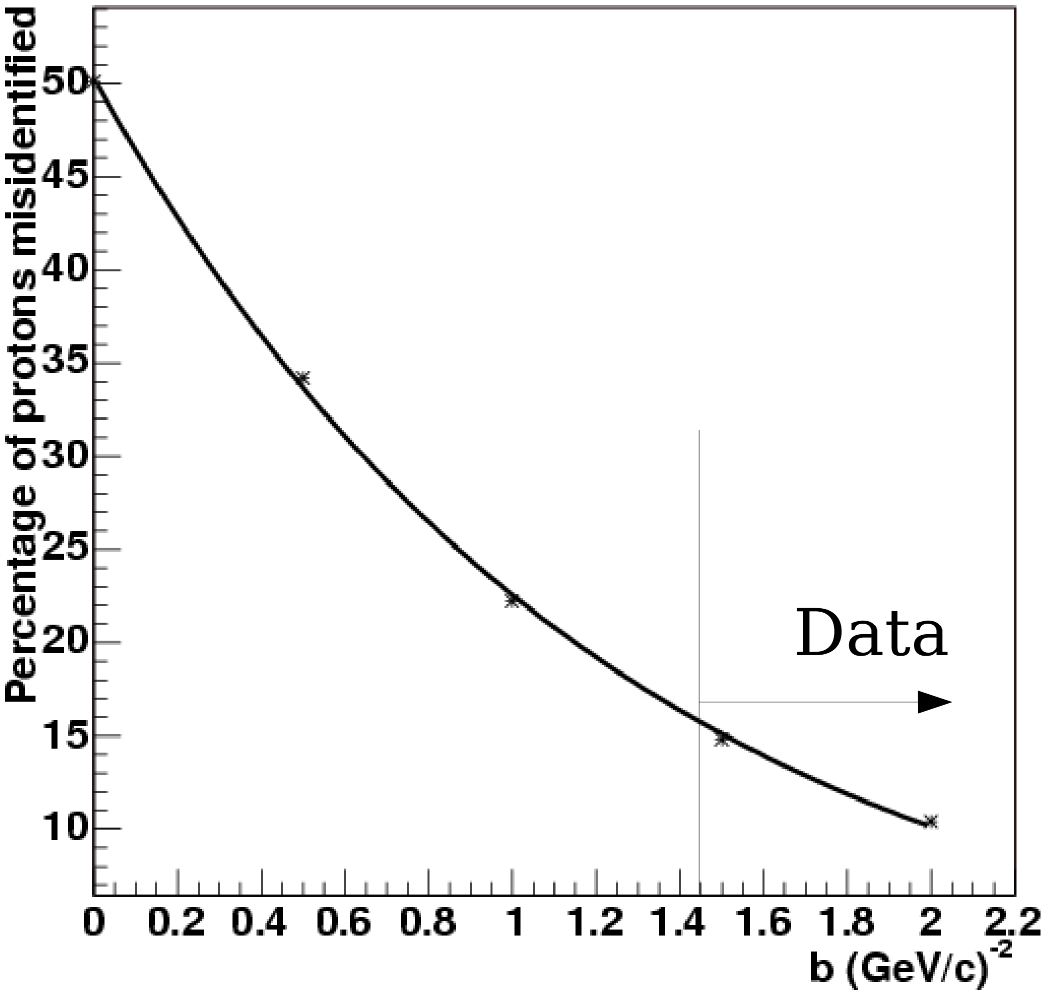

Figure 7.1. Two-body phase space Monte Carlo events were generated with an exponential distribution in t^{meson} with varying exponential slopes b. The figure shows the percentage of events in which the protons were misidentified. As b increases, the misidentification decreases exponentially. An overall fit to the data indicates that the slope is at least 1.5 $(GeV/c)^{-2}$, indicating that the protons are misidentified for less than 15% of the events.

7.5 Monte Carlo Studies on Production Mechanisms

Generating Monte Carlo events requires some basic assumptions about the production and decay mechanisms of the reaction. These assumptions affect the kinematic variables involved, such as invariant mass distributions, angular distributions, and exchange momentum. By comparing the Monte Carlo events to the data, these assumptions may be tested.

7.5.1 Generating Two-Body Phase Space Events

To generate Monte Carlo events which simulate a meson or baryon exchange mechanism, a two-body phase space model was employed. The choice of generating two-body meson or baryon exchange, or three-body phase space will be discussed in the following section. Two-body phase space events were generated according to the reaction $\gamma p \rightarrow pX$,$X \rightarrow p\bar{p}$. The phase space was defined as the two dimensional space with the axes defined as the center-of-mass(CM) breakup momentum(p_{CM}) and the the breakup momentum of the X to $p\bar{p}$ ($p_{Xbreakup}$).

For each event, the beam energy was chosen randomly from the range 4.8-5.5 GeV. A Bremsstrahlung beam energy distribution would be more appropriate, and was used for the final MC simulations. However, over the small energy range, a random distribution serves as a good approximation. The z-position of the vertex was chosen randomly in the range -110 to -90 cm, according to the position and size of the target. The (x,y) positions were fixed at (0,0). Experimentally, the spread of the beam is on the order of a millimeter. The resolution of the CLAS vertex reconstruction is on the order of centimeters. Thus, the generated transverse position of the beam may be safely approximated as a point.

The invariant mass of X was chosen randomly from the range 1.8-2.4 GeV/c^2. To simulate the meson or baryon exchange, the momentum transfer t^{meson} or t^{baryon}, defined in Chapter 2, was weighted by an exponential function, Ce^{-bt}. The exponential slopes used for simulation ranged from 0-3.5 $(GeV/c)^{-2}$. The CM breakup momentum was then calculated from the total energy, the mass of X, and the mass of the proton. The angle θ the X makes with the z-axis was also calculated from the momentum exchange, the beam energy, and the X mass. The azimuthal angle ϕ, however, was chosen randomly from $[-\pi, \pi]$.

The angular distribution of the decay of X to $p\bar{p}$ was generated isotropically, meaning that ϕ_X was chosen randomly on the range $[-\pi, \pi]$, and $cos(\theta_X)$ was chosen randomly on the range $[-1, 1]$. The angular distributions were generated this way so as not to introduce any angular dependence in the Monte Carlo simulations. The events were then weighted according to phase space. This was done by first determining the largest value of the Lorentz factor $f = p_{CM} \times p_{Xbreakup}$ obtained from a large number of trial events. Then for each generated event f was calculated, and a random number r was chosen on the range $[0, f_{max}]$. If f was less than r, the event was discarded.

This phase space weighting increases the probability for events to share the available momentum between the breakup momentum in the CM frame and the X rest frame. It decreases the probability for events to have extremes in the breakup momentum, such as a large CM breakup momentum and a very small X rest frame breakup momentum, or vice versa. The maximum of the Lorentz factor was mainly dependent on the beam energy. Thus the range of the beam energy is the source of the limitations on phase space.

7.5.2 Angular Dependencies on Production Mechanisms

Events were generated using two-body phase space under both a meson exchange and a baryon exchange mechanism. The exponential slopes used to generate these events was 1.5 $(GeV/c)^{-2}$ for meson exchange and 1.4 $(GeV/c)^{-2}$ for baryon exchange. These values were the best fit of each of the exchange processes to the data. For the measured angular distributions in the rest frames of the $\bar{p}p_{fast}$ and the $\bar{p}p_{slow}$ systems differed greatly from the two models as seen in Figure 7.2. The meson exchange events exhibit an exponential form in the $cos(\theta)$ distribution in the $\bar{p}p_{slow}$ rest frame. Under baryon exchange, the exponential form appears instead in the $cos(\theta)$ distribution of the $\bar{p}p_{fast}$ system. These Monte Carlo distributions were compared with those of the data. The observed data agrees well with the meson exchange distributions for $cos(\theta_{slow})$, which implies that the observed data has a large contribution of meson exchange production.

7.5.3 t'_m Analysis

Assuming a meson exchange process, Monte Carlo events were generated by weighting the t'_m distribution ($t'_m = t - t_{min}$). The t'_m intensity distribution should follow

$$I(t'_m) \propto f(t'_m) \times (phasespace) \times (acceptance)$$

where $f(t'_m)$ is the "true" functional form of the t'_m distribution. The simplest assumption is that $f(t'_m)$ takes the exponential form

$$f(t'_m) = e^{-bt'_m}$$

Two-body phase space events generated with varying slopes in t'_m are shown compared to the data in Figure 7.4. The t'_m distribution cannot be explained by a simple exponential weighting. Events generated with an exponential slope of $b = 1.0(GeV/c)^{-2}$ fit the data well at low t'_m, while failing at high t'_m. Whereas events generated with a slope of $b = 2.0(GeV/c)^{-2}$ fits the data poorly at low t'_m, but very well at high t'_m. While the data seems to be dominated by meson exchange production, there may be two meson exchange mechanisms with differing exponential slopes, or possible some non-meson-exchange production.

To study additional contributions to the production, it was assumed that $f(t'_m)$ consists of an exponential part as well as a background term,

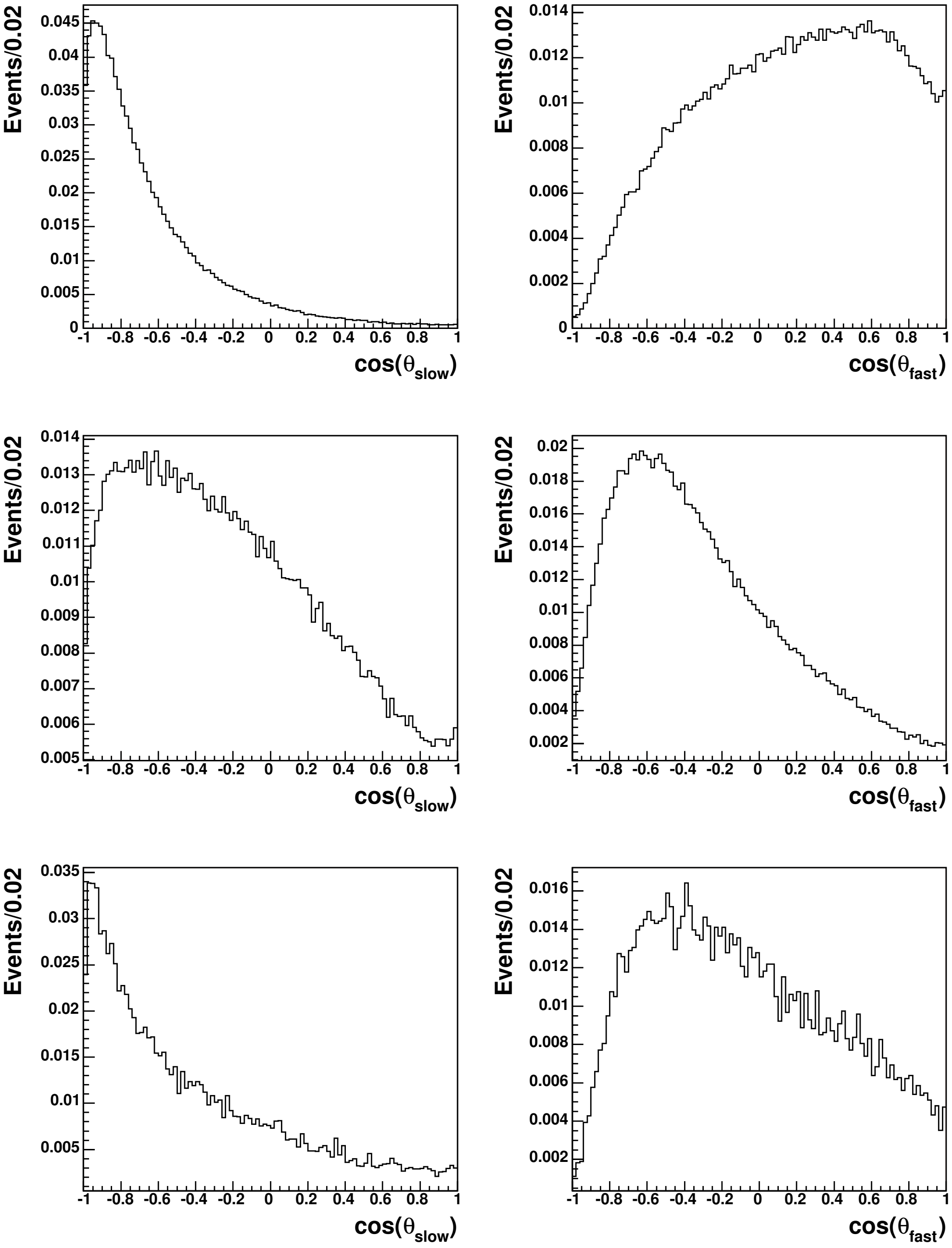

Figure 7.2. The distributions show the angle the antiproton makes with the target proton(photon) in the $p_{slow}\bar{p}(p_{fast}\bar{p})$ rest frame. Top row : Accepted MC events generated using a meson exchange model. Middle Row : Accepted MC events generated using a baryon exchange model. Bottom Row : The observed experimental data.

$$f(t'_m) = e^{-bt'_m} + a(t'_m).$$

To study the t'_m dynamics, the phase space and acceptance were factored out of the intensity,

$$f(t'_m) \propto \frac{I(t'_m)}{(phasespace)(acceptance)}.$$

The procedure involved first generating MC events uniform in t'_m, or $f(t'_m) = 1$. These events were weighted by phase space and then subjected to a simulation of the CLAS detector. The next processing stage involved reconstructing the MC detector hits in a similar fashion as the experimental data was processed. Finally, the data analysis and selection cuts, which were defined using the experimental data, were also applied to the reconstructed MC events. The resulting t'_m distribution is shown in Figure 7.5. The effects of pure phase space and acceptance are seen. Using MC sets generated by weighting t'_m exponentially with varying slopes, the phase space and acceptance dependence were factored out by dividing the t'_m distributions with that of the pure phase space accepted t'_m MC data. It was found that the t'_m dependence regained its exponential form using this method. In Figure 7.3, the corrected t'_m distributions for varying exponential slopes are shown on a log scale. The slope is slightly altered, however this is due to the effects of proton misidentification. The figure shows the slopes used to generate the events versus the measured slope. The error in the slope is linear, and thus can be corrected using this method.

The method was then applied to the experimental data. The resulting t'_m dependence was then fit to an exponential plus a background term, as shown in Figure 7.6. It was found that a constant represents the background term well. The slope of the exponential was measured to be $b = 3.87 \pm 0.14 (GeV)^{-2}$. The constant term may be explained as background events which are independent of t'_m, possibly due to baryon exchange production.

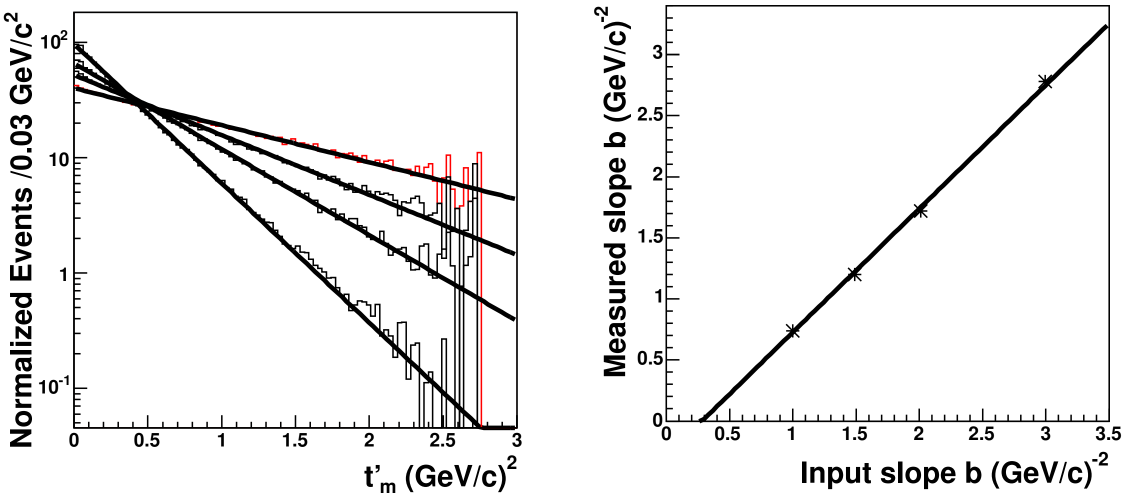

Figure 7.3. Left: Several MC sets were generated with an exponential t'_m distribution with varying slope. The t'_m distributions of the accepted events were then corrected by factoring out the phase space and acceptance. The t'_m distributions regain their exponential form as shown. Right : The exponential slope used to generate the MC events versus the measured exponential slope after phase space and acceptance correction. Some error occurs in the measurement of the exponential slope. This occurs due to proton misidentification. However the slope changes linearly as shown by the fit.

7.5.4 Particle Momentum Dependencies on Production Mechanisms

Comparing meson exchange, baryon exchange, and antibaryon exchange under the assumption that the fast proton was associated with the photon vertex, qualitative statements can be made about the antiproton momentum. Under meson exchange, a meson resonance decays to a fast proton and an antiproton, such that the particle that decays in the forward direction will have the most momentum in the lab frame. If all the events were meson exchange events, then it would be expected that roughly 50% of the events would have a fast proton with more momentum than the antiproton.

This would happen because, to a good approximation, there is no preferential forward/backward orientation for the $\bar{p}p$ decay in its rest frame. Thus half the

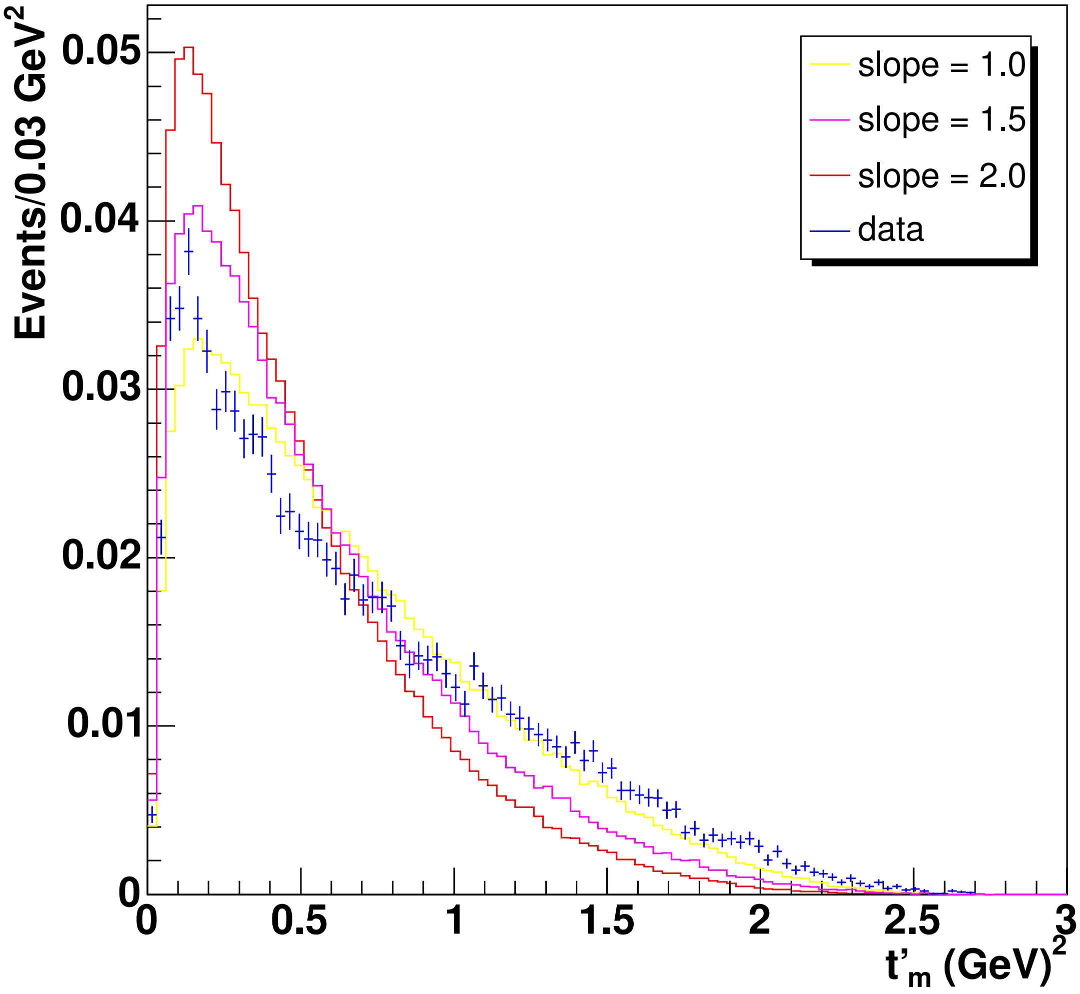

Figure 7.4. The t'_m distributions of MC events generated with exponential weights with varying slopes compared to the data(blue). The higher slope MC set fits the data best at low t'_m, whereas the low slope MC fits the data best at high t'_m. It was observed that the data could not be explained by a simple exponential weighting.

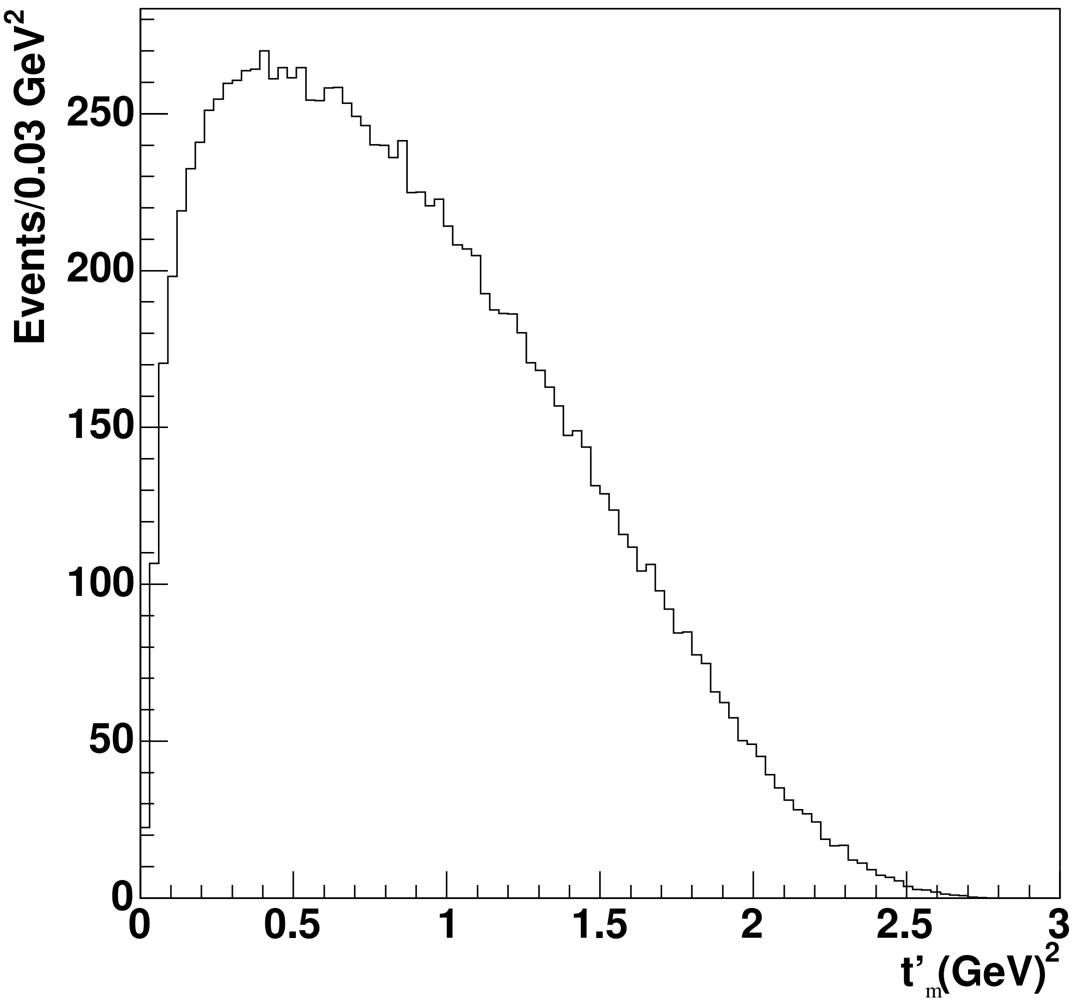

Figure 7.5. The t'_m distribution for MC events generated without t'_m dependence to show the effects of phase space and acceptance. At very low t'_m acceptance plays a major role due to protons being lost in the beam line. As t'_m increases, phase space effects become much stronger.

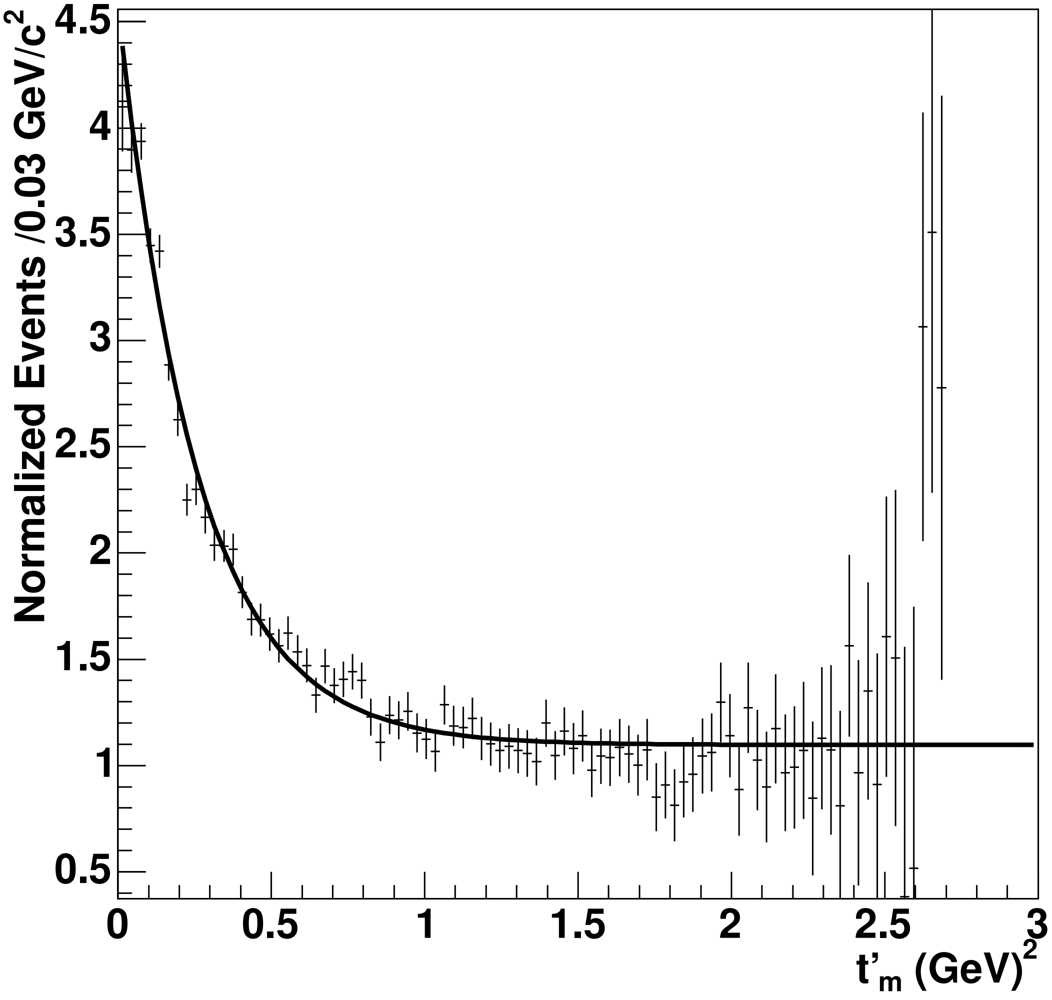

Figure 7.6. The t'_m distribution from the data after factoring out the effects of phase space and acceptance. The fit was done with an exponential plus a constant term. The result was an exponential slope of $b = 3.87(GeV)^{-2}$ with an error of $\sigma = 0.14(GeV)^{-2}$.

time the proton would be forward-going with respect to the beam direction. After boosting to the lab frame, a forward-going proton would then have more momentum than the antiproton. Taking acceptance into account, the fast protons may be lost in the beamline, thus this would act to decrease this percentage by some amount. Under baryon exchange, the proton at the photon vertex has a large amount of initial momentum, whereas the antiproton and the produced proton must share the remaining momentum available. Thus it is expected that nearly all baryon exchange events would have the fast proton having the most momentum. Under antibaryon exchange, the opposite occurs, therefore hardly any events would have a fast proton with more momentum than the antiproton.

The result from the data show that 67% of the events have a fast proton with more momentum than the antiproton. With perfect acceptance, this percentage would have been somewhat higher because of the effects of losing high momentum protons in the beam line. The result supports the conjecture that the data is dominated by meson exchange, but also contains some baryon exchange background.

7.5.5 Generating Three-Body Phase Space Events

Three-body phase space Monte Carlo events were generated in a similar fashion to two-body phase space. The main difference was that the CM angular distribution $cos(\theta_{CM})$ was chosen randomly on the range $[-1, 1]$. This weighting gives no preference to meson or baryon exchange production mechanisms. Three-body phase space events were also generated using a Bremsstrahlung beam energy distribution from the range 4.8-5.5 GeV. No mass dependence was placed on the $p\bar{p}$ resonance.

7.5.6 Fitting t^{meson} and t^{baryon} Simultaneously

While studies have shown that the observed $\gamma p \rightarrow pp\bar{p}$ data has a large contribution from meson exchange production, in order to understand the features of the data, other contributions to the production, such as baryon exchange, need to be included. A Monte Carlo study was performed to extract the contributions in the data from both t^{meson} and t^{baryon} production mechanisms. Monte Carlo events were weighted with t^{meson} and t^{baryon} distribution functions, $f(t_m) = e^{-bt_m}$ and $f(t_m) = e^{-at_b}$ respectively. The MC events were then fit to the data. The fit determined the two exponential slopes, and the t^{meson} to t^{baryon} mixing weight. This fit was performed by using three-body phase space MC events which were produced with a bremsstrahlung beam spectrum. This MC set was then used as an event bank to create subsets of two-body phase space MC events. A set of t^{meson}- and t^{baryon}-channel events were then selected by weighting the t^{meson} or t^{baryon} values according to the associated exponential slope. The two sets of data were then combined using a mixing weight. The t^{meson} and t^{baryon} distributions were compared to the data. A χ^2 was calculated by obtaining a χ^2 for both the t^{meson} distributions and for the t^{baryon} distributions and then summing the two. For i running over the N bins, where the number of data events is defined as N_{data}, and the intensities are normalized such that the total area equals unity.

The χ^2 is defined by

$$\chi^2_t \equiv N_{data} \sum_i (I^i_{MC}(t) - I^i_{data}(t))^2 / I^i_{data}$$

$$\chi^2_u \equiv N_{data} \sum_i (I^i_{MC}(u) - I^i_{data}(u))^2 / I^i_{data}$$

$$\chi^2_{TOT} = \chi^2_t + \chi^2_u$$

The fit parameters were then obtained by minimizing the χ^2. Note that each time the χ^2 is calculated, a new set of MC events are chosen from the bank. The χ^2 as a function of the three parameters is shown in figure 7.7. For each parameter, the other two parameters were fixed while it was varied. The resulting t^{meson} and t^{baryon} distributions are shown in figure 7.8. This fit produces excellent agreement in the t^{meson} distribution and good agreement in the t^{baryon} distribution. The χ^2/NDF was

441/197=2.24, which indicates that the fit does a fair job, but does not completely describe the data. The large χ^2/NDF value stems from the disagreement in the t^{baryon} distribution. This double channel fit does a much better job of matching the momentum exchange distributions, compared to those of the previous fit using single channel two-body phase space events.

From the double channel fit results, the t^{meson}-channel slope is measured to be $b = 3.0(GeV)^{-2}$ and the t^{baryon}-channel slope was $a = 0.9(GeV)^{-2}$. The weighting is measured to be 74% t^{meson}-channel to 26% t^{baryon}-channel events. The resulting particle momenta, invariant mass, and angular distributions are shown in figures 7.9, 7.10, and 7.11 respectively. The particle momenta distributions were improved dramatically from that of the meson exchange MC. Too often in the single channel simulations, the antiproton had a large momentum mismatch. In the invariant mass distributions, the double channel MC distribution is shifted slightly towards higher mass. Despite this, the overall shape is in good agreement with the data. No mass restrictions were placed on the Monte Carlo, thus these distributions are the direct result of the double channel phase space effects. The double channel MC angular distributions, shown in figure 7.11, are in excellent agreement with the data. This was not possible using single channel MC, as was shown in figure 7.2.

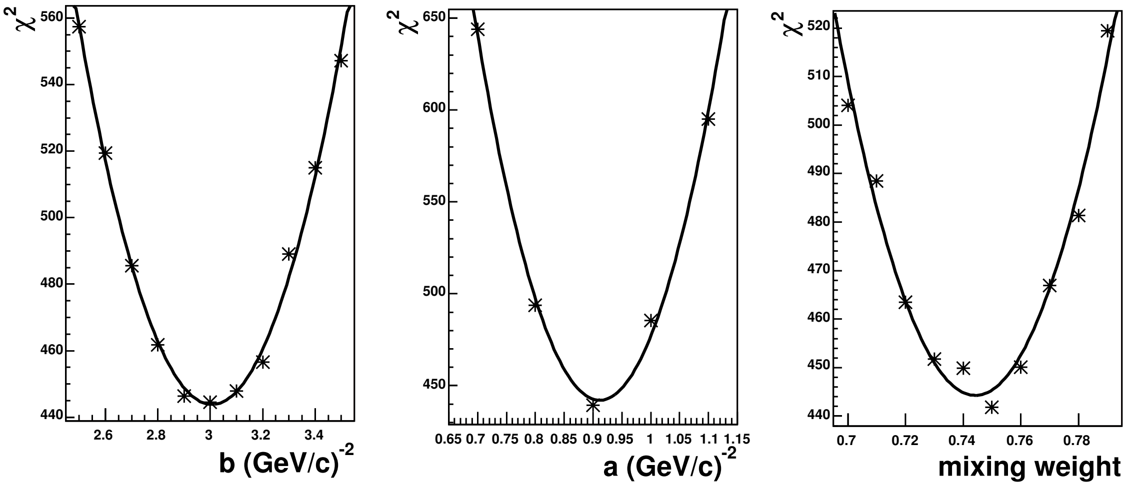

Figure 7.7. The χ^2 as a function of the fit parameters. b is the slope of the meson exchange exponential weighting function, t^{baryon} is the slope of the baryon exchange exponential weighting function, and the mixing weight is the ratio of t^{meson}-channel events. The fit results were $b = 3.0(GeV/c)^{-2}$, $a = 0.9(GeV/c)^{-2}$, and $weight = 0.74$.

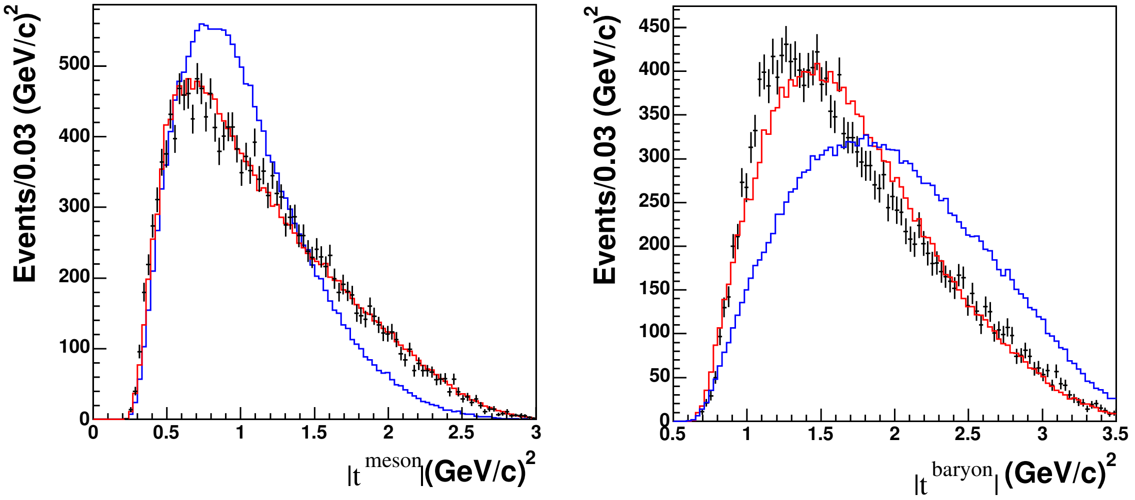

Figure 7.8. The results of fitting t^{meson} and t^{baryon} simultaneously. The black points are the data, the red line is the two-channel fit MC, and the blue line is the best meson exchange fit MC. The two-channel fit performs extremely well compared to the meson exchange fit.

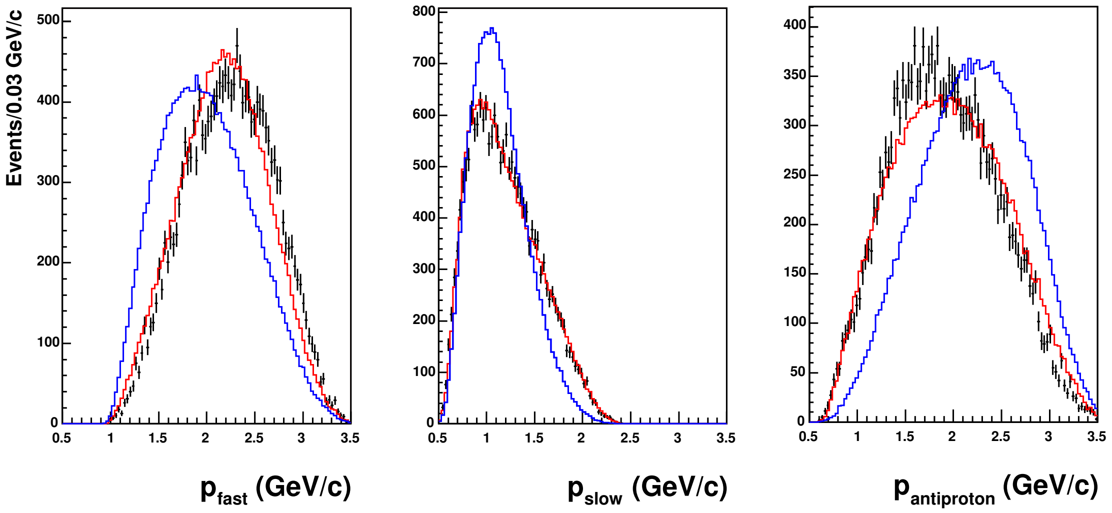

Figure 7.9. The resulting particle momentum distributions from two-channel MC (red) and meson exchange MC (blue) compared to the data(black). The two-channel fit performs extremely well compared to the meson exchange fit.

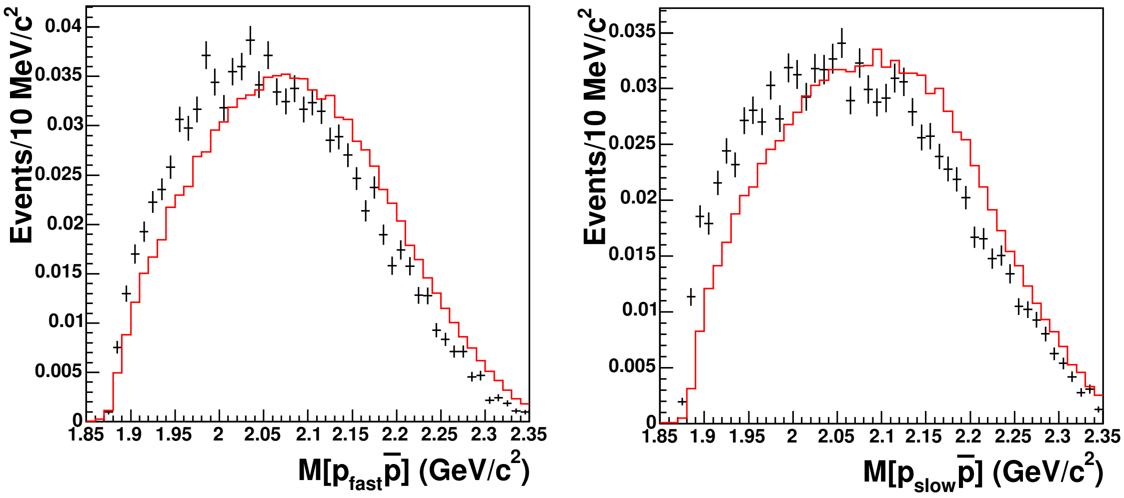

Figure 7.10. The resulting invariant mass distributions compared to the data(black). Despite the obvious shift, the result is astonishing since there are no restrictions to the mass in the generation of the MC.

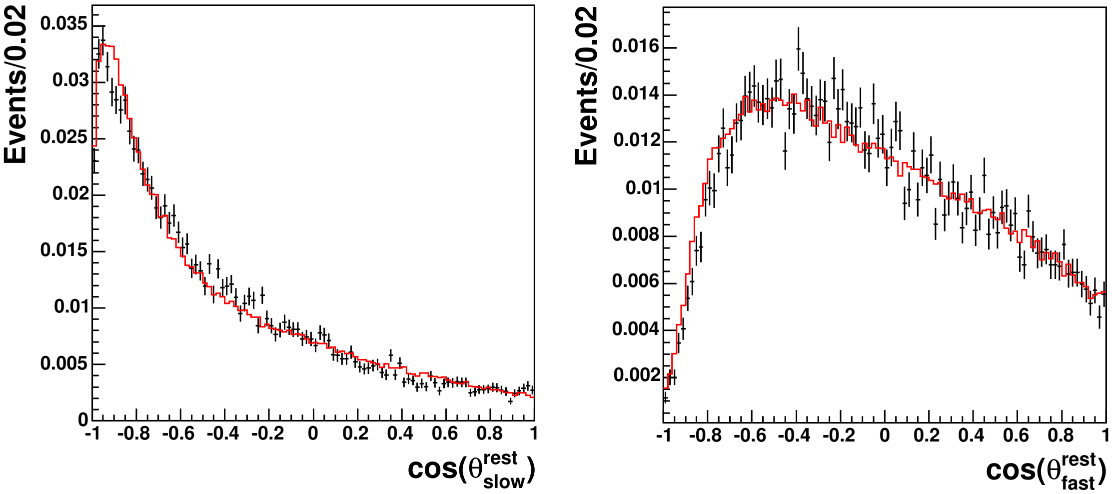

Figure 7.11. The resulting angular distribution in the X_{slow} and X_{fast} rest frames. There is excellent agreement between the data and the MC.

CHAPTER 8

CROSS SECTION MEASUREMENTS

A cross section is used to express the probability of a reaction to occur. The cross section for the reaction $\gamma p \rightarrow pp\bar{p}$ was measured for a photon energy of 4.8-5.5 GeV. The cross section can be used to determine how many events would be expected for a given number of photons interacting with a given number of protons. The cross section may also be used to compare the probability of this reaction to occur with that of other similar reactions.

8.1 Total Cross Section

The total cross section is found by

$$\sigma = \frac{N}{Sensitivity \times Acceptance} = \frac{N_{corrected}}{Sensitivity}.$$

The raw sensitivity is a measure of many events you would expect for a given cross section. It does not take into account detector acceptance or trigger efficiency. The raw sensitivity is defined as

$$S = \rho L N_A N_\gamma w$$

where ρ is the density of liquid hydrogen, L is the target length, N_A is Avogadro's number, N_γ is the total number of beam photons, and w is the molecular weight of hydrogen. The sensitivity for the E01-017 experiment was 2.767 events/pb.

The left plot in Figure 8.1 shows the photon flux as a function of energy. The right plot in the figure shows the photon flux corrected for background in the tagger. For a bremsstrahlung beam, the photon distribution is inversely proportional to the

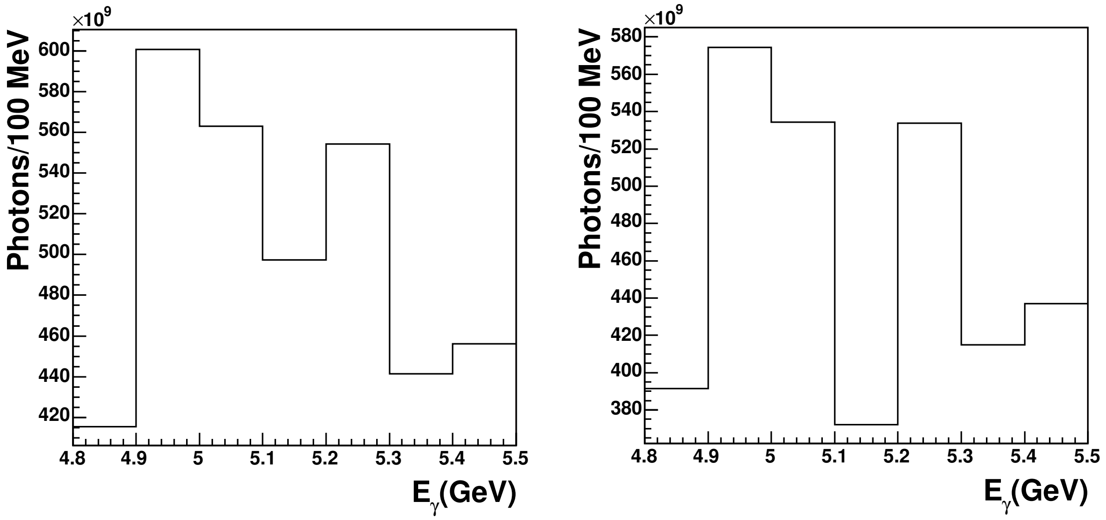

Figure 8.1. Left: The number of photons as a function of beam energy. For a bremsstrahlung beam, the number of photons is expected to decrease exponentially as the energy increases. Right: The number of photons corrected for background tagger hits. A large correction of 25% was made for the region 5.1-5.2 GeV.

photon energy. A large background of approximately 25% was found in the region 5.1-5.2 GeV. Evidence of this problem can be seen in Figure 6.1. A depletion of $p\bar{p}$ events occurs from 5.10 to 5.15 GeV. This indicates that the background is caused by good photons for which the timing information was inaccurate.

Using the corrected photon flux and the acceptance corrected data, the cross section as a function of energy was calculated. The results are shown in figure 8.2. The cross section starts at 27.3 ± 0.7 nb for $E_\gamma = 4.85 GeV$ and increases to 36.9 ± 0.7 nb at $E_\gamma = 5.45 GeV$. The average cross section over the range 4.8-5.5 GeV is 33 ± 2 nb.

8.2 Acceptance Correction

Three-body phase space events, generated with a bremsstrahlung beam spectrum, were used to correct the data for acceptance. The acceptance is estimated by taking the ratio of the E_{beam} versus t'_m distribution of the accepted events to that

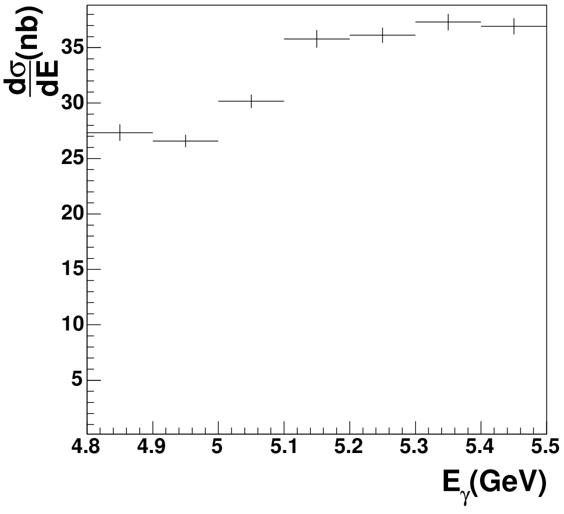

Figure 8.2. The cross section as a function of energy in nanobarns.

of the raw generated events. As the energy increases, more breakup momentum becomes available to the particles, which increases the likeliness of being detected by CLAS. Low momentum protons can bend out of CLAS, and $p\bar{p}$ pairs with small breakup momentum, which occurs more often at lower photon energies, suffer track reconstruction inefficiencies. The CLAS acceptance is dependent on t'_m because events with small exchange four-momentum are more likely to have particles go undetected in the beam line. The left side of Figure 8.3 shows the E_{beam} versus t'_m acceptance distribution. The right side of the figure shows the corrected E_{beam} versus t'_m distribution for the experimental data. The acceptance is mostly smooth except for a sharp drop at low t'_m. This is due to the large loss of particles in the beam line for events with low t'_m. On average, the acceptance is 23%.

8.3 Yield Corrections

Several corrections must be made to the overall yield to properly account for acceptance issues which are not determined through Monte Carlo simulations. For 12% of events from experiment E01-017, there are multiple tagged photons which

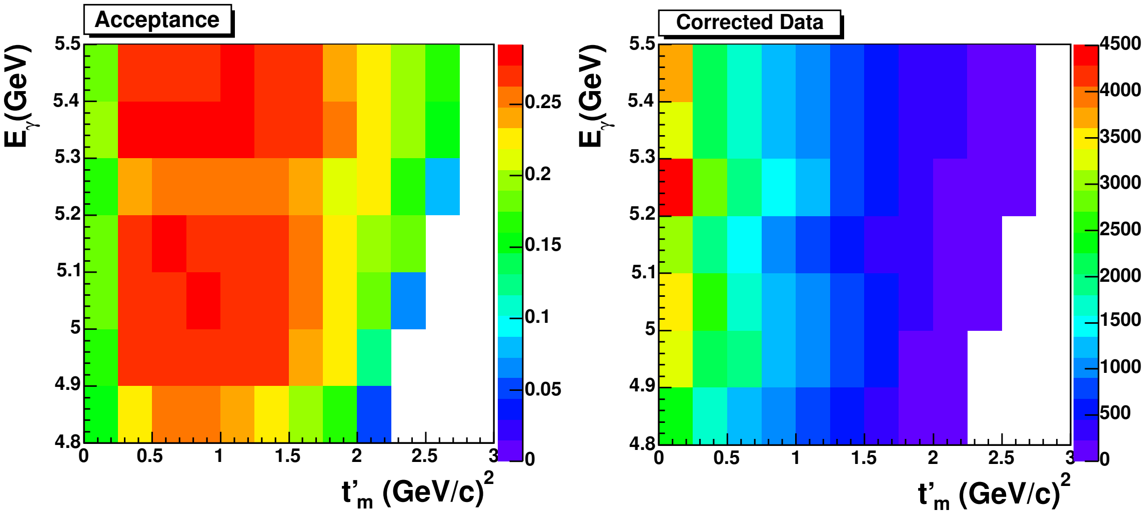

Figure 8.3. Left: The E_{beam} versus t'_m acceptance distribution measured from Monte Carlo simulations. The average overall acceptance is roughly of 23%. The acceptance decreases rapidly near low t'_m. Right: The corrected E_{beam} versus t'_m distribution for the experimental data. The increased phase space by increasing the beam energy can be seen by the increasing range of t'_m as the energy increases.

have the proper vertex time to have caused the event. During data selection, an event with multiple good photons, was assigned one of the photons randomly. In some cases, the multiple photons were actually a single photon whose electron generated two hits in the tagger. Multiple photons are taken into account by ignoring hits in which the photons had an energy within 0.1 GeV. This reduced the multiple photon events to 7% of the data set. Since the photons are chosen randomly, the wrong photon will be chosen half the time. Thus the yield must increased by a factor of 3.5%.

Due to the start counter resolution, some good events were lost due to timing requirements. The vertex time for the photon was required to match the vertex time determined by the start counter. To determine how many good events were lost, the timing requirements were removed to check the increase in signal events. The increased signal was measured by fitting the missing mass squared distribution to a Gaussian plus a linear background term. By removing the timing requirements and checking the missing mass squared distribution, the increase in the yield was measured to be 3.4%.

It was found that a large number of background photons were reported by the tagger. This was seen by comparing the vertex time from the tagger to the accelerator photon time, as shown in Figure 8.4. In the figure, a near Gaussian signal distribution sits on top of a flat background. This background was checked for varying photon energies from 4.8-5.5 GeV. Due to the nonlinearity of the timing resolution, the distributions were fit to double Gaussian distributions plus a flat background. For most of the energy range, the background represented about 5% of the tagged photons. For the energy range 5.1-5.2 GeV, the background was measured to be 24%.

The confidence level cut which was used to select antiprotons, removed some good events, as well as selecting some background events. The background events remaining in the data set and the number of good events lost from the confidence level cut were discussed in section 5.7. The yield requires an increase of 6.8% due to the good events lost by the confidence level cut. The yield requires a 6.6% reduction due to the background events which were accepted due to the confidence level cut.

8.4 Upper Limit on the 2.02 GeV/c^2 Resonance Production

The Feldman-Cousins method [48] was used to extract an upper limit on the production of a 2.02 GeV/c^2 resonance with a width of 27 MeV/c^2. This is the state reported by CERN in the reaction $\gamma p \rightarrow pp\bar{p}$ at 4.7-6.6 GeV. The Feldman-Cousins method is used to calculate a confidence interval for the cross section. The confidence interval is an estimated range of values which is likely to include the unknown cross section. A confidence level of 95% was used for the limits calculations. If the experiment was repeated several times, 95% of the confidence intervals would include the unknown cross section value. The benefit of using the Feldman-Cousins method is

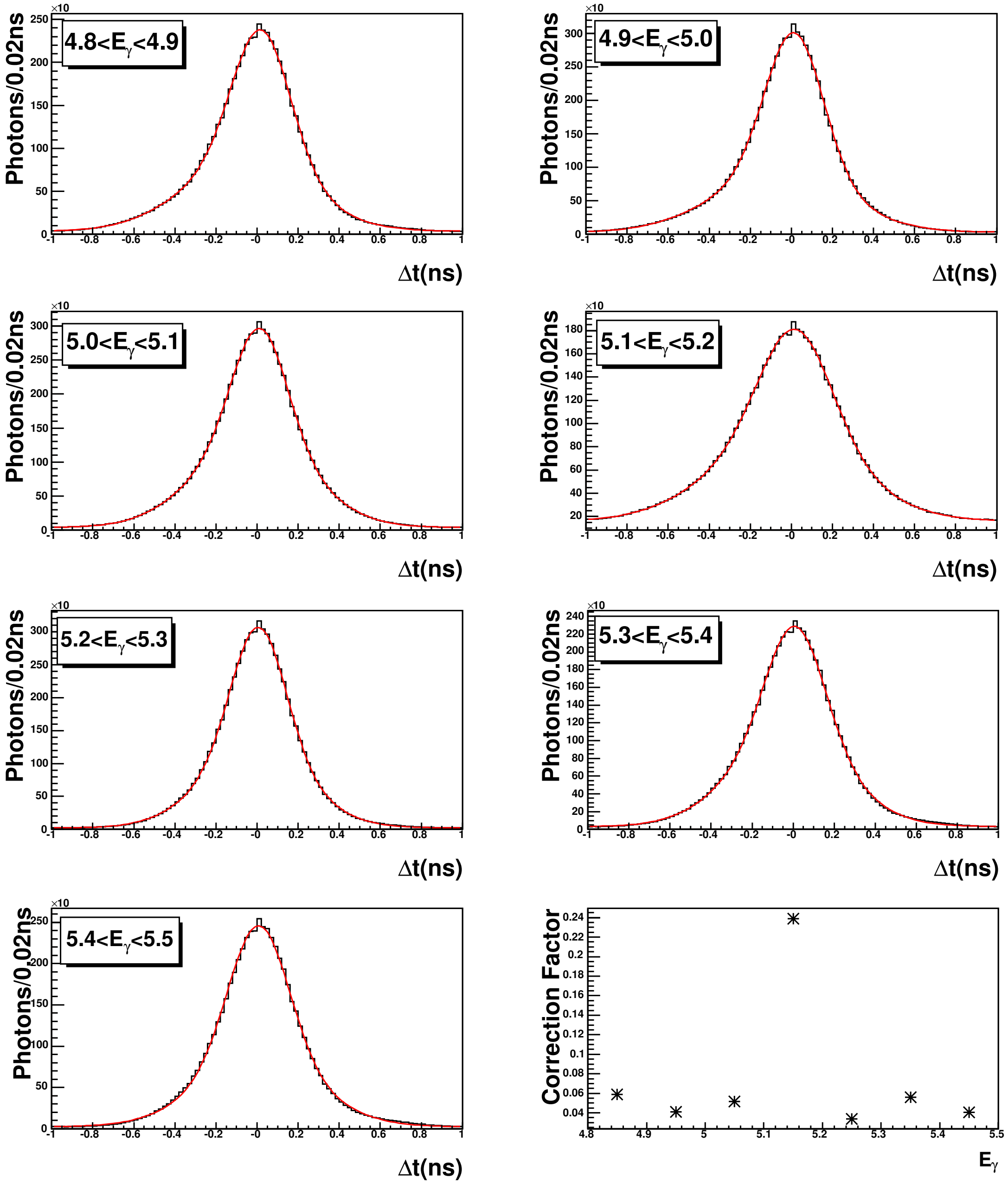

Figure 8.4. The distributions show the tagged photon time versus the accelerator photon time for several photon energy ranges. A small background of out-of-time photons were found, which is obvious for the photon energy range 5.1-5.2 GeV. The bottom right-hand plot shows the correction factors for the photon flux.

that it removes the bias of the experimentalist. Normally the experimentalist decides whether the data indicate a signal or the absence of one. For a signal, a confidence interval is calculated to determine the statistical significance of the signal. In the case there is no signal, an upper limit is calculated. The Feldman-Cousins method merges these choices so that an upper and lower limit smoothly shifts into an interval for a signal as that signal becomes more statistically significant.

For the $p_{fast}\bar{p}$ and $p_{slow}\bar{p}$ systems, a sixth order polynomial was fit to the invariant mass over the range 1.9-2.1 GeV/c^2. The mass was then scanned in 2 MeV/c^2 steps. For each step, the total number of events within 2σ ($\sigma = 20MeV/c^2$) were counted as the signal, and the fit was integrated within the same range to obtain the estimated background. An example showing how the signal and background events are obtained is shown in Figure 8.5. In the figure, the signal is all of the events from 2.00 to 2.04 GeV/c^2. The curve is a sixth-order polynomial fit to the mass range 1.900-2.100 GeV/c^2. The background is the integral of the curve from 2.00 to 2.04 GeV/c^2. The upper limit for mass value in the example is 80 events.

For this procedure, a 95% confidence level was used. The extracted upper limit yields are shown in in Figure 8.6. The left hand plots in the figure show the upper limit at each 2 MeV/c^2 mass value. The right hand plots show the background curves fit with sixth-order polynomials. The highest upper limit value occurs at 2.038 GeV/c^2 with a value of 196 events. Using the total number of events and the total cross section, the upper limit corresponds to a resonance cross section of 0.35 nb.

$$\sigma(\gamma p \to pX(2020), X \to p\bar{p}) < \tfrac{196\times\sigma_T}{18419} = 0.35nb$$

This contradicts the claim by Bodenkamp *et. al.* of a 2.02 GeV/c^2 resonance with a cross section of 14 ± 5 nb for the reaction $\gamma p \to pp\bar{p}$ with a beam energy of 4.7-6.6 GeV.

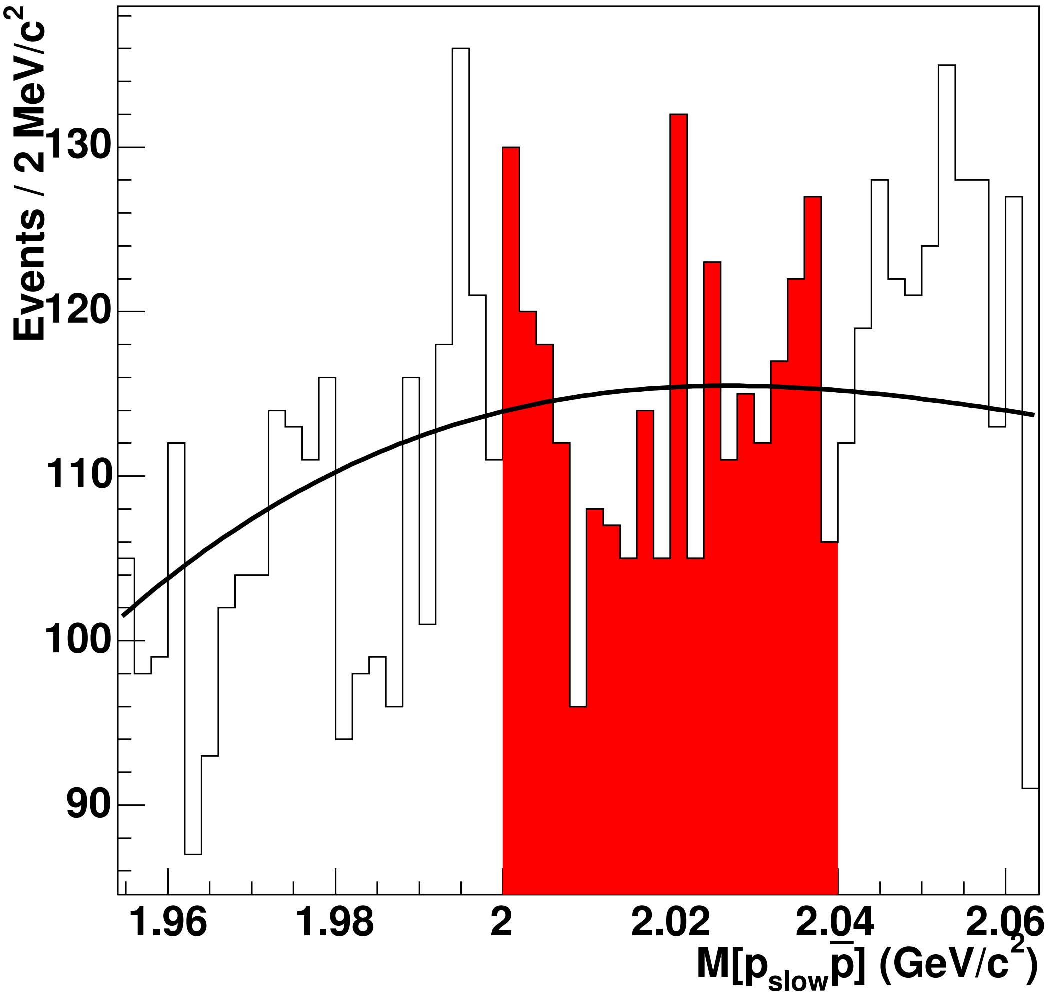

Figure 8.5. In this example of an upper limit calculation, the red region shows the events used as the signal for the mass of 2.020 GeV/c^2. The curve, which was fit to the mass range 1.900-2.100 GeV/c^2, is then integrated on the same range to estimate the background. The signal and background events are then used to calculate an upper limit for the resonance signal. The upper limit at the mass value shown was 80 events.

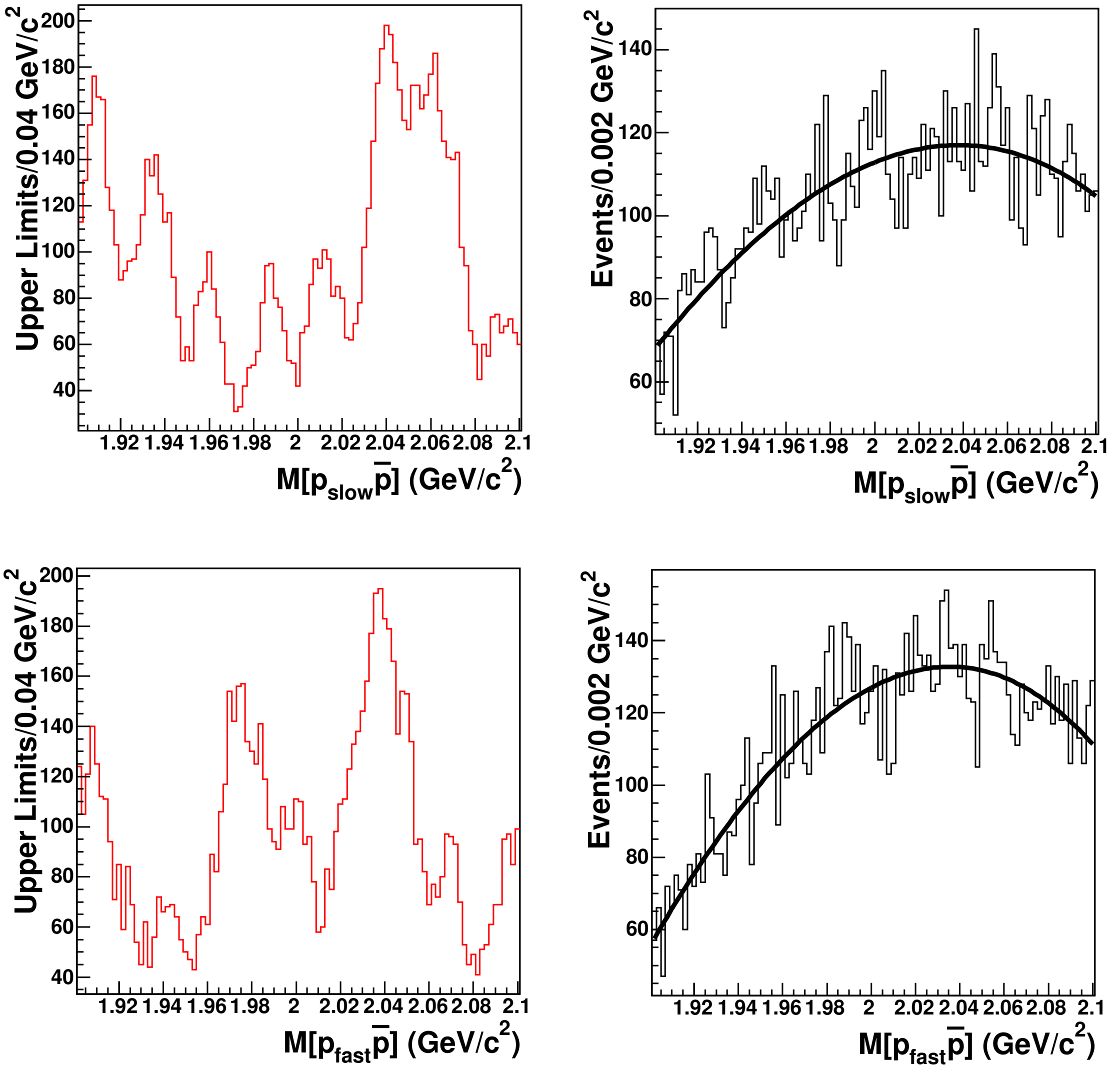

Figure 8.6. The figure on the right shows the background fit over the invariant mass distribution. The upper limit is calculated in 2 MeV/c^2 steps using all events within 20 MeV/c^2 of the mass. The number of background events for that range is calculated from the fit. The figure on the left shows the upper limit at each 2 MeV/c^2 step.

CHAPTER 9

MOMENTS ANALYSIS

One of the primary goals in the search for resonant states, in addition to the mass and width measurements, is the determination of a system's spin-parity through the study of the decay angular distributions.

In general, the angular intensity distributions are parametrized in terms of variables which can be directly interpreted or mapped to properties of the resonant states. In principle, any complete set of functions which span the appropriate space can be used. For example, Partial Wave Amplitude(PWA) analysis uses an expansion in terms of physical intermediate resonances[53]. While PWA allows for a more direct interpretation of results, in many cases the physical results suffer from ambiguities. That is, in some cases there can be several combinations of partial waves which describe the observed angular distributions.

A more mathematical approach uses an expansion in terms of moments, or averages of angular distributions. While moments are physically observed quantities, a moments analysis requires a complicated mapping from moments to physical states. Nevertheless, a moments analysis can provide an easy first-hand look at the existence of, or lack of, resonant spin-parity states.

9.1 Angular Moments

There exist many legitimate choices of weighting functions for an angular moments analysis. Using the spin formalisms developed by Chung [49], the angular moments were defined as the averages of the Wigner-D functions,

$$H(L,M) = \langle D^L_{M,0}(\phi,\theta,0)\rangle$$

where the angles were taken as the antiproton decay angle in the $\bar{p}p$ rest frame. These moments are in general, a product of two terms; one which contains information on how the resonance was produced, and another which contains information on how the resonance decays.

Figures 9.1, 9.2, 9.3, and 9.4 show the first several moments. Note that the moments are not corrected for acceptance. Structures are seen in the H(1,0), H(2,0), and H(2,1) terms. If the events were isotropic with perfect acceptance, then all of the moments, except the zeroth term, would have been consistent with zero. If the moments differ greatly from the Monte Carlo, it would normally be associated with structures in the decay angular distributions.

To isolate the structures seen in the data from normal isotropic behavior and acceptance, the experimental moments were compared to isotropic Monte Carlo. Initially, the moments were compared to accepted Monte Carlo events generated using only a single channel meson exchange production. The moments for raw MC events were calculated to verify that the moments were consistent with zero as shown in Figure 9.5. Using the raw events, the effects of mislabeling the protons could also be determined. In this MC sample, the protons were mislabeled in only 5% of the events. Figure 9.6 shows the moments calculated for raw events in which the protons were selected by momentum. The results are not consistent with zero. This shows a large effect from a small mislabeling of the protons.

The two-channel Monte Carlo fit took proton misidentification into account. In single-channel MC events, the events are weighted using perfect proton identification. In the two-channel MC simulation, the events are weighted using events with protons identified by their momentum. This serves as a mechanism for generating the proper number of events with misidentified protons.

There is no method to measure the raw moments for two-channel MC events. This is because the events were weighted after acceptance was taken into account. However, it was still possible to compare the accepted moments to the data. Figures 9.7, 9.8, 9.9, and 9.10 show that the MC and the data agree well. Resonant behavior would be represented by deviations between the data and Monte Carlo moments. Because of the strong similarities between the data and MC, the moments indicate that there are no non-S-wave resonances evident. The similarities also indicate that the two-channel MC events describe the data well.

9.2 Symmetrized Moments Distributions

The symmetrized moments are simply the average of the Wigner-D functions for each proton multiplied together. For a full derivation of the symmetrized moments, refer to Appendix A. These moments must be plotted as a function of the mass of each $p\bar{p}$ system. The moments are shown in Figures 9.11 and 9.12. Many similarities with the MC are seen in Figures 9.13 and 9.14. Because no significant differences are apparent, the conclusion is that there were no non-S-wave resonance production in the data.

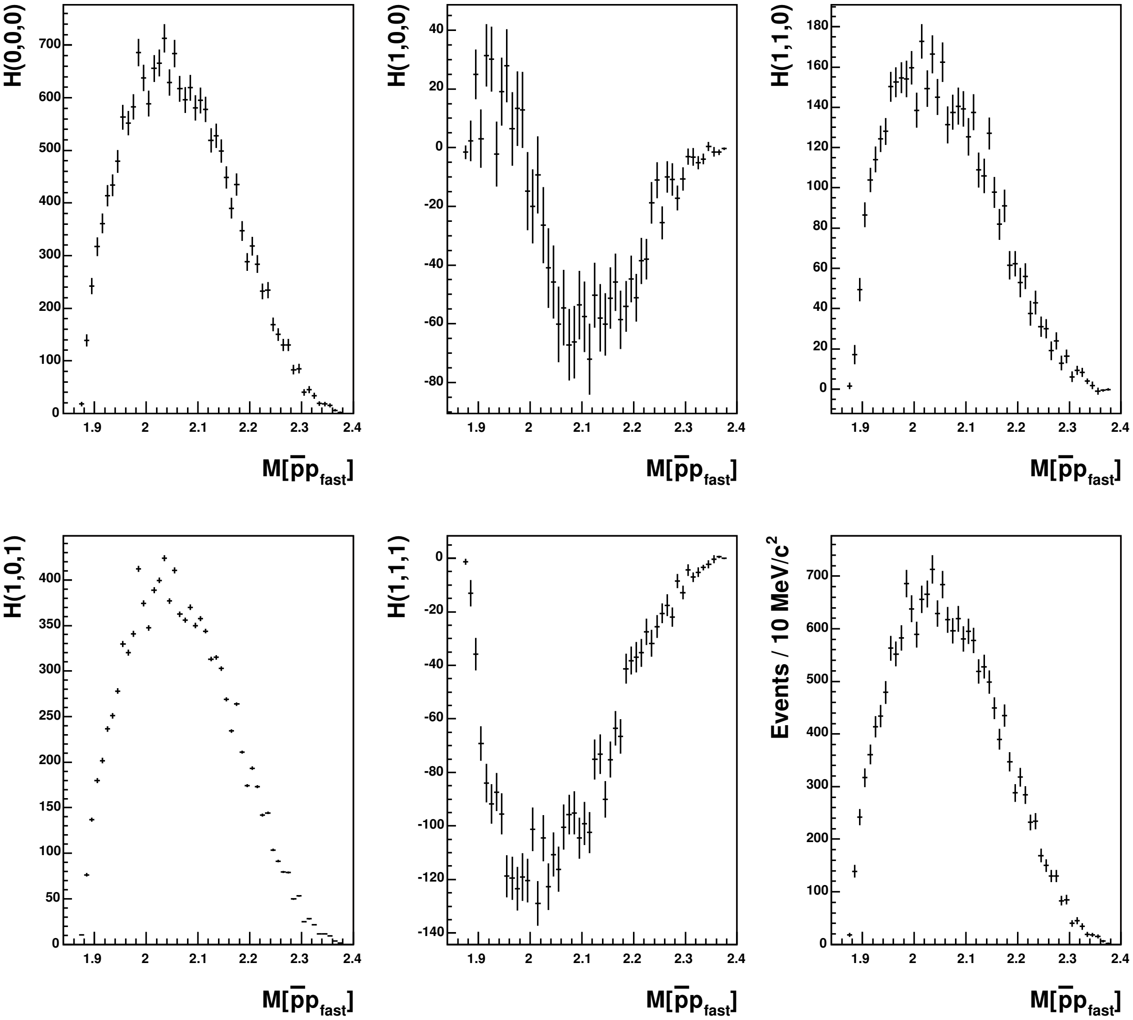

Figure 9.1. The data moments as a function of the $p_{fast}\bar{p}$ invariant mass. The moments are the averages of the Wigner-D functions using the $p\bar{p}$ rest frame angular distribution.

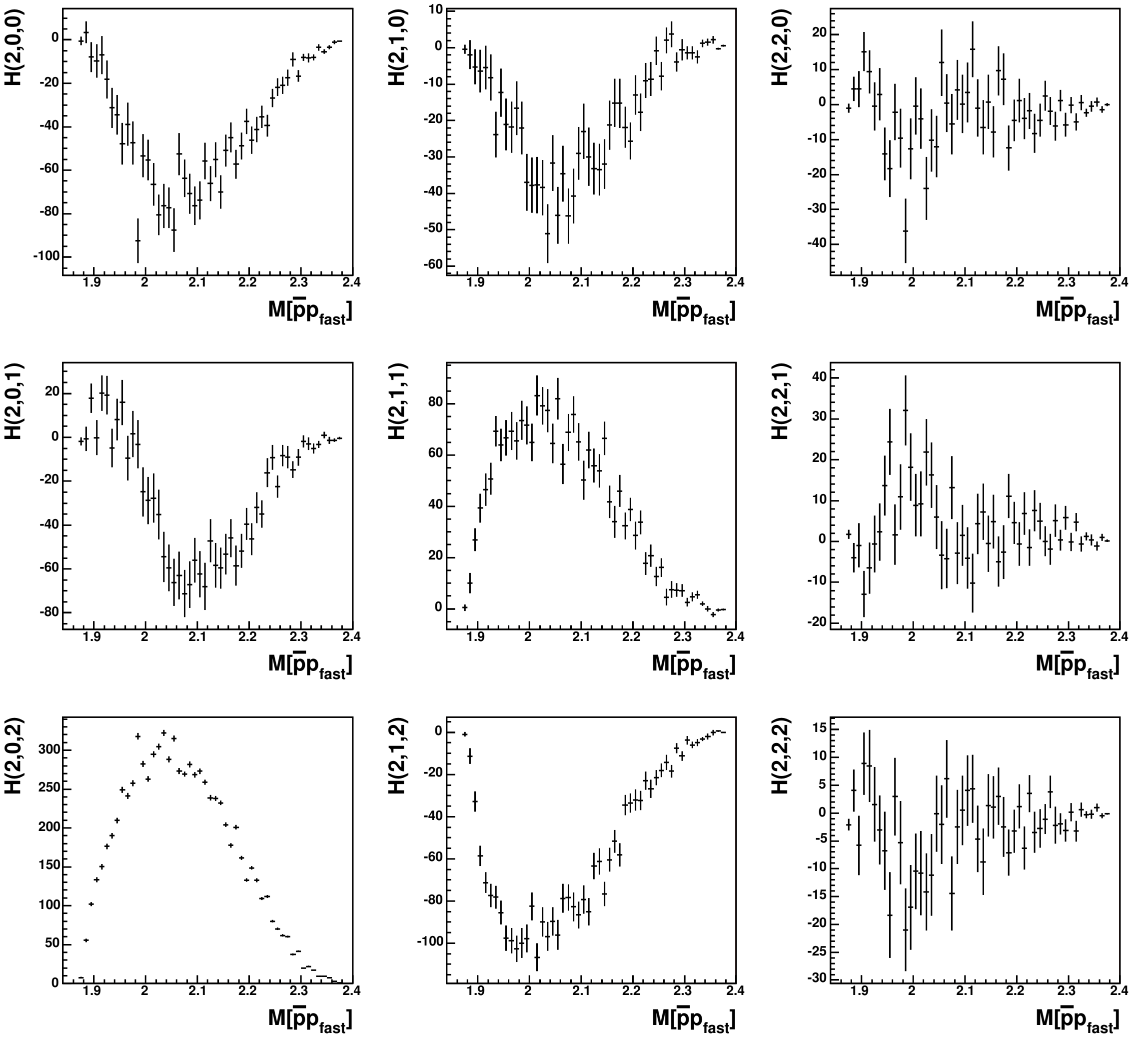

Figure 9.2. Higher order data moments as a function of the $p_{fast}\bar{p}$ invariant mass. The distributions have strong similarities to the moments for two-channel Monte Carlo simulations, shown in Figure 9.8.

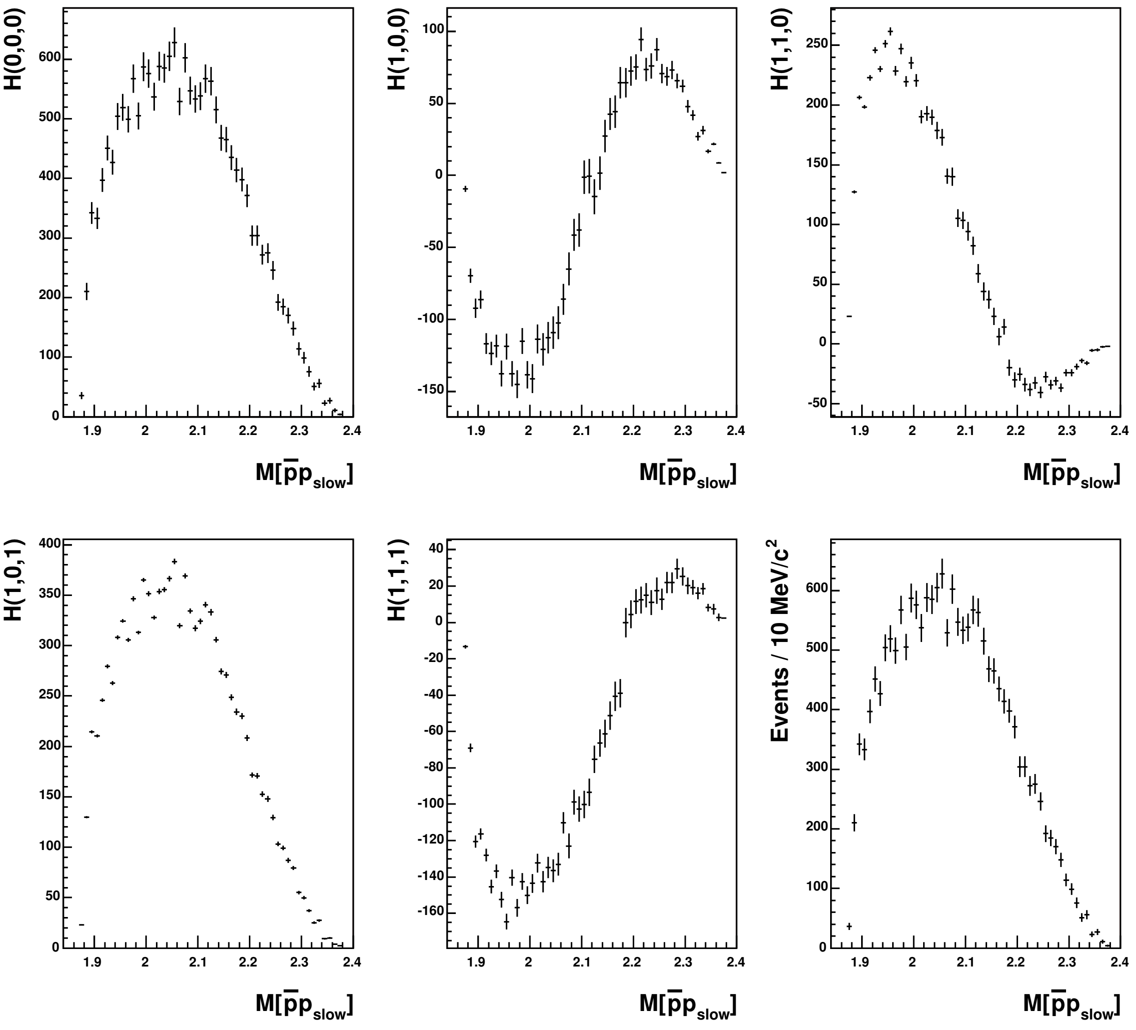

Figure 9.3. The data moments as a function of the $p_{slow}\bar{p}$ invariant mass. These distributions have strong similarities to those of the MC events shown in Figure 9.9.

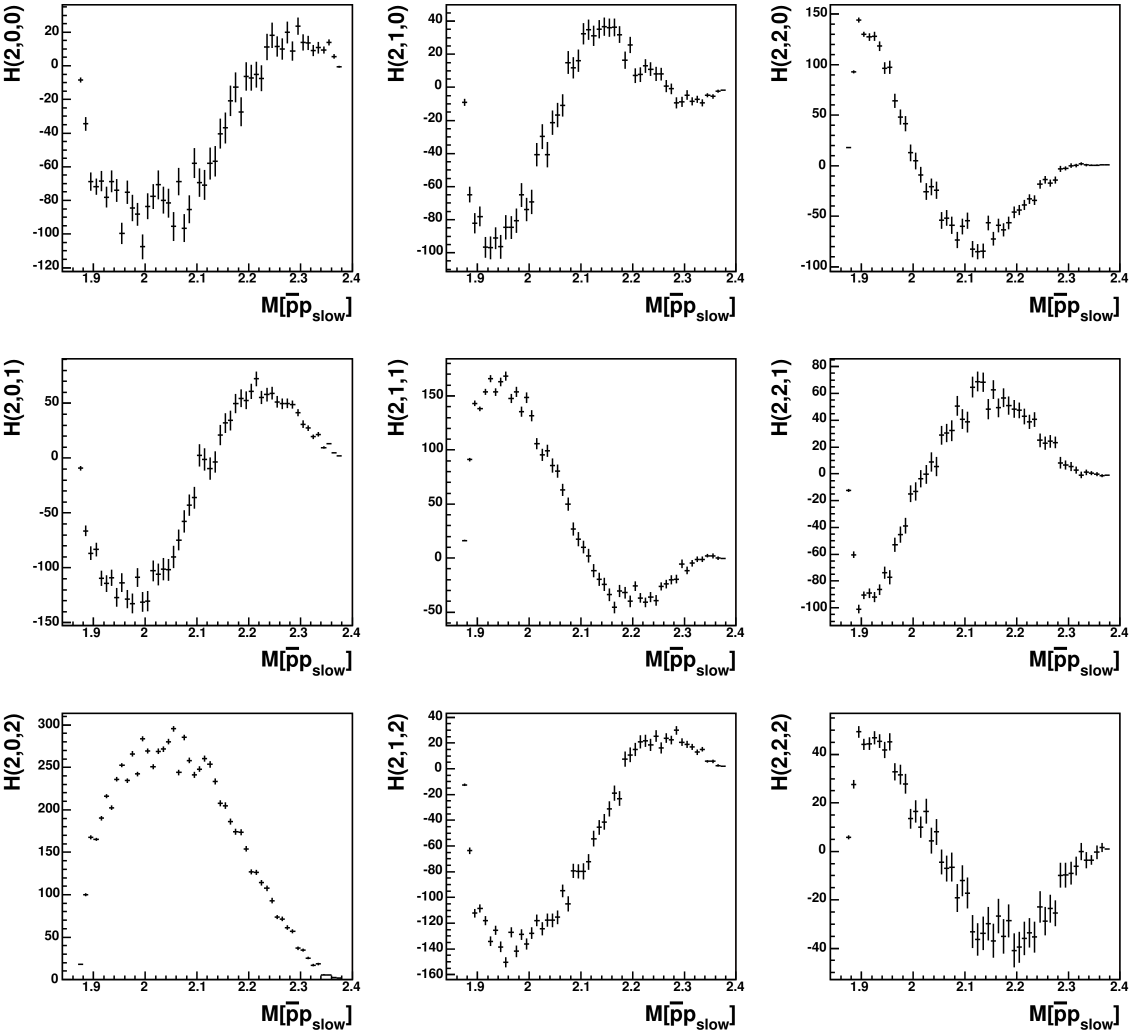

Figure 9.4. Higher order data moments as a function of the $p_{slow}\bar{p}$ invariant mass. Strong similarities are seen with the corresponding MC moments shown in Figure 9.10.

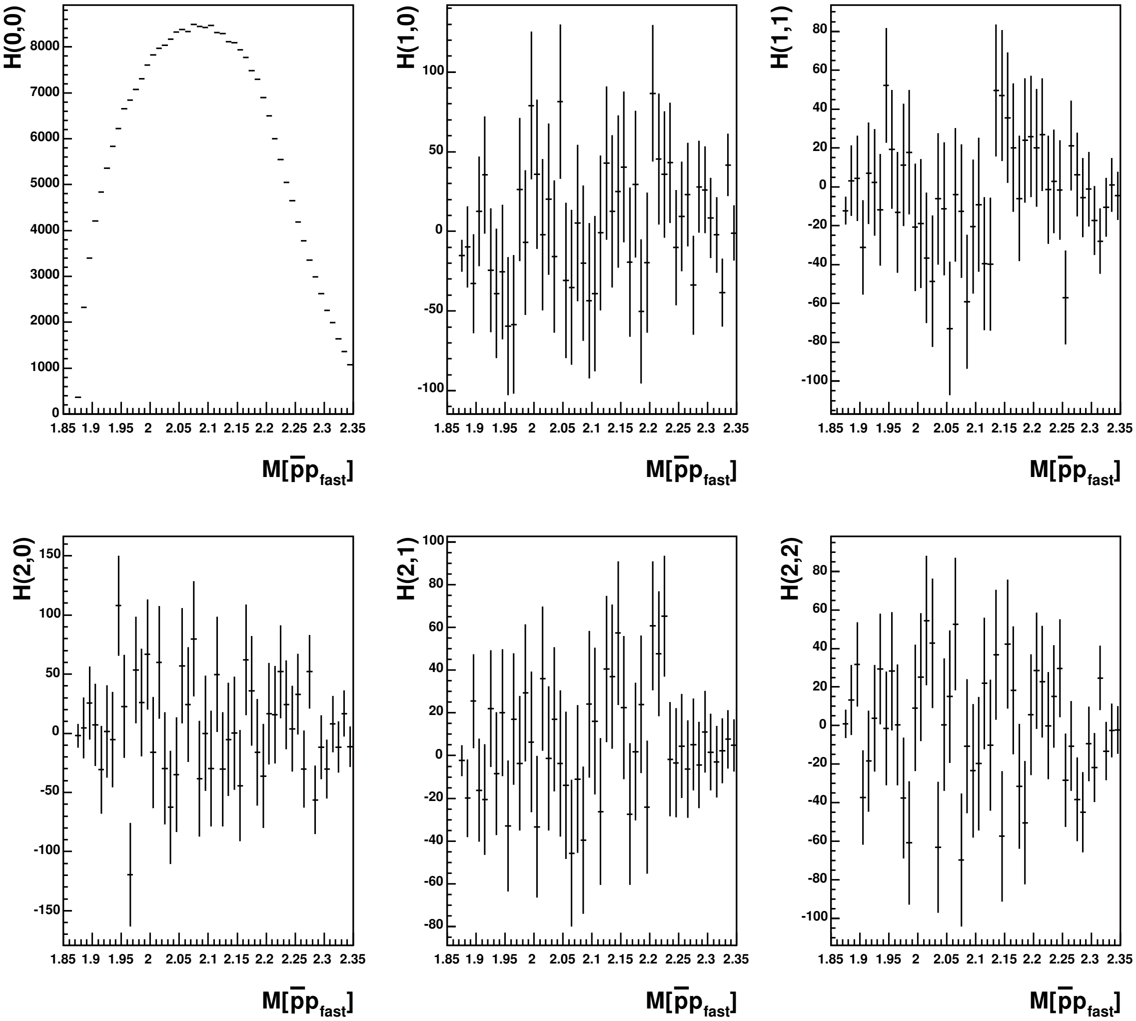

Figure 9.5. Raw moments of single channel meson exchange MC events. Each term, aside from the zeroth, is consistent with zero. These distributions match the expected moments for an isotropic phase space.

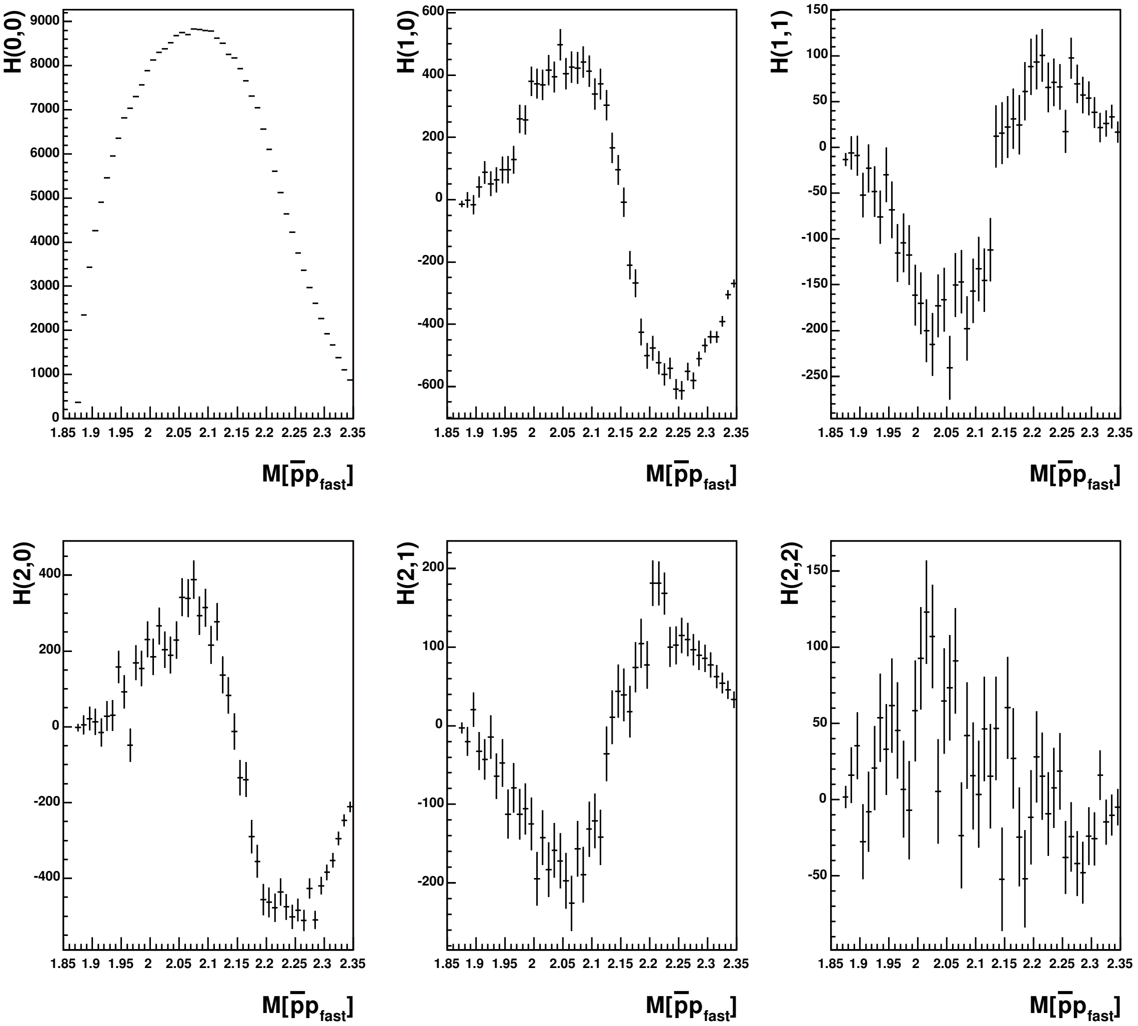

Figure 9.6. Raw MC moments in which the protons are labeled by momenta. The effects of mislabeling the protons are large, despite a misidentification of protons for only 5% of the events. Misidentifying the protons introduces structures into the moments. This effect greatly complicates the angular moments analysis.

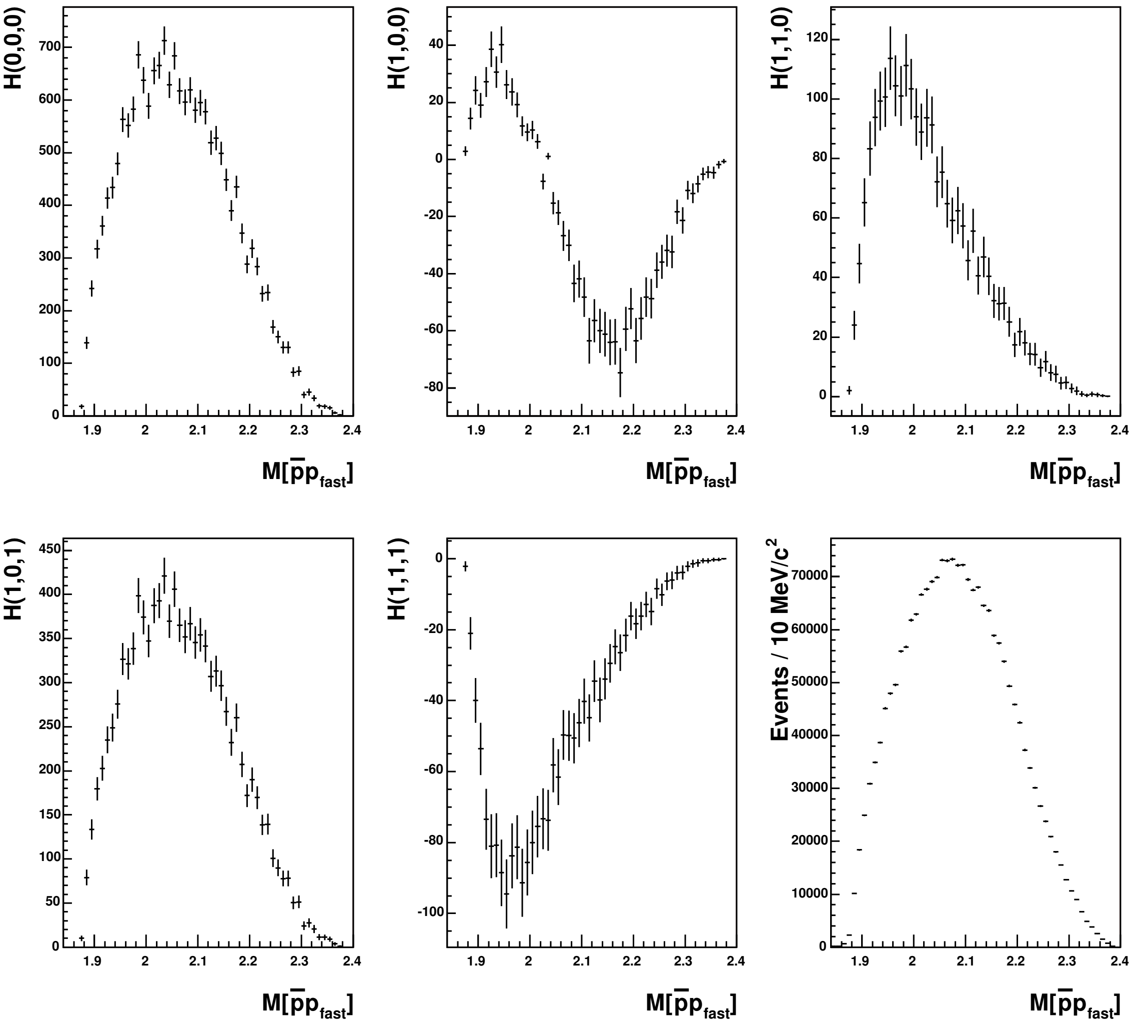

Figure 9.7. The MC moments as a function of the $p_{fast}\bar{p}$ invariant mass. These distributions are similar to those from the data(figure 9.1).

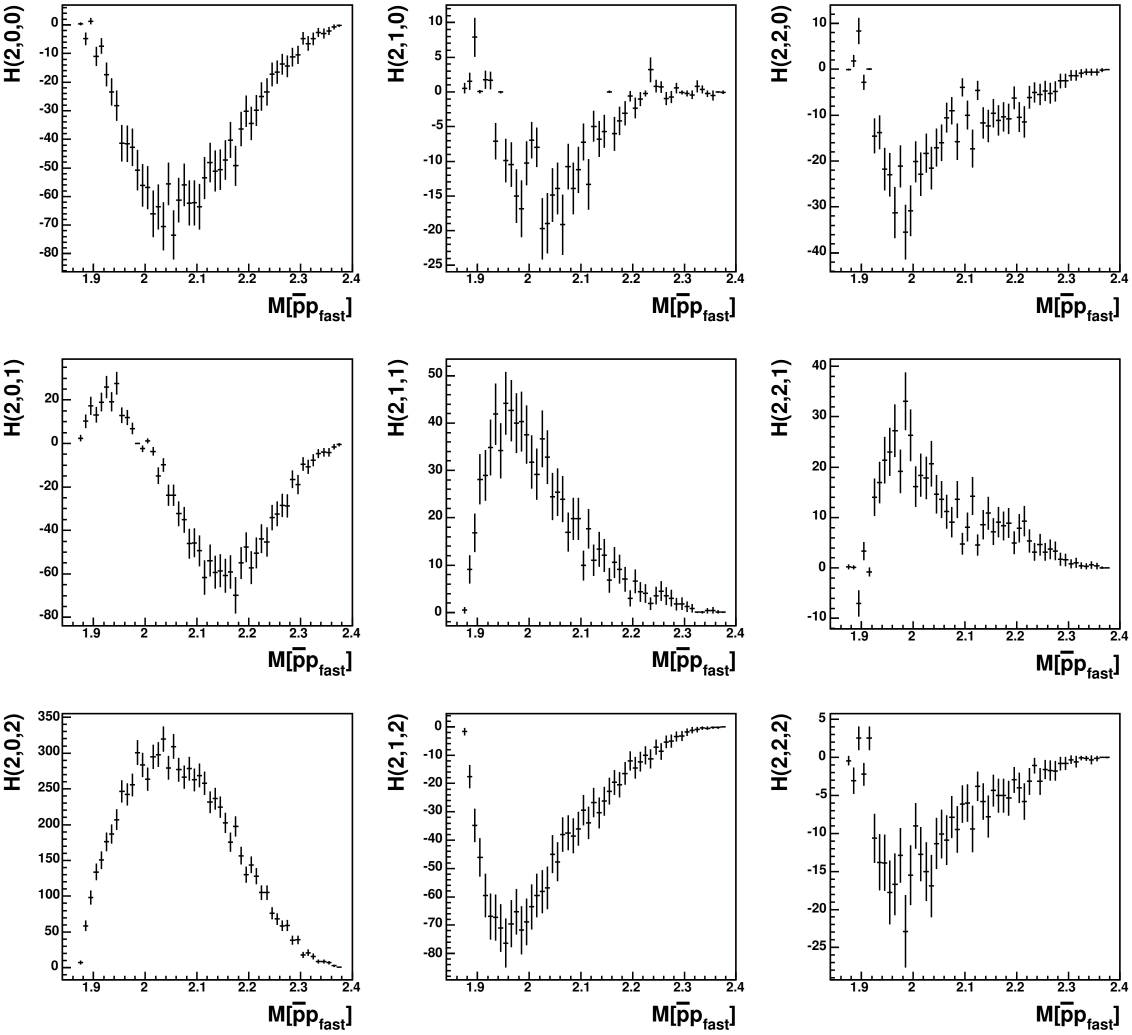

Figure 9.8. The MC moments as a function of the $p_{fast}\bar{p}$ invariant mass. These distributions are similar to those from the data(figure 9.2).

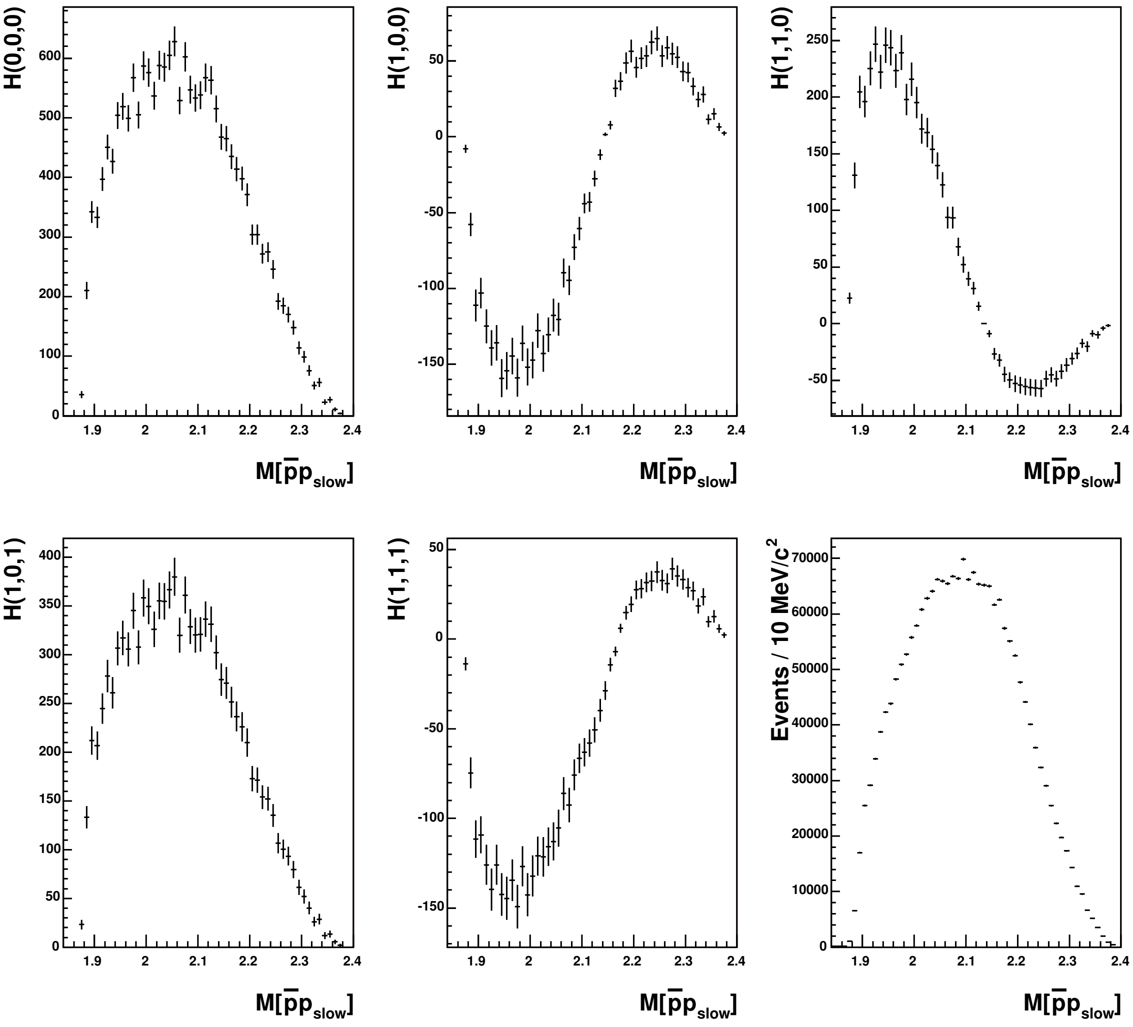

Figure 9.9. The MC moments as a function of the $p_{slow}\bar{p}$ invariant mass. These distributions are similar to those from the data(figure 9.3).

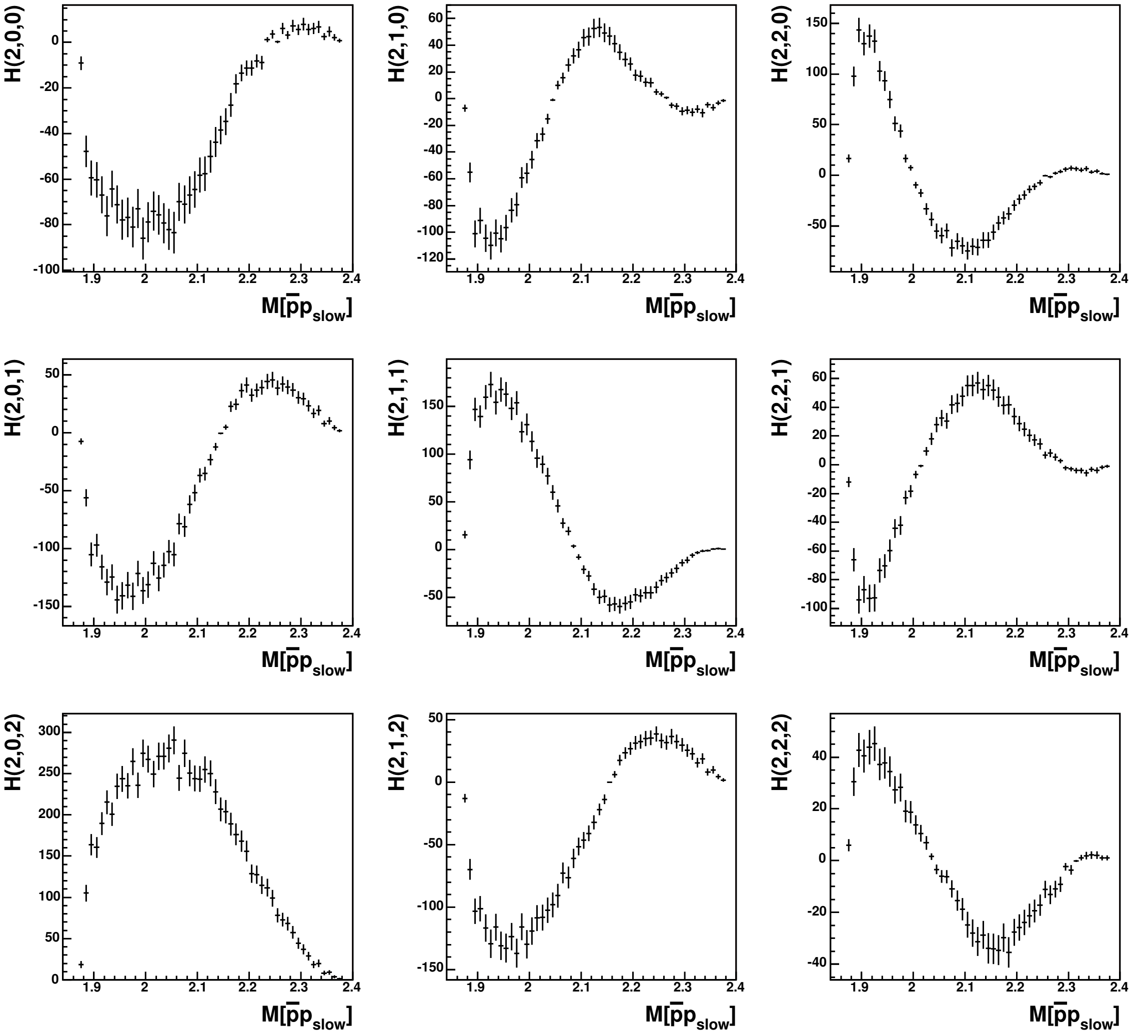

Figure 9.10. The MC moments as a function of the $p_{slow}\bar{p}$ invariant mass. These distributions are similar to those from the data(figure 9.4).

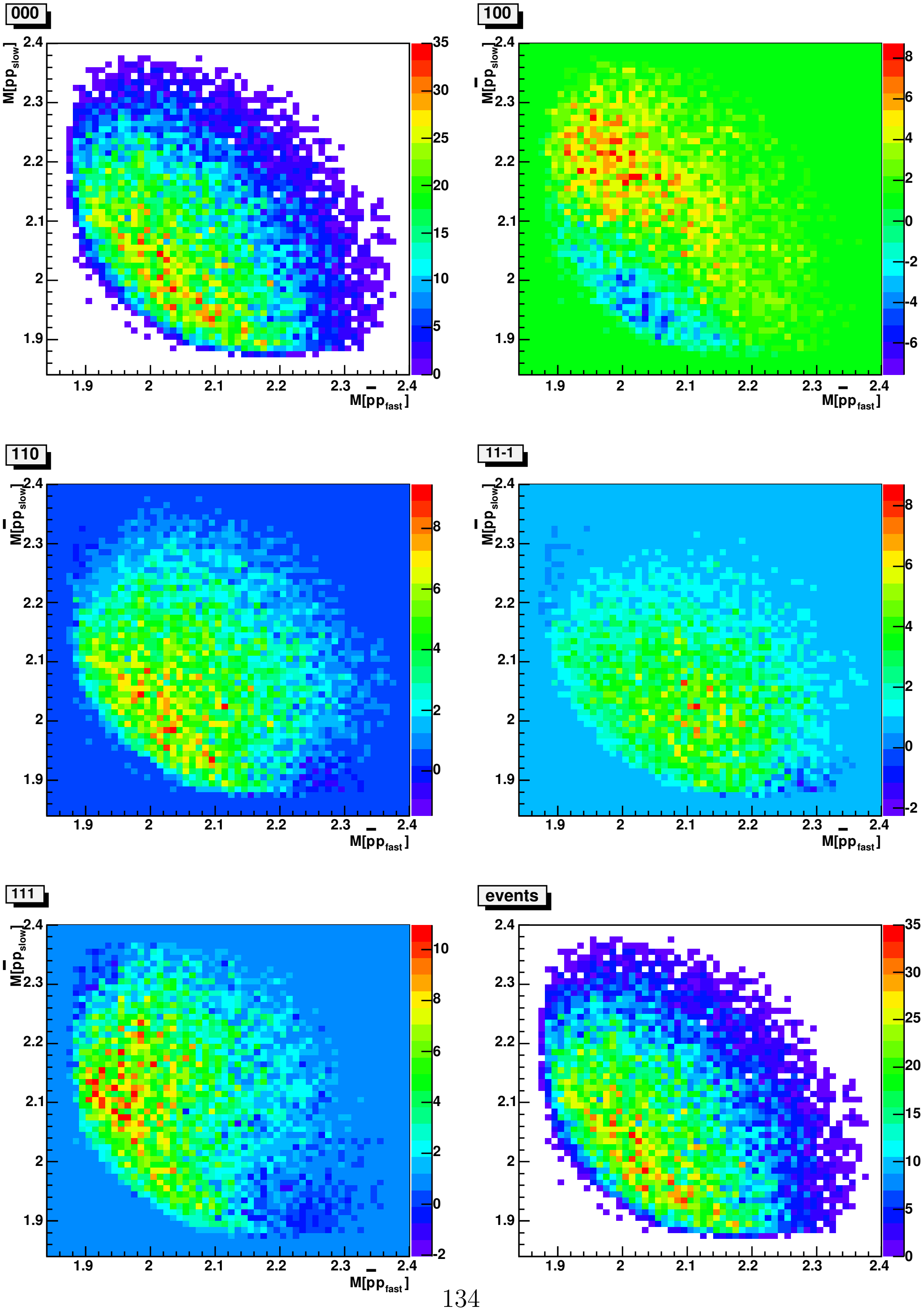

Figure 9.11. The two-dimensional symmetrized moments. The three digit indices represent which moment H(J,M,L) is calculated. The X-axis is the X_{fast} mass, while the Y-axis is the X_{slow} mass. The plot in the lower right-hand corner is simply the 2D invariant mass distribution.

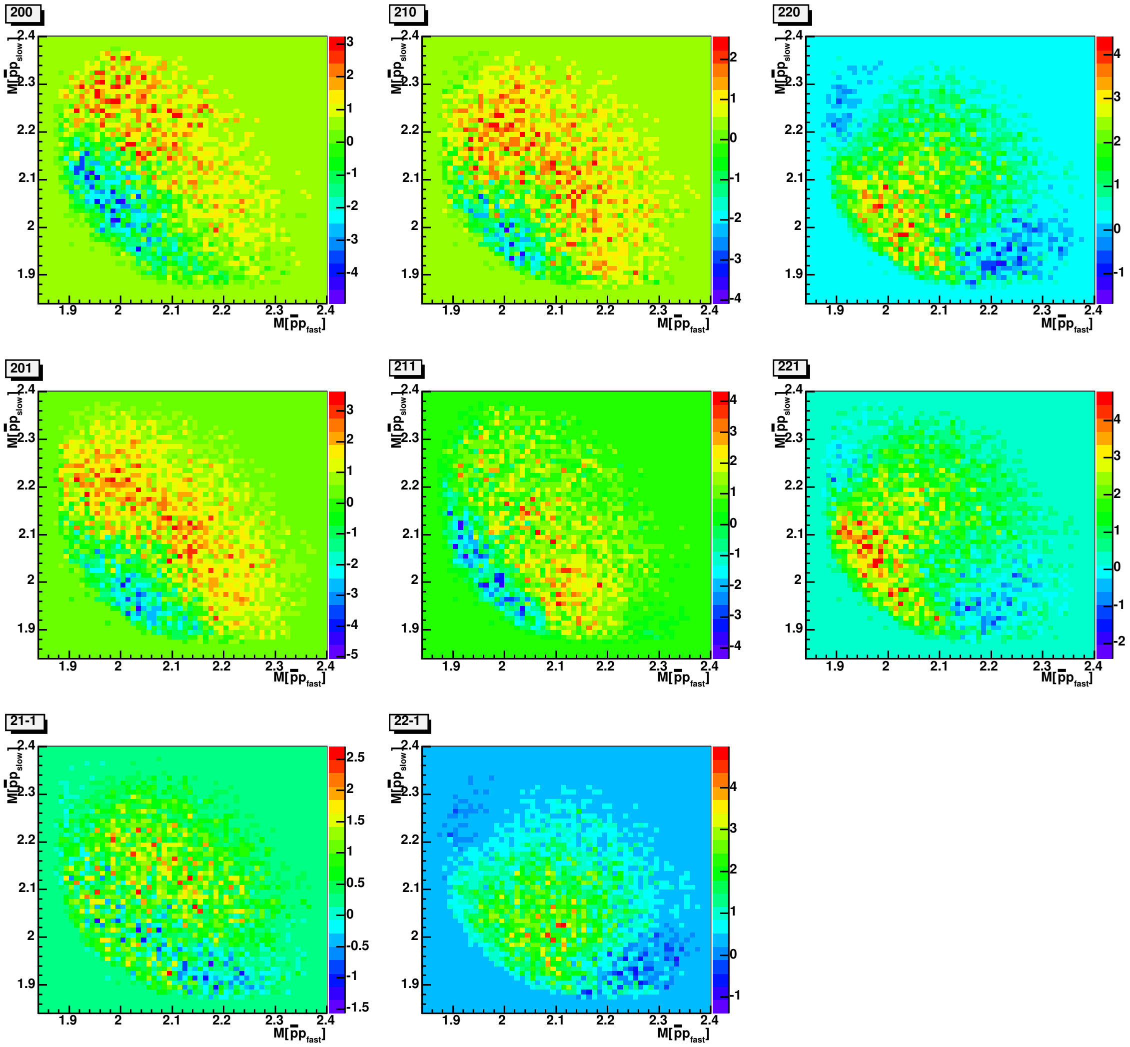

Figure 9.12. The higher order symmetrized moments for the data. Strong similarities are seen in the MC symmetrized moments shown in Figure 9.14.

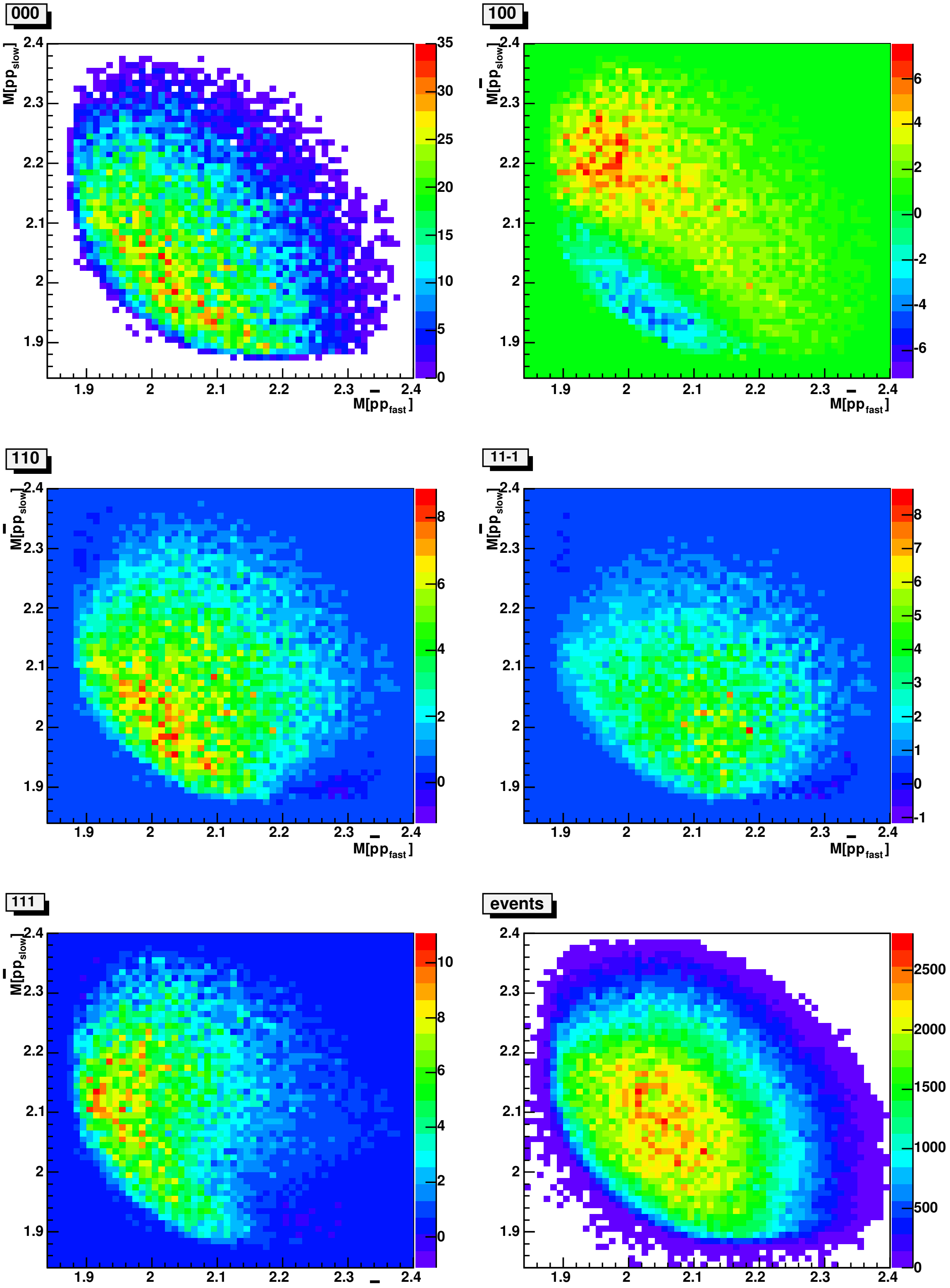

Figure 9.13. The two-dimensional symmetrized moments for accepted MC events. The bottom right-hand distribution shows the invariant mass distribution of the $p_{slow}\bar{p}$ system versus that of the $p_{fast}\bar{p}$ system. The MC moments were normalized to the data.

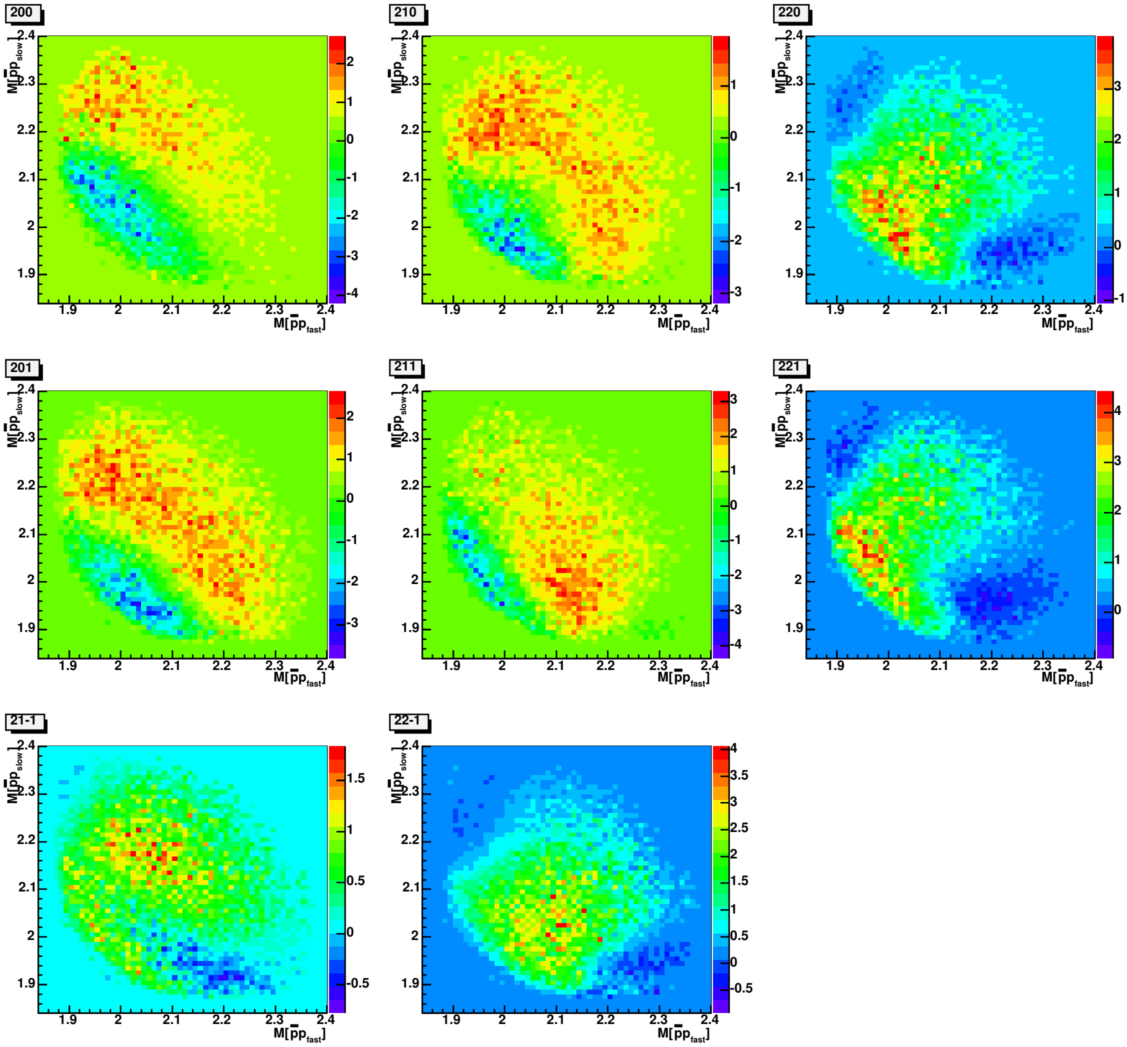

Figure 9.14. The higher order symmetrized moments for accepted MC events. Strong similarities seen in the data suggest that no non-S-wave resonant production contributes to the data.

CHAPTER 10

CONCLUSIONS

The reaction $\gamma p \to pp\bar{p}$ was analyzed from the CLAS experiment E01-017 at Jefferson National Lab for a photon energy in the lab of 4.8-5.5 GeV. The main goal of this analysis was to search for intermediate states decaying to $p\bar{p}$ pairs. A large clean event sample was obtained containing a background of less than 7%. The background was dominated by particle misidentification and incorrect photon energy measurements. At these energies, physics backgrounds, arising from events with other missing particles, do not significantly contribute to the overall background. This conclusion is supported by the continuity of background in the missing mass squared distribution across the mass of the antiproton.

No resonant $p\bar{p}$ structures were observed. No signals for narrow resonant states observed by other experiments were found. The most prominent of these observations was a resonance at 2.02 GeV/c^2 $p\bar{p}$ invariant mass[14][15][16]. The DESY result was based on $\gamma p \to pp\bar{p}$ events for a photon energy range of 4.7-6.6 GeV. DESY claimed a 2.024 ± 0.027 GeV/c^2 resonance with a production cross section of $14 \pm 5nb$. This state was not observed and an upper limit on its production cross section is placed at 0.35 nb. The discrepancy is presumed to be caused by the limited acceptance and the poor statistics of the DESY experiment. The 2.204 ± 16 GeV/c^2 resonance observed by CERN was also not observed. From the calculations for the upper limit on the 2.02 GeV/c^2 resonance, it is estimated that the production cross section of a 2.204 GeV/c^2 resonance is less than 0.5 nb.

From Monte Carlo simulations, it was found that the data is well described by a double-channel production mechanism consisting of both meson exchange and baryon exchange production. It was found that a mixture of 74% meson exchange and 26% baryon exchange describes the data well. Each mechanism was generated using an exponential weighting function for the exchange four-momentum squared, t^{meson} and t^{baryon}. For meson exchange, the exponential slope $b = 3.0(GeV/c)^{-2}$ was observed. For baryon exchange, the slope $a = 0.9(GeV/c)^{-2}$ was observed.

The double-channel Monte Carlo fit produced strong agreement between the experimental data and Monte Carlo simulation. There was good agreement in the momentum exchange, the particle momentum, and the angular distributions. The invariant mass distributions were similar in shape, however a small discrepancy at low $p\bar{p}$ invariant mass exists. Single-channel Monte Carlo events were simulated using various event weighting schemes. The single-channel events did not produce good agreement in the four-momentum exchange, the particle momenta, nor the angular distributions.

Single-channel Monte Carlo simulations had large discrepancies with the data in the angular moments distributions. These discrepancies were caused by the misidentification of protons. In the double-channel Monte Carlo events, proton misidentification was treated at the weighting phase of the simulation, thus providing a tool to handle the misidentification problem. The double-channel events produced moments very similar to those from the data. The strong effects of proton misidentification were not observed in the two-channel Monte Carlo moments. This provides evidence that the two-channel Monte Carlo simulation handles proton misidentification adequately.

The strong agreement in the angular moments between the data and Monte Carlo is evidence that no non-isotropic intermediate states(high-spin resonances) contribute to the data. From this observation and the non-observation of narrow resonant states, it is suggestive that the data is dominated by isotropic non-resonant $p\bar{p}$ production.

It is also suggestive that this non-resonant production occurs predominantly through a meson-exchange process, with a significant contribution from a baryon exchange process.

The differential cross section, $\frac{d\sigma}{dE}$, was calculated for the photon energy range of 4.8-5.5 GeV. The cross section increases from 27.3 ± 0.7 nb to 36.9 ± 0.7 nb over this energy range. These results are in disagreement with those reported by a similar experiment at DESY[16]. The DESY results report a differential cross section that differs roughly by a factor of two.

The existence of the baryonium state claimed by BES[21] is not excluded by this analysis. The CLAS acceptance is much lower for threshold $p\bar{p}$ invariant mass. CLAS is not sensitive to sub-threshold resonant states.

The absence of any evidence for resonant nature in this large data set has inspired theoretical work to predict the cross sections for background processes. These processes can be simply described as reverse proton-antiproton annihilation coupled to the target proton. The model uses proton-antiproton annihilation cross sections to calculate the production cross section for $\gamma p \rightarrow pp\bar{p}$. The reaction $p\bar{p} \rightarrow \gamma\pi^0$ is reversed using the Principle of Detailed Balance[54] ($\gamma\pi^0 \rightarrow p\bar{p}$). This step is necessary in order to use experimental annihilation data. The pion is then coupled to the target nucleon to obtain the production cross section.

Figure 10.1 shows the predicted differential cross section as a function of $p\bar{p}$ invariant mass. The differential cross section is shown for different photon energies. Current estimates of non-resonant pion exchange production are consistent with the experimental production cross section. This theoretical work may provide valuable insight into many background hadronic processes.

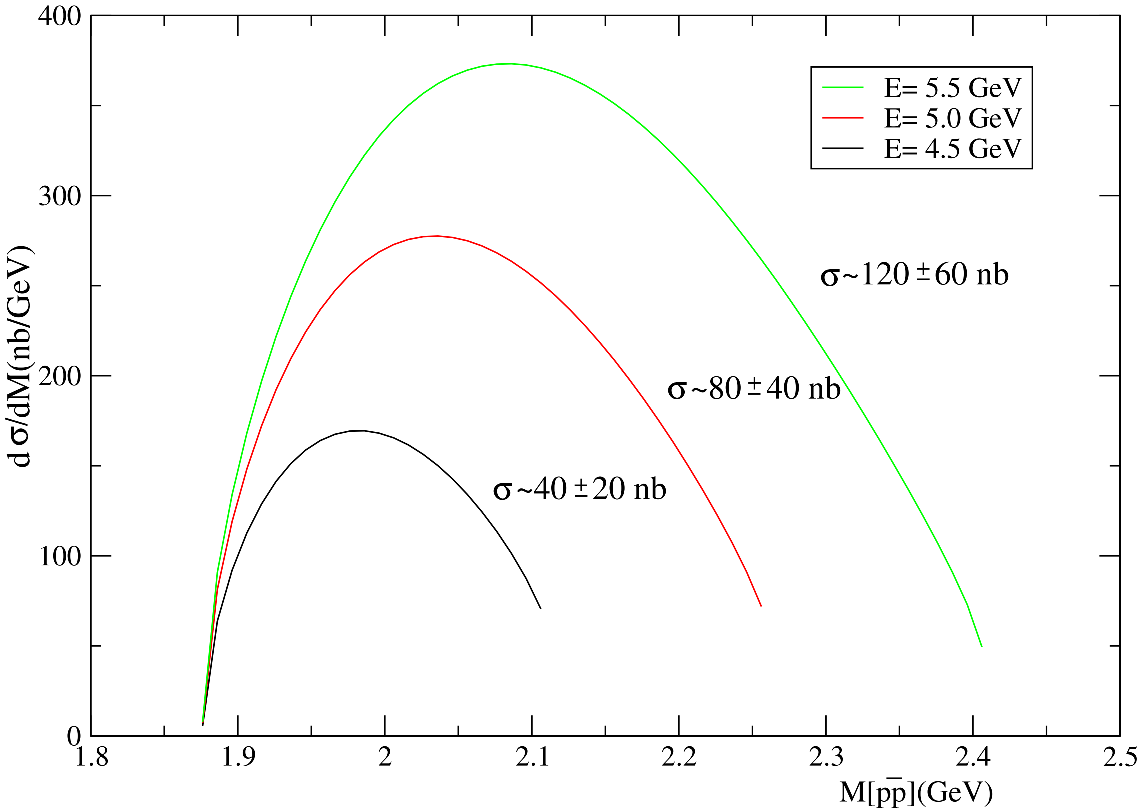

Figure 10.1. The predicted differential cross section as a function of $p\bar{p}$ invariant mass. The differential cross section has been calculated for different photon energies. The current estimates of non-resonant pion exchange production are consistent with the experimental production cross section.

APPENDIX A

DERIVATION OF SYMMETRIZED MOMENTS

In order to account for the two protons in the final state, the transition amplitude must be antisymmetric over the exchange of protons. This section describes the derivation of the symmetrized moments following S.U. Chung's Spin Formalisms [49]. To calculate the transition amplitude of the production of a proton and a state J which then decays to $p\bar{p}$, the final state wave function must be symmetrized under exchange of protons

$$|\psi_f\rangle = \frac{(|p_1 p_2 \overline{p}\rangle - |p_2 p_1 \overline{p}\rangle)}{\sqrt{2}}$$

For an angular momentum projection M, the amplitude M_{f0} of γp →p J→p p $\overline{p}$ becomes

$$M_{f0} = \frac{1}{\sqrt{2}}(M_{f0}^2 - M_{f0}^1) = \frac{1}{\sqrt{2}}(\langle p_1 p_2 \overline{p}|\, M \,|\gamma p\rangle - \langle p_2 p_1 \overline{p}|\, M \,|\gamma p\rangle)$$

Define the helicities of the initial and final state λ_i, where the index of 1(2) is for $p_1(p_2)$. Define the helicity of the intermediate resonance as Λ_i where an index of 1(2) indicates the resonance decays to $\bar{p}p_1(\bar{p}p_2)$. Also define the mass dependent transition operator $T(\omega_0)$, where ω_0 is the center-of-mass energy. The separate transition amplitude terms become

$$M_{f0}^2 \sim \sum_{\Lambda} \langle \overrightarrow{p_2} \lambda_2 \lambda_{\overline{p}}|\, M \,|J\Lambda_2\rangle \left\langle \overrightarrow{p_f^1} \lambda_1 \Lambda_2 \right|\, T(w_0) \,|\overrightarrow{p_0} \lambda_\gamma \lambda_T\rangle$$

$$M_{f0}^1 \sim \sum_{\Lambda} \langle \overrightarrow{p_1} \lambda_1 \lambda_{\overline{p}}|\, M \,|J\Lambda_1\rangle \left\langle \overrightarrow{p_f^2} \lambda_2 \Lambda_1 \right|\, T(w_0) \,|\overrightarrow{p_0} \lambda_\gamma \lambda_T\rangle$$

The helicity decay amplitude is defined as

$$F^J_{\lambda_i\lambda_{\bar{p}}} = 4\pi(\frac{w_i}{p_i})^{\frac{1}{2}} \left\langle J\Lambda_i\lambda_i\lambda_{\bar{p}}\right| M \left|J\Lambda_i\right\rangle$$

The constant N_J is set equal to

$$N_J = (\frac{2J+1}{4\pi})^{(}\frac{1}{2})$$

We then have from Chung [49]

$$\left\langle\overrightarrow{p_i}\lambda_i\lambda_{\overline{p}}\right| M \left|J\Lambda_i\right\rangle = N_{J_i} F^J_{\lambda_i\lambda_{\bar{p}}} D^{J*}_{\Lambda_i\lambda^i}(\Omega_i)$$

where $\lambda^i \equiv \lambda_i - \lambda_{\bar{p}}$ and $\Omega_i = (\theta_i, \phi_i)$

Now define the spin density matrix as

$$\rho^{ij}_{\Lambda\Lambda'} \sim \int d\Omega_i d\Omega_j (-)^{i+j} \sum \left\langle \overrightarrow{p^i_f}\lambda_i\Lambda_{i'}\right| T(w_0)\left|\overrightarrow{p_0}\lambda_\gamma\lambda_T\right\rangle \left\langle \overrightarrow{p^j_f}\lambda_j\Lambda_{j'}\right| T(w_0)\left|\overrightarrow{p_0}\lambda_\gamma\lambda_T\right\rangle^*$$

where the sum is over $\lambda_\gamma$and λ_T, and i' and j' refer to the the opposite index of i or j.

Define $g^{J\lambda_i\lambda_j}_{ij}$ which contains the helicity decay amplitude and the mass dependence

$$g^{J\lambda_i\lambda_j}_{ij} \sim \int dw_1 dw_2 K(w_1, w_2) F^J_{\lambda_i\lambda_{\bar{p}}} F^{J\dagger}_{\lambda_j\lambda_{\bar{p}}}$$

where $K(\omega_1, \omega_2)$ is a factor which includes all the quantities dependent on (ω_1, ω_2), such as the phase space factor. Denote the normalized angular distribution as $I(\Omega_1, \Omega_2)$, then

$$\int d\Omega_1 d\Omega_2 I(\Omega_1, \Omega_2) = 1$$

Then we may write

$I(\Omega_1, \Omega_2) = \sum_{J\Lambda_i\Lambda_j\lambda_{\overline{p}}\lambda_i\lambda_j ij} \frac{2J+1}{4\pi}\rho^{ij}_{\Lambda_i\Lambda_j} D^{J*}_{\Lambda_i\lambda^i}(\phi_i, \theta_i, 0) D^J_{\Lambda_j\lambda^j}(\phi_j, \theta_j, 0) g^{J\lambda_i\lambda_j}_{ij}$

Because Λ_i runs over $2J{+}1$ values for each J the sum becomes somewhat complex,

$I(\Omega_1, \Omega_2) = \sum_{\lambda_{\bar{p}}\lambda_1\lambda_2 J} \frac{2J+1}{4\pi}(a_{11} + a_{12} + a_{21} + a_{22})$

where the a's are :

$a_{11} = \sum_{\Lambda_1\Lambda_1'} \rho^{11}_{\Lambda_1\Lambda_1'} D^{J*}_{\Lambda_1\lambda^1}(\Omega_1) D^J_{\Lambda_1'\lambda^1}(\Omega_1) g^{J\lambda_1\lambda_1}_{11}$

$a_{12} = \sum_{\Lambda_1\Lambda_2'} \rho^{12}_{\Lambda_1\Lambda_2'} D^{J*}_{\Lambda_1\lambda^1}(\Omega_1) D^J_{\Lambda_2'\lambda^2}(\Omega_2) g^{J\lambda_1\lambda_2}_{12}$

$a_{12} = \sum_{\Lambda_2\Lambda_1'} \rho^{21}_{\Lambda_2\Lambda_1'} D^{J*}_{\Lambda_2\lambda^2}(\Omega_2) D^J_{\Lambda_1'\lambda^1}(\Omega_1) g^{J\lambda_2\lambda_1}_{21}$

$a_{22} = \sum_{\Lambda_2\Lambda_2'} \rho^{22}_{\Lambda_2\Lambda_2'} D^{J*}_{\Lambda_2\lambda^2}(\Omega_2) D^J_{\Lambda_2'\lambda^2}(\Omega_2) g^{J\lambda_2\lambda_2}_{22}$

The moments are then

$$H(J, M, M', L, L') = \left\langle D^J_{ML}(\Omega_1) D^J_{M'L'}(\Omega_2) \right\rangle$$

$$= \int I(\Omega_1, \Omega_2) D^J_{ML}(\Omega_1) D^J_{M'L'}(\Omega_2) d\Omega_1 d\Omega_2$$

For simplcity, the number of moments can be reduced by ignoring the terms with differing M M' and L L'. This can be done by setting M'=M and L'=L. This reduces the moments to

$$H(J, M, L) = \left\langle D^J_{ML}(\Omega_1) D^J_{ML}(\Omega_2) \right\rangle$$

The resulting moments are quite simple. They are the average of the Wigner-D function for one $p\bar{p}$ system in its rest frame, mulitplied by that of the other system, and then averaged.

REFERENCES

[1] Particle Data Group, http://particleadventure.org

[2] Particle Data Group, Eur. Phys. J. C, *Review of Particle Physics*

[3] N. Isgur and J. Paton, Phys. Rev. D 31 (1985) 2910.

[4] T. Jordan, http://quarknet.fnal.gov/run2/standard2.html

[5] M.W. Eaton *et al.,* Phys. Rev. D 29 (1984) 805

[6] G. Adams *et al.,* Meson Spectroscopy in Few Body Decays, E99-005

[7] G. Adams *et al.,* Meson Spectroscopy in Few Body Decays, Extension Request

[8] V. Koubarovski, M. Battaglieri, and M. Ripani, CLAS Analysis 2001 Papers 2001-101.

[9] D. Cline *et al.,* Phys. Rev. Lett. 21 (1968) 1268.

[10] V. Chaloupka *et al.,* Phys. Lett.B 61 (1976) 487.

[11] M.N. Focacci *et al.,* Phys. Rev. Lett. 17 (1966) 890.

[12] A.S. Carroll *et al.,* Phys. Rev. Lett. 32 (1974) 247.

[13] T.E. Kalogeropoulos and G.S. Tzanakos, Phys. Rev. Lett. 34 (1975) 1047

[14] P. Benkheiri *et al.,* Phys. Lett. 68 B (1977) 483.

[15] B.G. Gibbard *et al.,* Phys. Rev. Lett. 42 (1979) 1593.

[16] J. Bodenkamp *et al.,* Phys. Lett. 133 B (1983) 275.

[17] R. Bizzarri *et al.,* Phys. Rev. D 6 (1972) 160.

[18] S. U. Chung *et al.,* Phys. Rev. Lett. 45 (1980) 1611.

[19] A. Buzzo *et al.,* Z.Phys.C76 (1997) 475-478.

[20] A. Ferrer *et al.,* The Eur. Phys. J. C 10 (1999) 249.

[21] J. Z. Bai *et al.,* Phys. Rev. Lett.91 (2003) 022001-1.

[22] E. Fermi and C.N. Yang, Phys. Rev. 76 (1949) 1739.

[23] J.M. Richard, Nucl.Phys.Proc.Suppl.86 (2000) 361.

[24] I.S. Shapiro, Phys. Repts. 35 (1978) 129.

[25] D.B. Dover and M. Goldhaber, Phys. Rev. D 15 (1977) 1997.

[26] C.B. Dover, J.M. Richard, Phys. Rev. D. 17 (1978) 1770.

[27] R.L. Jaffe, Phys. Rev. D 17 (1978) 1444.

[28] E.W. Colglazier and J.L. Rosner, Nucl. Phys. B 27 (1971) 349.

[29] B.A. Mecking *et al.,* Nucl. Instr. and Meth. A 503 (2003) 513.

[30] C.K. Sinclair, JLAB-ACT-97-11.

[31] M. Crofford *et al.,* JLAB-ACT-98-06.

[32] M.D. Mestayer *et al.,* Nucl. Instr. and Meth. A 449 (2000) 81.

[33] E.S. Smith *et al.,* Nucl. Instr. and Meth. A 432 (1999) 265.

[34] R. Wigmans, *Calorimetry, Energy Meaurements in Particle Physics.*

[35] S. Christo, *g6c and g8a Target Cell Assembly.*

[36] D.I. Sober *et al.,* Nucl. Instr. and Meth. A 440 (2000) 263.

[37] M. Nozar, CLAS-ANALYSIS 2006-102, *Search for the Photo-Excitation of Exotic Mesons in the* $\pi^+\pi^+\pi^-$ *System.*

[38] P. Barber, Personal Communications.

[39] J. Santoro, *Electroproduction of* $\phi(1020)$ *Mesons at High* Q^2 *with CLAS*, PHD Thesis, Virginia Polytechnic Institute, (2004).

[40] S.J. Taylor, *Radiative Decays of Low-Lying Excited-State Hyperons*, PHD Thesis, Rice University, (2000).

[41] J.W.C. McNabb, *Photoproduction of* Λ *and* Σ^0 *Hyperons off Protons in the Nucleon Resonance Region using CLAS at Jefferson Lab*, PHD Thesis, Carnegie Mellon University, (2002).

[42] R. DeVita, *Measurement of the Double Spin Assymetry in* π^+ *Electroproduction with CLAS*,PHD Thesis, INFN Genova, (2001).

[43] L. Guo, *Search for S=+1 Exotic Baryon in* $\gamma p \to K^+K^-\pi^+(n)$, PHD Thesis, Vanderbilt University, (2004).

[44] E. Pasyuk, http://clasweb.jlab.org/cgi-bin/cvsweb/cvsweb.cgi/packages/eloss/README?rev type=text/x-cvsweb-markup.

[45] J. Li, *Search for Exotic Mesons in* $\pi^+\pi^-\pi^0$ *Decay*, PHD Thesis, Rensselaer Polytechnic Institute, (2003).

[46] E. Wolin, GSIM User's Guide Version 1.1 (1996).

[47] J. Manak, a1c Documentation, http://clasweb.jlab.org/offline/utilities/a1/a1_docs.html, (1997).

[48] G.J. Feldman and R.D. Cousins, Phys. Rev. D 57 (1998) 3873.

[49] S.U. Chung, BNL Preprint, BNL-QGS-02-0900(2005).

[50] M. Williams and C.A. Meyer, CLAS-NOTE 2003-017 (2003).

[51] M.D. Mestayer, *et al.,* Nucl. Instr. and Meth. A 524 (2004) 306.

[52] GEANT, http://geant4.web.cern.ch.

[53] J. Cummings and D. Weygand, *The New BNL Particle Wave Analysis Program* BNL Report 64637 (1997).

[54] F. Coester Phys. Rev. 84 (1951) 1259.

BIOGRAPHICAL SKETCH

Burnham E. Stokes

Florida State University
Department of Physics
Tallahassee, FL 32306-3016
Office: (757) 269-5465
Fax: (757) 269-6248
Email: bestokes@jlab.org
World Wide Web: http://www.jlab.org/∼bestokes/

Current Status	**Research Assistant** Hadronic Nuclear Physics Group Department of Physics Florida State University
Education	**Ph.D. in Nuclear/Particle Physics**, Apr, 2006, Florida State University. **Advisor:** Paul M. Eugenio **Thesis:** Photoproduction of Proton-Antiproton Pairs. **B.S. Physics**, Apr, 2001. Florida State University. **B.S. Mathematics**, Apr, 2001. Florida State University.

Experiences:

Research Assistant	Department of Physics Apr 2002 - present	Florida State University
Teaching Assistant	Department of Physics Aug 2001 - Apr 2002	Florida State University

Research Activities:

My research includes efforts in hadronic nuclear physics towards a better understanding of nonperturbative QCD. I have been performing experiments at JLab such as searching for resonances decaying to proton-antiproton pairs. Recently, I have also been contributing to an effort at Jefferson Lab to build a state-of-the-art hermetic spectrometer– the GlueX project. For this effort, I have the led the construction and design of a prototype electromagnetic calorimeter to be used as an upstream photon veto.

Teaching Experience:

As a Teaching Assistant, I lectured students taking calculus based college physics courses on the subject of laboratory experiments. These lectures covered fundamental concepts as well as laboratory procedures. I also extensively engaged myself with one-on-one discussions with students to answer specific questions and to reinforce their understanding of physics.

Conference Presentations:

B. Stokes , "Photoproduction of Proton-Antiproton Pairs," *APS Division of Nuclear Physics Conference*, October 2003

B. Stokes , "$\pi^- p \rightarrow K^+ K^- \pi^+ \pi^- n$" *APS Division of Nuclear Physics Conference*, October 2002

Conference Proceedings:

P. Eugenio and B. Stokes , "Photoproduction of Proton-Antiproton Resonances," *AIP Conference Proceedings*, Journal 717 1 Conference 10, 2004

Representative Publications

1. *Beam-Helicity Asymmetries in Double-Charged-Pion Photoproduction on the Proton.*, CLAS Collaboration, (S. Strauch et al.), Submitted to Phys. Rev. Lett. (2005).

2. *Measurement of the Deuteron Structure Function F(2) in the Resonance Region and Evaluation of its Moments.*, CLAS Collaboration, (M. Osipenko et al.), Submitted to Phys. Rev. D (2005).

3. *Electron Scattering from High-Momentum Neutrons in Deuterium.*, CLAS Collaboration, (A.V. Klimendo et al.), Submitted to Phys. Rev. C (2005)

4. *Search for* Θ^+*(1540) Pentaquark in High Statistics Measurement of* $\gamma p \rightarrow \bar{K}0K^+N$ *at CLAS.*, CLAS Collaboration, (M. Battaglieri et al.), Phys. Rev. Lett. 96 042001 (2005).

5. *Deeply Virtual and Exclusive Electroproduction of Omega Mesons.*, CLAS Collaboration, (L. Morand et al.), Eur. Phys. J. A24:445-458 (2005).

6. *Measurement of the Polarized Structure Function* $\sigma_{LT'}$ *for Pion Electroproduction in the Roper Resonance Region.*, CLAS Collaboration, (K. Joo et al.), Phys. Rev. C. 72 058202 (2005).

7. *Radiative Decays of the* Σ^0*(1385) and* Λ*(1520) Hyperons.*, CLAS Collaboration, (S. Taylor et al.), Phys. Rev. C 71 054609 (2005).

8. *Exclusive* ρ^0 *Meson Electroproduction from Hydrogen at CLAS.*, CLAS Collaboration, (C. Hadjidakis et al.), Phys. Lett. B 605 256-264 (2005).

9. *Measurement of the Polarized Structure Function* $\sigma_{LT'}$ *for P(Polarized-e,e'* π^+*)N in the* Δ*(1232) Resonance Region.*, CLAS Collaboration, (K. Joo et al.), Phys. Rev. C 70 042201 (2004).

10. *Survey of* $A_{LT'}$ *Asymmetries in Semi-Exclusive Electron Scattering on He-4 and C-12.*, CLAS Collaboration, (D. Protopopescu et al.), Nucl. Phys. A 748 357-373 (2004).

11. *Proton Source Size Measurements in the eA* $\rightarrow$ *e' PPX Reaction.*, CLAS Collaboration, (A.V. Stavinsky et al.), Phys. Rev. Lett. 93 192301 (2004).